

**A Computational Platform to Unravel the Mechanisms of Directed
Self-Assembly of Nanoparticles on Surfaces**

by

ZHEN LUO

B.S., Beijing University of Chemical Technology, 2010

M.S., Beijing University of Chemical Technology, 2013

THESIS

Submitted in partial fulfillment of the requirements
for the degree of Doctor of Philosophy in Chemical Engineering
in the Graduate College of the
University of Illinois at Chicago, 2021

Chicago, Illinois

Defense Committee:

Shafiqh Mehraeen, Chair and Advisor

Gang Cheng

Vivek Sharma

Sangil Kim

Robert Klie, Physics

Copyright by

ZHEN LUO

2021

This thesis is dedicated to my parents, without whom it would never have been accomplished.

ACKNOWLEDGMENT

Throughout the writing of this dissertation I have received a great deal of support and assistance.

I would first like to thank my research advisor, Professor Mehraeen, whose expertise was invaluable in formulating the research project and methodology. Your continuous guidance and insightful feedback pushed me to sharpen my thinking and brought my work to a higher level.

I would also thank my committee members, Professor Klie, Professor Cheng, Professor Sharma and Professor Kim, for their valuable recommendations during my preliminary exam as well as defense. You provided me with the advices and assistance that I needed to successfully complete my dissertation as well as scholarship application.

In addition, I would like to thank my family for their solid support, wise counsel and sympathetic ear.

TABLE OF CONTENTS

<u>CHAPTER</u>		<u>PAGE</u>
1	INTRODUCTION	1
1.1	Directed Self-Assembly	1
1.2	Applications	5
1.2.1	Plasmonic Devices	6
1.2.2	Semiconducting Nanowire Devices	6
1.2.3	Photovoltaic Devices	7
1.3	State of Art	8
1.3.1	Dynamics of Directed Self-Assembly of nanoparticle (DSA-n) on Templated Surface	8
1.3.2	Design of Templated Surface	11
1.3.3	Design of Accumulation Zone	12
1.3.4	Computational Modeling	14
1.4	Thesis Outline	16
2	A PREDICTIVE MODEL TO PROBE THE IMPACT OF GRAV- ITY AND SURFACE TENSION ON RISING WETTING THIN FILMS	17
2.1	Introduction	17
2.2	Theoretical Model	19
2.3	Results and Discussion	25
2.3.1	Progression of rising liquid film	25
2.3.2	Impact of gravity	27
2.3.3	Impact of surface tension	32
2.3.4	Structure factor	36
2.4	Conclusions	39
3	UNRAVELING THE MECHANISM OF A RISING THREE- PHASE CONTACT LINE ALONG A VERTICAL SURFACE USING MANY-BODY DISSIPATIVE PARTICLE DYNAMICS	41
3.1	Introduction	41
3.2	Theoretical Model	44
3.2.1	Many-body Dissipative Particle Dynamics (MDPD) model . .	44
3.2.2	Parametrization	45
3.2.3	Static contact angle measurement	47
3.3	Results and Discussion	53
3.3.1	Spontaneous capillary rise of liquid film	53
3.3.1.1	Double-wall configuration	53

TABLE OF CONTENTS (Continued)

<u>CHAPTER</u>		<u>PAGE</u>
3.3.1.2	Single-wall configuration	56
3.3.2	Dynamic contact angle	63
3.3.3	Velocity and vorticity profile	64
3.4	Conclusions	66
4	A MOLECULAR VIEW OF THE DISTORTION AND PINNING FORCE OF A RECEDING CONTACT LINE: IMPACT OF THE NANOCAVITY GEOMETRY	68
4.1	Introduction	68
4.2	Theoretical Model	71
4.2.1	MDPD model	71
4.2.2	Simulation setup	71
4.2.3	Machine learning classification	73
4.3	Results and Discussion	73
4.3.1	Progression of receding liquid film	73
4.3.2	Distortion	75
4.3.3	Pinning force	80
4.3.4	Pathline	82
4.3.5	Dynamic contact angle	83
4.4	Conclusions	93
5	IMPACT OF TEMPLATE GEOMETRY AND CONFINEMENT ON DIRECTED SELF-ASSEMBLY OF NANOPARTICLES	95
5.1	Introduction	95
5.2	Theoretical Model	98
5.2.1	MDPD model	98
5.2.2	Simulation setup	98
5.3	Results and Discussion	100
5.3.1	Progression of DSA-n on template substrate	100
5.3.2	Confinement impact on the yield of DSA-n	104
5.3.2.1	DSA-n phase diagram	104
5.3.2.2	Thickness variation	106
5.3.2.3	Nanoparticle concentration variation	107
5.3.2.4	Dynamics of the nanoparticles in the confinement	112
5.3.2.5	Impact of the local confinement on the yield of DSA-n	116
5.3.3	Impact of the template geometry on the yield of DSA-n	120
5.3.3.1	Impact of the nanocavity interspacing on the yield of DSA-n	121
5.3.3.2	Impact of the circular nanocavity radius on the yield of DSA-n	124
5.4	Conclusions	127

TABLE OF CONTENTS (Continued)

<u>CHAPTER</u>		<u>PAGE</u>
6	FREE ENERGY CONTRIBUTIONS TO TEMPLATE-ASSISTED SELF-ASSEMBLY OF NANOPARTICLES FROM STEERED MOLECULAR DYNAMICS SIMULATIONS	129
6.1	Introduction	129
6.2	Theoretical Model	133
6.2.1	MDPD model	133
6.2.2	Simulation setup	133
6.3	Results and Discussion	134
6.3.1	Stagnant liquid film	135
6.3.2	Receding liquid film	147
6.4	Conclusions	154
7	FUTURE DIRECTIONS	156
	REFERENCES	162
	VITA	183

LIST OF TABLES

<u>TABLE</u>		<u>PAGE</u>
I	THE MAPPING BETWEEN DIMENSIONLESS AND DIMENSIONAL GRAVITATIONAL ACCELERATION	32
II	THE MAPPING BETWEEN DIMENSIONLESS AND DIMENSIONAL SURFACE TENSION	35
III	MAPPING BETWEEN DIMENSIONLESS AND DIMENSIONAL MDPD PARAMETERS	47
IV	MAPPING BETWEEN DIMENSIONLESS AND DIMENSIONAL MDPD PARAMETERS	72
V	MAPPING BETWEEN DIMENSIONLESS AND DIMENSIONAL SIMULATION PARAMETERS	100
VI	MAPPING BETWEEN DIMENSIONLESS AND DIMENSIONAL SIMULATION PARAMETERS	134

LIST OF FIGURES

<u>FIGURE</u>		<u>PAGE</u>
1	Schematic illustration of paths of Directed Self-Assembly (DSA) of nano-materials to achieve functional systems. (a) Low dimensional nanomaterials used to assemble nanostructures. (b) Approaches of Self-Assembly (SA). (c) Approaches of DSA. (d) Prominent fields using SA and DSA techniques. (17)	3
2	Example of two-dimensional patterns of Au nanorods fabricated on lithographically-defined surface using DSA. All scale bars, 250nm. (31)	5
3	Schematic of DSA-n on a templated surface, displaying the sequential stages of nanoparticle assembly from initial suspension in liquid film to final deposition on the templated surface. (50)	9
4	(A) The 3D schematics of the Ising lattice gas model, illustrating the rise of the liquid layer on the vertical substrate. Red particles represent the bulk liquid, gray and blue particles show the first and second layer of particles located at $z = 1$ and 2 , respectively, and green particles illustrate the solid-liquid interface. Numbered arrows show four in-plane and one out-of-plane nearest neighbors. (B) Cross section of the schematics, depicting the four component of the total energy, gravity, van der waals interaction with the substrate, nearest neighbor particle-particle interaction (bottom inset), and interfacial energy (top inset).	22
5	Top view of 10 snapshots, illustrating the rise of the liquid layer at different times, $t = 1 \times 10^7, \dots, 10 \times 10^7$ with the interval of 10^7 in KMC time unit. Occupied sites at $z = 1$ and 2 are shown in gray and blue, corresponding to bottom and top layer, respectively. Empty sites are shown in white. Parameters used are $A = 30$, $J = 3$, $g' = 0$, $\sigma = 0$. . .	26
6	Log-log plot of evolution of the (A) average interface displacement, (B) instantaneous interface velocity, and (C) interface roughness of the rising liquid layer with time, t , in Kinetic Monte Carlo (KMC) time unit. Solid lines are averages over 200 independent KMC simulations with $A = 30$, $J = 3$, $\sigma = 0$, and $g' = 0, 0.01, 0.05$ and 0.25 , from red to blue, respectively. Dashed lines are the guide for the eye.	28

LIST OF FIGURES (Continued)

<u>FIGURE</u>		<u>PAGE</u>
7	Log-log plot of growth of the (A) average interface displacement, (B) instantaneous interface velocity, and (C) interface roughness of the rising liquid layer with time, t , in KMC time unit. Solid lines are averages over 200 independent simulations with $A = 30$, $J = 3$, $g' = 0$, $\sigma = 0, 0.8, 1.6, 2.4$, and 3.2 , from red to blue, respectively. Dashed lines are the guide for the eye.	34
8	Structure factor of the interface roughness at 5 logarithmically spaced KMC time unit between $t = 10^3$, and 10^6 , from red to blue, respectively, averaged over 200 independent KMC simulations for (A) $g' = \sigma = 0$, (B) $g' = 0, \sigma = 3.2$, (C) $g' = 0.05, \sigma = 0$ and (D) $g' = 0.25, \sigma = 0$. Other parameters are $A = 30, J = 3, L_x = 512$, and $L_y = 300$. Dashed lines are the guide for the eye, illustrating k^{-2} , $k^{-1.7}$, $k^{-1.6}$ and $k^{-1.2}$ behavior in panels A, B, C and D respectively.	38
9	Two dimensional schematic of interface (red line) capturing technique, distinguishing solid (black particles) and liquid (cyan particles) from vapor (blank area) phase.	48
10	The equilibrium particles configuration for MDPD attraction parameter in increasing order, $A_{sl} = -40$ to -10 with the interval of 10, from left to right, respectively.	50
11	Configuration setup to compute γ_{sl} for various A_{sl} . Gray particles represent the solid phase, and cyan particles illustrate the liquid phase. . .	50
12	Comparison of cosine of the static contact angle, θ_s , as a function of A_{sl} , from MDPD model (red), Young's equation (blue) both averaged over 10 simulations, and the work by Henrich <i>et al.</i> (127) Error bars indicate the corresponding standard deviation.	52
13	Front view at x - y plane taken from MDPD simulations illustrating the progression (from left to right) of spontaneous capillary rise of a thin liquid film in double-wall geometry.	54
14	Evolution of height of liquid film in MDPD time unit (red), averaged over 10 simulations and measured at the center-line ($x = L_x/2$) during spontaneous capillary rise through the gap between two standing solid walls shown in Figure 13. Dashed lines are the guide for the eye.	55

LIST OF FIGURES (Continued)

<u>FIGURE</u>		<u>PAGE</u>
15	Side view of MDPD simulations, from left to right, illustrating the progression of spontaneous capillary rise of a liquid film along a standing single wall partially immersed into a liquid reservoir at the bottom. . .	58
16	Rough (A), flat (B), and patterned-with-square-cavity (C) wall-surface structure (in y-z plane) along which displacement of the contact line is measured in time. Wall color varies with depth from green to blue corresponding to top to bottom surface. See text for characteristics of rough and patterned surfaces.	59
17	Log-log plot of evolution of the maximum interface displacement (averaged over 5 simulations) as a function of MDPD time during the rise of a liquid film along a rough (blue), flat (red), and patterned-with-square-cavities (black) single-wall surface, shown in Figure 16. Dashed lines are the guide for the eye. Shaded area locates the period during which dynamic contact angle decreases (see Figure 27 for details).	60
18	Particle density profile in the solid (red) and liquid (blue) phase at three cross sections aa , bb and cc , shown in the right panel in Figure 15. Shaded area in cross section aa and bb highlights the solid wall location.	62
19	(A) Extracting dynamic contact angle between the fitted tangent to the interface and a vertical line (angle between two red lines) using interface tracking technique. (B) The variation of dynamic contact angle (blue) and moving average of dynamic contact angle (red) vs. MDPD time. Shaded area locates the range where the dynamic contact angle decreases.	64
20	Velocity (black arrows) and vorticity (colormap) field in (A) x-y plane at $z = L_z/2 = 2.5$, (B) z-y plane at $x = 3$, and (C) x-z plane at $y = 40$, during capillary rise of the liquid thin film along a single wall positioned between $0 \leq x \leq 1$ (not pictured), averaged over 8 simulations. Red line indicates solid-liquid and liquid-vapor interface. Absence of an interface indicates positions where the periodic boundary condition is applied. .	66
21	(A-E) Progression of dewetting of a liquid film (cyan) sliding over a solid substrate (gray) with a circular nanocavity. Dewetting is driven by a hydrophilic piston (red) moving down while in contact with the liquid film.	75
22	(A) Top view of the superposition of progression of contact line pinning as it is receding over a circular nanocavity, from top to bottom, light to dark blue, respectively. (B) The schematic of distortion definition. . . .	76

LIST OF FIGURES (Continued)

<u>FIGURE</u>		<u>PAGE</u>
23	(A-D) Progression of contact line pinning for circular (top) and horizontally oriented elliptical (bottom) nanocavities. (E) The variation of contact line distortion with time (in MDPD units) for circular (C, red) and horizontally oriented elliptical (HOE, blue) nanocavities. Lines are the best fit to the instantaneous distortion (dots). (F) Variation of contact line distortion with time for square (S), vertically oriented elliptical (VOE), upward triangular (UT), and downward triangular (DT) nanocavities. Contact line distortion with time for circular nanocavity was also included for reference.	77
24	(A) The variation of pinning force against distortion for upward triangular (UT), horizontally oriented elliptical (HOE), square (S), circular (C), downward triangular (DT), and vertically oriented elliptical (VOE) nanocavities, color coded from red to blue, respectively. Symbols are the distinct force-distortion measurements taken from MDPD simulations and solid lines are the fits. (B) Comparison of spring constants taken from the linear fits in Figure 24A (solid lines) with that from experiment (dashed line), using spherical defects.	82
25	(A) Top view in yz -plane showing pathlines of 7 equally spaced tracer particles sampled along the contact line slightly above the nanocavity. The pathlines are color coded from red to blue, respective to the progression of trajectories. The dashed line represents the circular nanocavity. (B) Side view in xy -plane displaying the pathlines following a large circular (caterpillar) motion.	84
26	(A) Top view in yz -plane showing pathlines of 7 equally spaced particles sampled along the contact line, when it is right above the nanocavity. The pathlines are color coded from red to blue, corresponding to the progression of trajectories. The dashed line represents the circular nanocavity. (B) Side view in xy -plane displaying the pathlines following a large rotational flow field.	85
27	(A) A receding contact line is pinned once the liquid (cyan) is pulled down by the piston (red) to go over a circular nanocavity (blue) on an otherwise flat substrate (gray). Dynamic contact angle is monitored along a - a (red line), b - b (magenta line) and c - c (blue line) cross sections. (B) The variation of dynamic contact angle against the MDPD time along a - a , b - b and c - c cross sections, with $A_{sl} = -30, -35$ and -38 , from top to bottom, respectively, averaged over 10 simulations.	88

LIST OF FIGURES (Continued)

<u>FIGURE</u>		<u>PAGE</u>
28	A pinned contact line is depicted while the liquid (cyanMDPDparticles) is going over a nanocavity with upward triangle, horizontally oriented ellipse, square, downward triangle, and vertically oriented ellipse cross section, A to E, respectively, as the piston (red plate) is pulled down.	89
29	Variation of the dynamic (receding) contact angle along a-a (A), b-b (B), and c-c (C) cross section, as shown in Fig. Figure 27A. The dynamic contact angle variations are color-coded from red to blue, respective to Upward Triangular (UT), Horizontally Oriented Elliptical (HOE), Square (S), Circular (C), Downward Triangular (DT), and Vertically Oriented Elliptical (VOE) nanocavity.	91
30	Maximum variation of the dynamic contact angle along cross section c-c for the 6 geometries in Figure 29C averaged over 10 simulations (dots) and the respective standard deviation shown by the error bars.	93
31	Progression of a liquid thin film sliding over a substrate with templated array of circular nanocavities from top to bottom (A-D) is shown while the purple piston is pulled down to conduct DSA-n. Top view of panel D indicates deposition of nanoparticles (red particles), where liquid particles (cyan) are turned off for clarity (E).	101
32	Progression of an advancing liquid film (cyan) with suspension of nanoparticles, moving over a templated substrate (gray) with an array of circular nanocavities (white holes) from bottom to top (A-D). Top view of the same snapshot in D while liquid particles are turned off for clarity. Red particles represent directly self-assembled nanoparticles, whereas yellow ones illustrate those in the bulk liquid.	103
33	The phase diagram of yield of DSA-n as a function of nanoparticle density, ρ , and the liquid film thickness, d . Nanoparticle configuration for points A-D on the phase diagram are visualized in Figure 36.	105
34	The yield of DSA-n (p) into a 10×10 array of circular nanocavities against the liquid film thickness (d) at fixed nanoparticle density, $\rho = 0.05, 0.07$, and 0.09 , corresponding to red, blue, and black, respectively.	106
35	The yield of DSA-n vs. concentration of nanoparticles at fixed liquid film thickness of $d = 3, 5$ and 7 , respective to red, blue, and black. . . .	107

LIST OF FIGURES (Continued)

<u>FIGURE</u>		<u>PAGE</u>
36	<p>The top view of last snapshot of MDPD simulations corresponding to four different points on the phase diagram in Figure 33 (A-D). Middle row panels illustrate the corresponding orientational order parameters per particle color coded from blue to red, respective of 0 to 1 high. The average particle's 2D bond orientational order parameter is shown at the top of each panel. Bottom row panels depict the 3D view of the same snapshots in the top row, while liquid particles (cyan) are turned on. All particle configurations are obtained at the same MDPD time step in MDPD simulations.</p>	111
37	<p>Top view of trajectories of 3 tracer nanoparticless from their initial (blue) to final (green) position over a templated substrate with 10×10 array of circular nanocavities (A). x-trajectory vs. MDPD time for the tracer nanoparticle marked by a white arrow in A, where purple and cyan dashed lines indicate the MDPD time at which the piston and receding contact line goes over the marked nanoparticle deposited in the nanocavity (B). y-trajectories of all 100 nanoparticles involved in the DSA-n, where blue line is trajectory of the receding contact line, green line is trajectory of the marked tracer nanoparticle, and red line is the trajectory of a nanoparticle that is directly self-assembled by the receding interface (C). z-trajectory of the marked tracer nanoparticle where the dashed red line represents the surface of the templated substrate (D). Likelihood of the marked tracer nanoparticle being in and out of the nanocavity.</p>	115
38	<p>Comparison of the top and side views with the liquid film turned on (blue cyan particles) and off for clarity, and nanoparticle configurations between receding liquid film by moving a piston (A) and a flat plate (B). Panels in the bottom row compares the distribution (blue histogram), mean (red dashed line), and median (blue dashed line) of nearest neighbor distances for the two aforementioned MDPD simulations.</p>	118
39	<p>The comparison of velocity and vorticity profile in DSA-n the liquid film pulled by the piston (AB), and a flat plate (CD). Panels A and C represent instantaneous profiles, while panels B and D represent profiles averaged over 5 independent simulations. Red contour line indicates solid-liquid and liquid-vapor interface, arrows show velocity field, and vorticity field is color coded from blue to red, low to high, respectively.</p>	120

LIST OF FIGURES (Continued)

<u>FIGURE</u>		<u>PAGE</u>
40	An intermediate (left three panels) and final (right panels) snapshots of MDPD simulations of DSA-n on templated substrate with increasing center-to-center distance between nanocavities from 3.5 (A), to 4.25 (B), and 5 (C). Far left and right panels are the top views with liquid (cyan particles) turned on and off for clarity, respectively. The middle panels are the side views, corresponding to the left panels, with and without the liquid film visualized. All snapshots are taken at the same time point.	123
41	The three left panels show an intermediate snapshot taken from the MDPD simulations, and the right panel was taken when the contact line went past the array. Nanocavity radius increases from 1.5 (A) to 1.75 (B) to 2 (C), the left and right panels show the top views, and the middle two panels illustrate the side views of the far left panel. In the left two panels, liquid film is turned on whereas in the right two panels it is turned off for clarity. All intermediate snapshots were taken at the same time point during the simulations.	126
42	(A) The top view of the liquid film (not shown for clarity) over a templated surface (gray) with a nanocavity (white circle), gold nanoparticles (yellow), and the tracer nanoparticle (red), used as the initial condition for the SMD simulation. (B-C) The side views, illustrating the progression of the SMD simulation, where the tracer is guided from the bulk liquid to the bottom of the nanocavity, respectively, by contraction of the black spring while the liquid film is stagnant.	137
43	The side view of 100 independent trajectories of the tracer nanoparticle in the yz -plane during the SMD simulations. The dashed line indicates the substrate and nanocavity surface. The nanoparticle density decreases from 0.1 to 0, from A to F, respectively.	139
44	(A) Top view of the starting point of SMD simulations, where initial positions of the tracer nanoparticle are located in the black square in xy -plane, color coded from red to blue, corresponding to densities $\rho = 0.1$ to 0 with the interval of 0.02, respectively. The pink circle represents the top view of the circular nanocavity. (B) The external work done on the tracer to move it from $z = 5.5$ to $z = 3.0$ averaged over 100 independent trajectories with initial positions in A for the 6 different densities. Legend indicates the nanoparticle densities. (C) The change in free energy calculated from Jarzynski's equality in Equation Equation 6.5 color coded for the 6 different densities. The work and change in the free energy are nondimensionalized by kT	144

LIST OF FIGURES (Continued)

<u>FIGURE</u>		<u>PAGE</u>
45	The average work, W , free energy change, ΔE , fluctuations in the work, $\text{std}(W)$, and energy dissipation profile, W_{diss} for the tracer nanoparticle in the absence of other nanoparticles in SMD simulation with a flat surface (A), in the presence of a nanocavity (B), and in the presence of a nanocavity and other nanoparticles with $\rho = 0.08$ (C). The results were obtained over 100 independent simulations.	146
46	Panel A presents a top view of liquid film over a templated surface with a nanocavity as the initial condition of the SMD simulations. Side view of a SMD simulation at 3 stages (B to D) shows the progression of a tracer nanoparticle deposition guided by a SMD spring (black) while the liquid film is receding downward.	147
47	The trajectories of a tracer nanoparticle in the yz -plane, obtained from 100 independent SMD simulations. Nanoparticle density, ρ varies from 0.1 (A) to 0 (F).	149
48	The initial positions of a tracer nanoparticle in xy -plane (A), average work (B), and the free energy change (C), averaged over 100 independent SMD simulations for each density. Red to blue corresponds to the density of nanoparticles ranging from 0.1 to 0.	150
49	Comparison of the free energy change in SMD simulations for $\rho = 0.1$ and different attraction strength between the tracer and other nanoparticles.	152
50	The work and its fluctuation, W and $\text{std}(W)$, respectively, free energy change, ΔE , and energy dissipation profile, W_{diss} for the tracer nanoparticle during deposition on a flat substrate in the absence of bulk nanoparticles (A), deposition on a templated substrate with nanocavity at $\rho = 0$ (B), and $\rho = 0.08$ (C). The results are averaged over 100 independent SMD simulations, where the liquid film is receding from top to the bottom.	153

LIST OF ABBREVIATIONS

BD	Brownian Dynamics
DPD	Dissipative Particle Dynamics
DSA	Directed Self-Assembly
DSA-n	Directed Self-Assembly of nanoparticle
HSQ	Hydrogen Silsesquioxane
KMC	Kinetic Monte Carlo
MC	Monte Carlo
MD	Molecular Dynamics
MDPD	Many-body Dissipative Particle Dynamics
NW	Semiconducting Nanowire
SA	Self-Assembly
SVM	Support Vector Machine

SUMMARY

The development of miniaturization in semiconductor manufacturing is mainly driven by the continuous pursuit of extremely powerful performance and efficient energy consumption behind which requires more sophisticated design of devices in nanoscale, even beyond sub-10 nm dimension. Integration of nanomaterials with such patterned devices would further promote cooperative phenomenon with adjacent substrate materials, and demonstrate extraordinary physicochemical properties. However, the fabrication process of above-mentioned low-dimensional devices demands strict control on nanostructure positioning that incurs several difficulties. None of the conventional patterning techniques with top-down photolithography is able to adequately address the challenge due to physical restriction in resolution. Alternative techniques have been introduced to solve the problem, including ultra-violet lithography, nanoimprint lithography, and directed self-assembly, among which directed self-assembly presents a potential in producing structurally and functionally complex substrate-supported nanostructure in a well-tunable and cost-effective manner, in addition to its broad applicability and operational simplicity.

Recent development in directed self-assembly on templated surfaces, while remains at a beginning stage, has presented the opportunity of assembling arrays of nanoparticles. Advanced control over the assembly process including the dynamics of advancing/receding contact line, optimization of confinement and template, nevertheless, requires accurate and complete understanding of the underlying mechanisms. In addition, the experimental study on the contact line

SUMMARY (Continued)

behavior or further in directed self-assembly needs to create a thin film of hundred nanometers thickness which remains a challenge in terms of efficiency and cost. Nevertheless, computational modeling provides with great feasibility and convenience to investigate a variety of parameters at specific conditions.

We develop a 3D kinetic Monte Carlo model to understand the dynamics of the liquid film developed during dip coating process and the wetting behavior of a liquid film rising along a vertical substrate. By varying gravitational acceleration and surface tension, we present explicit analysis of the effect of dynamics of solid-liquid interface on the interfacial displacement and contact line roughness.

To further unravel the wetting mechanism of spontaneous rise of thin liquid film, we present a coarse grained Molecular Dynamics simulation. We investigate the dynamics of a rising contact line by demonstrating its displacement and dynamic contact angle in single- and double-wall geometry, and different surface roughness.

Lithographically-defined substrates also play a significant role in pinning, deformation, and contact line of a liquid film receding over the substrate. Using a coarse grained Molecular Dynamics simulation, we show the pinning force and distortion of the pinned contact line varies across different nanocavity shapes and orientation. A rotational flow at the receding contact line is observed, and a localized clamping effect originated from the variation of dynamic contact angle is determined, and discussed.

To explore the impact of confinement, nanoparticle density, and template geometry on the directed self-assembly of nanoparticles, we utilize a series of coarse grained Molecular Dynamics

SUMMARY (Continued)

simulations. We develop a phase diagram for the directed self-assembly of nanoparticles. From the phase diagram, we show that high yield of nanoparticle deposition is obtained at specific combination of liquid film thickness (confinement) and nanoparticle density. We propose a new mechanism for the directed self-assembly by providing a series of analyses of nanoparticles trajectories. The new mechanism has roots in random hopping between the bulk liquid and nanocavity, which is shown to occur far from liquid-vapor meniscus. We also discuss the impact of template geometry on the yield by modifying the center-to-center distance and circular nanocavity radius.

We then turn to the energetics of the directed self-assembly, and determine the free energy and entropic contributions to the self-assembly of nanoparticles, using Jarzynski's equality. Taking advantage of the Steered Molecular Dynamics simulations with both stagnant and receding liquid films, we discuss the impact of nanoparticle densities and receding contact line on the free energy contributions. We show that the directed self-assembly of nanoparticles is entropically prohibitive at low nanoparticle densities, and energetically unfavorable at high nanoparticle densities.

Last but not least, we propose future directions, which can facilitate the template design, controlling non-equilibrium process of directed self-assembly of nanoparticles, and optimizing the yield during experiments, using machine learning with a continuous feedback loop linked to the experiments.

CHAPTER 1

INTRODUCTION

1.1 Directed Self-Assembly

The coffee ring phenomenon has been a main driver for researchers to creatively develop the Self-Assembly (SA) technique as an efficient and cost-effective approach for achieving complex nanostructures with controlled arrangement and scalability. (1; 2; 3) As a drop of coffee dries out on solid surface, it leaves a dense ring-shape stain, which implies a net flow towards the edge, and a complete transfer of coffee particles to the perimeter. (4) Similar flow of solute has been observed in solvent evaporation of polymer films, where the region near the free surface is polymer rich. (5) The accumulation of ring deposit has been demonstrated to be the result of capillary-assisted accumulation, in which the continuous evaporation at pinned contact line of coffee drop leads to an outward flow of interior liquid carrying coffee particles. (3) In the evaporation process, the shrinking contact line slides over accumulated particles which are fixed by lateral capillary force of leftover liquid at the edge. (2) It has also been proposed that the decrease of density in stain deposit follows a parameter that depends on the distance from the edge as well as the local evaporation rate. (6) This capillary flow mechanism facilitates spontaneous deposition of coffee particle and furthermore provides insights into developing SA approaches.

Over the past two decades, there has been a lot of applications using SA process in material manufacturing, including printing, coating, photonics and biosensing devices. (7; 8; 9; 10) Classic SA refers to the phenomenon in which individual components (such as nanoparticles, nanotubes, nanorods and polymer chains) spontaneously organize themselves into a variety of structures, including chains, sheets, 3D crystals and even more complex structures, as shown in Figure 1a. (11; 12; 13; 14; 15; 16; 17)

Solution-based assembly is a major strategy of SA, in which the process is governed by the balance of interactions between individual components, also referred as molecular recognition and association. The attractive forces of interaction includes hydrogen bonding, electrostatic attraction of unlike charges, and inter-dipole interactions, while the repulsive forces of interaction includes steric forces and electrostatic attraction of like charges. (18)

As a bottom-up nano-fabrication process, one of the fundamental aspects of research is to solve the challenge of defects in scale-up assembly, which are difficult to remove without any external direction input. Additionally, high complexity of 3D nanostructure requires a better morphological control in the aggregation of building blocks, that again demands a higher level of modulation involved. (3; 19) To address such difficulties, Directed Self-Assembly (DSA) is introduced to provide additional guide in the intrinsically SA process with controlled alignment, spacing and location.

On top of SA, DSA is accomplished by exploiting external field or pre-defined template to assist the SA process by directing specific assembling blocks into desired structure and arrangement. Numerous DSA approaches have been developed to assemble anisotropic nanostructures

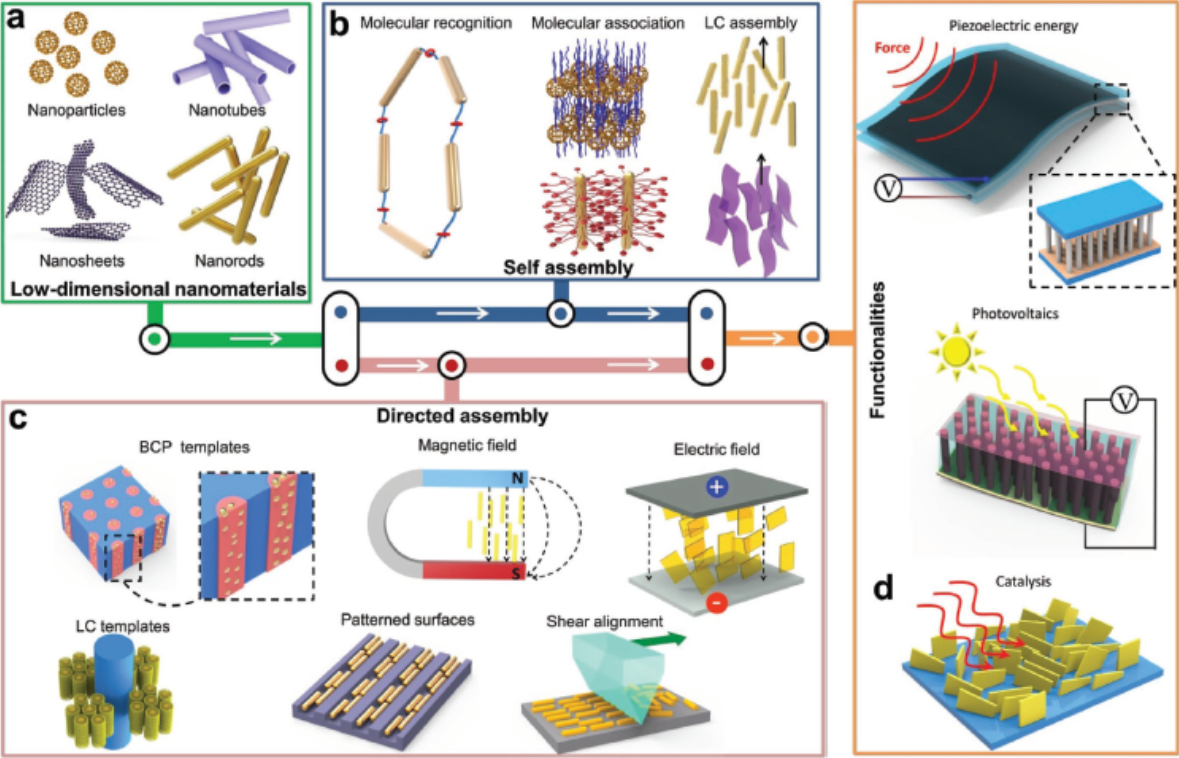


Figure 1: Schematic illustration of paths of DSA of nanomaterials to achieve functional systems. (a) Low dimensional nanomaterials used to assemble nanostructures. (b) Approaches of SA. (c) Approaches of DSA. (d) Prominent fields using SA and DSA techniques. (17)

from random distribution of individual components, with the application of magnetic field, electric field, flow field, phase interface and templates, as shown in Figure 1c. (20; 21; 22; 23; 24; 17)

The use of external fields (magnetic, electric and flow fields) offers great potential to induce orientation-dependent interactions with tunable intensity and direction that helps to create configurations with alignment. Apart from static magnetic field DSA, electric field DSA is able to generate heating and other electro-hydrodynamic effects that increase the complexity

of DSA, while flow field DSA can generate a number of modes, including simple shear flow, evaporation, Marangoni flow and capillary force. (25; 26; 27; 28)

In addition to external forces, the use of template in DSA utilizes pre-defined substrates in SA process that helps organize individual components into a diverse range of structures or arrangement. With the development in synthesis of nanoparticles with well-defined sizes, shapes and compositions, Directed Self-Assembly of nanoparticle (DSA-n) on templated surfaces has drawn a major attention to accurately deposit anisotropic nanoparticles into patterned template with ordered spatial distribution via geometry of confinement. (29; 30; 26) In experiments, the template is a surface-modified substrate in 1D, 2D or 3D significantly larger than the nanoparticles to be deposited. It is served as a templated surface onto which nanoparticles can be selectively induced into complex configuration with a morphology that is complementary to that of the template. The technique is composed of a thin liquid film of nanoparticles suspension sliding over the surface with a well-formed meniscus, followed by nanoparticles self-positioning into topographical cavities. Furthermore, overall pattern of nanoparticles on the templated surfaces can be easily modified with respect to the complexity and scale of template.

Figure 2 displays an example of two-dimensional patterns of Au nanorods deposited on a lithographically-defined surface using DSA. (31) The specific pattern of the template is able to fully determine the assembly of nanoparticles, independent of geometry orientation on template, composition of template/nanoparticle and shape of nanoparticles. Work towards complex nanostructures on templated surfaces using DSA can be achieved using multiple methods such as templated capillary flow, templated dewetting, etc.

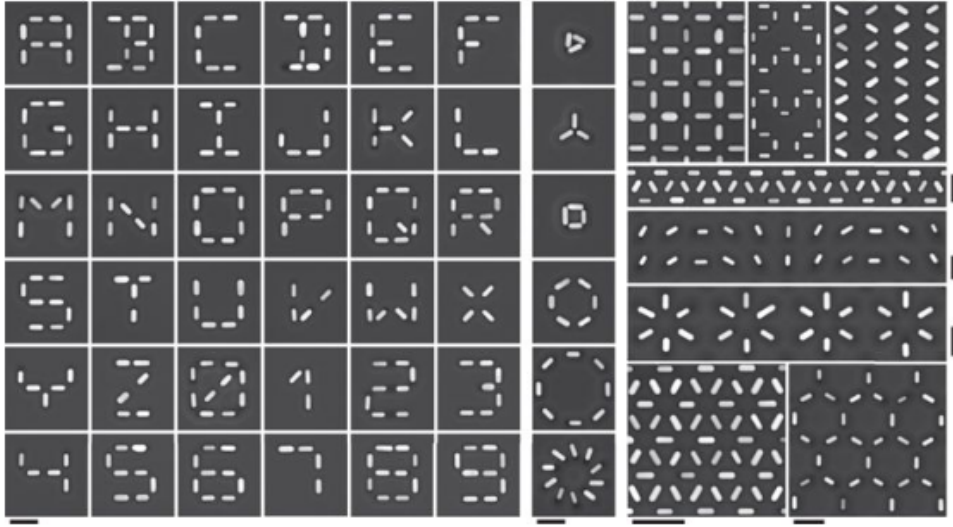


Figure 2: Example of two-dimensional patterns of Au nanorods fabricated on lithographically-defined surface using DSA. All scale bars, 250nm. (31)

Taking advantages of both patterned templates and externally orientated forces, DSA-n on templated surfaces paves new way towards tunable SA of nanostructure with a high degree of lithographic complexity, yield, scalability and advanced functionality for novel integrated applications.

1.2 Applications

DSA-n on templated surfaces offers notable opportunities to create functional materials and devices with sophisticated optical, chemical, thermal and magnetic properties that apply to both emerging technologies and long-existing challenge. Here, I briefly discuss several applications using DSA-n on templated surface.

1.2.1 Plasmonic Devices

Plasmonic nanoparticles exhibit strong interaction with electromagnetic radiation and demonstrate exceptional scattering, absorbance and coupling properties based on their compositions, sizes, geometries and relative positions. Assembling plasmonic nanoparticles on surfaces with proper design of the short- and long-range coupling effects, known as plasmonic metasurfaces, can result in superior enhancement of collective properties beyond single plasmonic nanoparticle, such as the capability to manipulate amplitude, phase, and polarization of light at subwavelength resolution. Such unique properties stimulated growing interest in a variety of chemical and biological applications including plasmonic solar cells, optical probe, imaging below the diffraction and ultrathin invisibility skin cloaks. (32; 33; 34; 35; 36) A common motif is to deposit nanoparticle arrays with required spacing and orientation on a templated surface, which remains a major challenge for top-down lithographic techniques. (37) Recent development in DSA on templated surfaces have provided an opportunity to precisely position plasmonic nanoparticles on a modified surface with the aid of capillary force. (17) The topographic features of the template selectively trap the nanoparticles and define the orientations, without sacrificing the scalability and fabrication cost. The enhanced reproducibility and well-controlled properties through DSA of plasmonic nanoparticles on templated surfaces provide a solid foundation for complex spatial organization that is required for further application.

1.2.2 Semiconducting Nanowire Devices

Semiconducting Nanowire (NW) at the nanoscale presents superior physico-chemical properties and is able to serve as building blocks for field-effect transistors, biosensors, and optoelec-

tronic devices. (38; 39) The fabrication of NW has made impressive progress toward complex, heterogeneous and high-quality nanostructures using tunable materials. (40) Nevertheless, the main challenge resides in post-growth of such sophisticated NW nanostructure in NW-based devices, which require precise positioning of single NW as well as its alignment via less complex and cost effective technique. Collet proposed an innovative DSA approach on templated surface that utilizes both dielectrophoresis (DEP) phenomenon and capillary effect as external directions in assembling NW. (41) In the experiment, NW are locally accumulated in selected region via capillary effect and convective flow, followed by accurate deposition at lithographically-defined surface via DEP field. Moreover, DSA on templated surface using above-mentioned strategy is able to produce NW devices with high accuracy of position and alignment at low cost and large scale.

1.2.3 Photovoltaic Devices

Organic photovoltaic devices (OPV) has drawn a lot of attentions as an alternative clean-energy approach to prevent undesirable climate change. However, the performance of OPV is merely one third comparing to inorganic photovoltaic devices despite its flexibility, customizability and inexpensive cost. One major reason of undesired performance is the random blend of active layers in heterojunction (BHJ) fabrication process, that leads to failures in exciton (electron-hole pair) dissociation and electron transportation. (42; 43; 44; 45) The strategy of ordered bulk heterostructure (OBHJ) demonstrates great potential to address above issues by aligning ordered inorganic semiconductor such as ZnO nanorods and TiO₂ nanorods in polymer phase, as a hybrid OBHJ structure. (17; 46; 47; 48) Whereas controlling the spacing and

ordering of nanorods array with the required precision represents significant challenge with respect to scalability. Recent development has proposed a DSA approach on templated surface to achieve the hybrid OBHJ morphology with well-controlled alignment of nanorods arrays across multiple length scale via capillary flow field. (49) Additionally, DSA of OBHJ on templated surface provides a scalable fabrication platform for nanorods arrays with various shapes, sizes and orientations.

1.3 State of Art

DSA-n on templated surfaces is drawing increasing attentions, and has been extended to numerous applications. (50; 51) In spite of its extraordinary advantages in precise positioning, tunable arrangement, convenient process and scalable fabrication, complete understanding of the dynamics and the parametric relation to its performance is still elusive. The transfer of nanoparticles from suspension in liquid film to a templated surface requires appropriate modification of surface that makes it receptive to nanoparticle attachment. Lithographic patterning of such surface partially controls the dynamics by providing means to capture nanoparticles at well-defined target sites with remaining surface clean when the exposure to liquid film is over. In addition, local flow field in liquid film plays a significant role by continuously supplying sufficient nanoparticles to the templated surface region for deposition.

1.3.1 Dynamics of DSA-n on Templated Surface

Various studies have hypothesized three sequential stages (accumulation, trap and drying) for the dynamics of DSA-n on templated surfaces. (31; 37; 52) Figure 3 illustrates the trajectory

of a single nanoparticle from initial suspension in liquid film to final deposition on a templated surface.

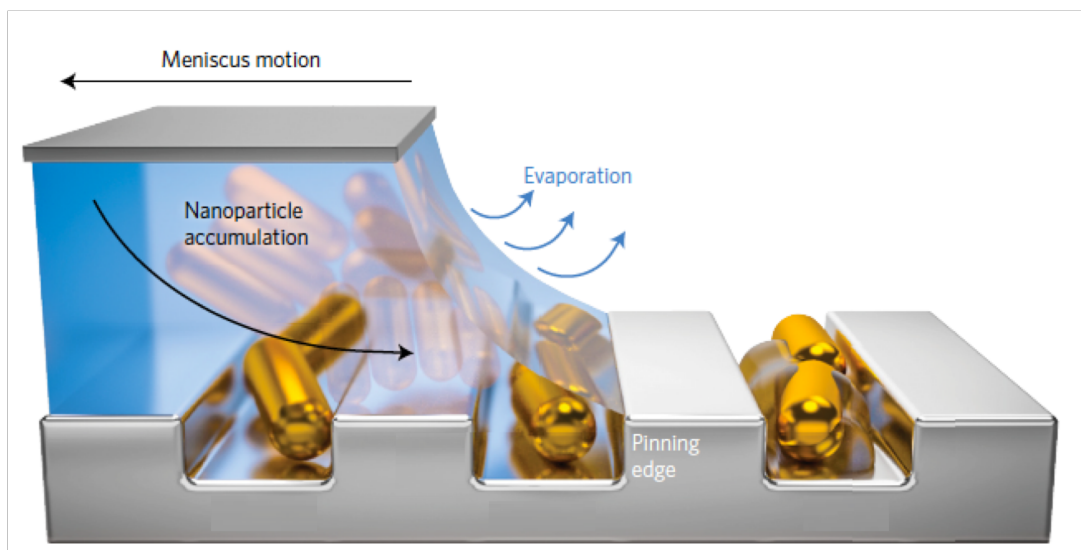


Figure 3: Schematic of DSA-n on a templated surface, displaying the sequential stages of nanoparticle assembly from initial suspension in liquid film to final deposition on the templated surface. (50)

As shown in Figure 3, the experiment is performed by dragging the top planar substrate with a constant velocity in parallel to pre-defined substrate, leaving a liquid film of nanoparticles suspension in between substrates. (50) In this experiment, it is hypothesized that the surface tension helps form the most energetically favorable contact angle at the three phase contact line in receding meniscus.

The evaporation across the surface of receding meniscus creates a convectively laminar flow that brings nanoparticles towards contact line while receding meniscus drags suspended nanoparticles in the opposite direction. Within the accumulation zone of nanoparticles at the contact line, pile-up structures or multiple monolayers with short range ordering are formed adjacent to the templated surface with a higher local density of nanoparticles. In the absence of topographical cavities, receding meniscus is able to effectively drag nanoparticles across a flat surface. Once the topographical cavity is encountered, the contact line becomes distorted and gets pinned by the edge of cavity, presenting a more stretched contact line than that on flat surface around the cavity. The combination effect of convective flow, locally high density of nanoparticles and Brownian motion helps insert nanoparticle into the cavities. As the majority of liquid film moves constantly, the increasing stretch of contact line at pinning edge leads to reduction of contact angle, acting as a clamping force to trap nanoparticle inside until the pinning contact line detaches from cavity. The clamping force also aligns nanoparticles inside cavity along the receding direction of meniscus if cavity is larger than the size of nanoparticle. After the nanoparticle is trapped in the cavity, it is then fixed at its position by local capillary force until the surrounding liquid dries.

Overall, DSA-n on templated surfaces utilizes the receding contact line as a guide to accumulate and drag large numbers of nanoparticles over a lithographically-defined surface that is designed to pin the contact line and trap these nanoparticles at pre-defined locations. Enhancement of assembly performance is mainly focused on optimization of accumulation zone design and the templated surface design, which will be discussed in the following sections.

1.3.2 Design of Templated Surface

By providing guidance for nanoparticle deposition, proper design of topographical cavity in terms of size, depth, shape and alignment is the key to achieve assembly on lithographically-defined surface.

The size of topographical cavity can be geometrically tailored to capture individual or a cluster of nanoparticles depending on their size. It has been reported that a large cavity is able to accommodate multiple nanoparticles in the similar mechanism; nonetheless, the assembly of a cluster of nanoparticles in a cavity is strongly influenced by interaction between nanoparticles. (53; 54) Particle-particle interaction can either facilitate the assembly process by attracting nearby nanoparticles into close proximity or hinder it through repulsive forces that push nanoparticles out of cavity.

The depth of topographical cavity also has a critical impact to assembly process that provides resilience against the recession of meniscus. For example, a shallower cavity can only deposit one nanoparticle even though the area is large enough to accommodate multiple. (53) It is hypothesized that the topographical cavity must be deep enough to pin the meniscus and form required paths from accumulation zone to the cavity. On the other hand, deeply embedded nanoparticles in the cavity may have reduced functionality in further applications.

The shape of the topographical cavity has been studied and a variety of shapes for nanoparticles have been explored. (55; 54; 31) Recent studies showed that the assembly of nanoparticles with complex structure such as nanotriangles and nanoarrows could also be achieved by tailoring the shape of the topographical cavity. (55; 56) Additionally, DSA of such complex nanoparticles

on templated surfaces have been explored to produce a reasonably high yield. Shape-assisted strategy also presents an opportunity for the template design with a shape-selective capability that filters undesired nanoparticles from a mixture with impurity. Besides complexity, the shape of topographical cavity has been discovered to be able to control the alignment and orientation of nanoparticles, with the aid of receding meniscus. (57; 58) Other studies also focused on the modification of straight-end cavity, by introducing a funnel-shaped edge or adding an adjacent auxiliary sidewall, that improve the assembly yield. (31)

The alignment of topographical cavity has been broadly explored for achieving high yield assembly, surprisingly, similar yield of nanoparticles deposition have been demonstrated regardless of the alignment relative to receding contact line, parallel or perpendicular. (57) A plausible hypothesis was provided that sufficiently extended receding meniscus is able to host enough nanoparticles with random orientation at the bottom layer by the lithographic cavities such that at least one that crosses a single cavity, can tightly match its orientation. (31)

1.3.3 Design of Accumulation Zone

The accumulation zone, where nanoparticles stack up at receding meniscus, acts as a transition system for the assembly process in which it collects disordered nanoparticles, orders them in stacks and sends them to topographical cavities for further deposition.

The key prerequisite for high yield assembly is the accumulation zone, where the liquid film is densely packed with nanoparticles. It is not only to ensure the supply of nanoparticles in accumulation zone that needs to be commensurate with the demands of SA process on the templated surface, but also suppresses the Brownian motion, specifically, mobility of nanoparticles in order

to increase the probability of successful deposition. (52; 10) The crowd of complex nanoparticles (nanorods, nanocubes, nanoprisms, etc.) within the accumulation zone however, may result in demands of stabilizing ligand shell around nanoparticles against agglomeration. (9)

The shape of accumulation zone also plays a key role in establishing a proper SA environment. (9; 53) If the receding contact angle is too large, tending to be hydrophobic, then the wedge-shaped geometry is difficult to form that accumulate nanoparticles for later deposition. If the receding contact angle is too small, tending to be hydrophilic, the highly stretched pinning effect may break the path of the nanoparticle assembling into topographical cavity. The templated surfaces are often chemically treated or intentionally selected to form an optimum contact angles at approximately 50° , that also helps facilitate local ordering of nanoparticles within accumulation zone. (52; 31) A significant degree of ordering, with respect to each other and relative to the receding contact line, within proper shape of accumulation zone has been confirmed in several studies considering nanorods, nanocubes and nanoprisms. (31; 57; 55)

Another influencing factor is the velocity of receding meniscus that is normally driven by another substrate or gravity. It needs to be optimized to avoid detrimental flows that may take nanoparticles away from the accumulation zone. Optimal velocity is typically at a few micrometers per second, which is also considered to be the practical condition.

Evaporation of liquid at receding meniscus is also considerably critical in the SA process as it may affect the convective flow in collecting nanoparticles at the accumulation zone. A study has shown that controlling the convective flow created by evaporation can easily be achieved by adjusting the temperature of accumulation zone through the substrate. (52) In the assembly

process, tuning the temperature is able to either promote the deposition speed of nanoparticles, or the reversal.

1.3.4 Computational Modeling

There has been numerous studies in DSA-n on templated surfaces with various kinds of structural complexity; however, most of them have focused on deposition of nanoparticles of size 50 nm or larger.

Apart from the fabrication difficulty of sub-10 nm particles and the associated topographical cavities on a surface, deposition of such nanoparticles using above-mentioned receding meniscus over a templated surface cannot avoid random assemblages. (58) Moreover, particles at sub-10 nm are too small to observe their SA process using optical microscopy; hence, the underlying mechanism has remained unclear. Additionally, the high cost of fabrication of sub-10 nm particles and the corresponding templated surface is another obstacle for experimental studies in order to discover the parametric relation between ultimate ordering and nanoparticles geometry and functionality, and the template geometry.

To address above difficulties, computational modeling has been utilized. Recent progress in DSA of sub-10 nm nanoparticles on templated surfaces has shown the dominant effect of pairwise interaction and Brownian motion in the SA process. (59) At sub-10 nm length scale, size of nanoparticles is much smaller than the length of receding meniscus; therefore, convective flow is not the major factor that controls the motion of nanoparticles. Instead, Brownian motion and pairwise interaction forces strongly affect the dynamics; thus, creating the undesirable random assembly on the surface. A strategy has been shown to harnesses the interactions

(both attractive and repulsive forces) between nanoparticle, the template and the surrounding liquid in DSA of sub-10 nm nanoparticles in nanochannels. (58)

Using Brownian Dynamics (BD) simulations, it has also been confirmed that the majority of alignment and self-assembly configuration of nanoparticles does not change with respect to the direction of meniscus motion; on the contrary, it is well-formed before the receding meniscus reaches to the deposition site. (59) It has been hypothesized that nanoparticles are collected at the accumulation zone due to the combined contribution of convective flow and capillary force attraction. The attractive force further increases the local density of nanoparticle, pushing nanoparticles mostly into the repulsive regime of pairwise interactions. Once the deposition is completed, the ordering of nanoparticles within channel-shaped cavity is arranged by the coupled nanoparticle-nanoparticle repulsion and capillary force attraction.

The role of liquid film thickness and contact angle has also been explored in large area DSA of sub-10 nm particles with single particle resolution using BD simulation. (60) Large liquid thickness and contact angle are suggested to hinder deposition process by presenting energetically favorable hexagonally ordered clusters in the bulk, while the opposite conditions facilitate SA process by slightly reducing possible nearest interactions. Despite above-mentioned experimental and theoretical works on DSA-n, its mechanism and dynamics of nanoparticles are not well understood due to the several contributing driving forces and difficulty in imaging the SA process and receding interface in real time.

1.4 Thesis Outline

To further investigate the key mechanism in DSA of sub-10 nm particles on templated surfaces, it requires accurate understanding of the dynamics of thin liquid film spreading over the substrate, accounting for the impact of gravitation and interfacial tension, which will be discussed in chapter 2.

In chapter 3, an appropriate computational model will be established for versatile studies that help delineate the effects of lithographically-defined surfaces in the advancing of thin liquid layers.

Pinning phenomenon of receding meniscus over substrate, effect of cavity topography on pinning strength, and internal flow field of accumulation zone will be discussed in chapter 4.

In chapter 5, we develop a model to simulate a template-riven DSA-n at sub-10 nm, within which multiple parameters including liquid film properties and template designs are to be explored in order to unravel the mechanism of DSA-n and to obtain a high yield.

Understanding the complex energetics in DSA-n is crucial to help optimize the experimental design and thus improve the yield. We report a model that is able to obtain work, free energy and entropy variation during DSA-n in chapter 6.

We also propose future plans in chapter 7, in which we provide directions to be investigated by taking advantage of the model we constructed. The idea and strategy may suggest a potential path to achieve high yields of DSA-n in experimental designs.

CHAPTER 2

A PREDICTIVE MODEL TO PROBE THE IMPACT OF GRAVITY AND SURFACE TENSION ON RISING WETTING THIN FILMS

Reprinted with permission from (Luo, Z. and Mehraeen, S.: Predictive model to probe the impact of gravity and surface tension on rising wetting thin films. Langmuir, 35(11):4189-4196, 2019). Copyright (2019) American Chemical Society.

2.1 Introduction

The spreading of liquid films on solid surfaces at nanometer scale plays a significant role in numerous technologies, including but not limited to painting, coating, micro-reactor and chemical sensors, which have received great attention over a century. (61; 62; 63; 64; 65) Recently, it was also shown that spreading liquids on solid surfaces can be applied to controllably position sub-10 nm particles into lithographically defined templates. (58; 60; 59) The development of these applications requires accurate knowledge of underlying dynamics of spreading, especially on surfaces with interfacial interactions occurring over a scale ranging from molecular distance to capillary length. At macroscopic scales, spreading of liquid films is precisely described by hydrodynamic theories that ignore the molecular structure of liquids. (66; 67; 68; 69; 70) At microscopic scale however, the origin of the universal laws that govern the spreading dynamics is not well understood.

The appearance of a spreading liquid film has been found to start from the formation of a molecularly thin liquid layer on the substrate. (71) This thin liquid layer spreads along the substrate faster than the rest of the liquid film. Using dynamic ellipsometry and x-ray reflectivity measurements, (72; 73; 74; 75; 76; 77; 78; 79; 80) it has been shown that on atomically smooth surfaces, one or few of these thin films advance faster than the macroscopic liquid film edge. Subsequently, this macroscopic liquid film spreads on top of such thin liquid layer, which may fuse into macroscopic extent at sufficiently long time. For nonvolatile liquids, it has been established that the linear extent of the thin layer grows proportional to \sqrt{t} , regardless of the nature of the species involved. (72) The law of \sqrt{t} has been verified with different substrates and liquids in which the bottom thin liquid layer directly in contact with substrate spreads much faster. (73; 74; 75) Similar experiments performed for capillary rise geometries in which a thin liquid layer creeps upward on a solid wall, have also shown that the height of the liquid layer increases as \sqrt{t} within certain time domain until the thin layer is broken by gravity. (76; 77) As such, the universal law of \sqrt{t} seems to be independent of the substrate, liquid, geometry as well as the size of the liquid molecules.

Computational approaches have been utilized to reveal the mechanism behind the rise of the thin liquid layer, and explain the time dependence of spreading. Several theoretical models have been proposed, (50; 81; 82; 83) and Molecular Dynamics (MD) and Monte Carlo (MC) simulations have been performed. (84; 85; 86; 87; 88; 72; 89) In particular, Burlatsky *et al.* have proposed a microscopic 1D model, (72) which allows mass transport from reservoir to mono-molecularly thin layer, while its spreading is restricted by surface tension applied at the

solid-liquid interface. The height of the thin layer was found via MC simulations to follow $\sim \sqrt{t}$. Using Kinetic Monte Carlo (KMC) simulations, Abraham *et al.* proposed a 3D lattice gas model predicting \sqrt{t} time dependence of the rise. (82) Above mentioned models however, ignore the impact of gravity on the vertical spreading of the thin liquid layer.

In this chapter, we present a 3D Ising lattice gas model to describe the rise of a thin liquid film against the gravity, and explain its fine structure. In our microscopic model, we account for the impact of gravity, surface tension, cohesive energy between liquid and substrate, and interaction energy between liquid particles on the rise of the liquid layer. Utilizing KMC simulations, we show that our model establishes the \sqrt{t} behavior of rising liquid layer in the zero to low gravity regime, which is consistent with the original 2D Ising model in the absence of gravity studied before. (82) Additionally, we analyze the dynamics of spreading while varying gravitational acceleration, and surface tension. We report the impact of above mentioned parameters on the solid-liquid interface displacement, instantaneous interface velocity, and roughness.

2.2 Theoretical Model

Our lattice gas model mimics the experiment in which a substrate is partially immersed vertically into a liquid bath. Upon partial immersion, a macroscopic meniscus at the solid-liquid interface is created, followed by formation of a very thin liquid layer climbing up the vertical substrate against the gravity. We introduce a lattice model in which the dynamics of the thin liquid layer is represented by motion of particles, which consist of liquid molecules, restricted to a 3D lattice. Every lattice site in this model can either be vacant or occupied by

a liquid particle. In addition, the edge of the thin liquid layer, which represents the solid-liquid interface, is modeled by the dynamic boundary formed by the moving outermost particles.

We define a square lattice with unit lattice spacing $\Delta x = \Delta y = \Delta z = 1$ along x -, y -, and z -direction, respectively. We then specify the position of particles moving on the 3D square lattice by the position vector $\vec{r} = (x, y, z)$. Without loss of generality, we assume that z can only be 1 or 2, meaning that only two layers of particles parallel to the substrate are considered. Adding more layers will only slow our KMC simulations while it does not affect the dynamics of solid-liquid interface.

We define the dimensionless change in total energy for a given particles configuration in which a particle moves from site i to j by

$$\frac{\Delta E_{i \rightarrow j}}{kT} = \Delta G_{i \rightarrow j} + \Delta J_{i \rightarrow j} + \Delta A_{i \rightarrow j} + \Delta F_{i \rightarrow j}. \quad (2.1)$$

The first term in Equation 2.1 denotes the work done by the gravity

$$\Delta G_{i \rightarrow j} = (y_j - y_i)g', \quad (2.2)$$

in which y_i and y_j are the y -coordinates of the site i and j , respectively, $g' = mg\Delta y/kT$ is the dimensionless gravitational acceleration, m is the particle mass, g is the dimensional gravitational acceleration, k is the Boltzmann constant, and T is temperature.

The second term in Equation 2.1 is the contribution from particle-particle interaction denoted by

$$\Delta J_{i \rightarrow j} = (n_j - n_i)J, \quad (2.3)$$

where n_i and n_j are the total number of bonds with the nearest neighbors to be broken and made at site i and j , respectively, and J is the cohesion strength between neighbor particles, (81; 82) nondimensionalized by kT .

The third term in Equation 2.1 indicates the contribution from van der Waals interaction of liquid particles with the substrate characterized by the Hamaker constant $A > 0$, (81; 90; 91)

$$\Delta A_{i \rightarrow j} = A \left(\frac{1}{z_j} - \frac{1}{z_i} \right), \quad (2.4)$$

where z_i and z_j are the z -coordinates of site i and j , respectively, which can be either 1 or 2, corresponding to the bottom or top layer, respectively.

Interfacial energy at the solid-liquid interface is expressed by the last term in Equation 2.1

$$\Delta F_{i \rightarrow j} = \sigma(y_j - y_i), \quad (2.5)$$

where $\sigma = \gamma \Delta x \Delta y / kT$ is the dimensionless surface tension, γ is the dimensional surface tension at the interface, and Δx and Δy is the lattice constant along the x - and y -direction. (92)

Figure 4A illustrates the 3D lattice model, where y is the axis perpendicular to the liquid bath (not shown). For clarity, we are not showing the underlying lattice grid. In Figure 4A, red

particles indicate the top layer of the liquid bath, blue and gray particles illustrate the top and bottom layers, and green particles depict the edge of the rising liquid layer where the surface tension is applied to particles vertical hops. Figure 4B depicts the cross section of the rise of liquid layer, representing the four components of the energy change described in Equation 2.1.

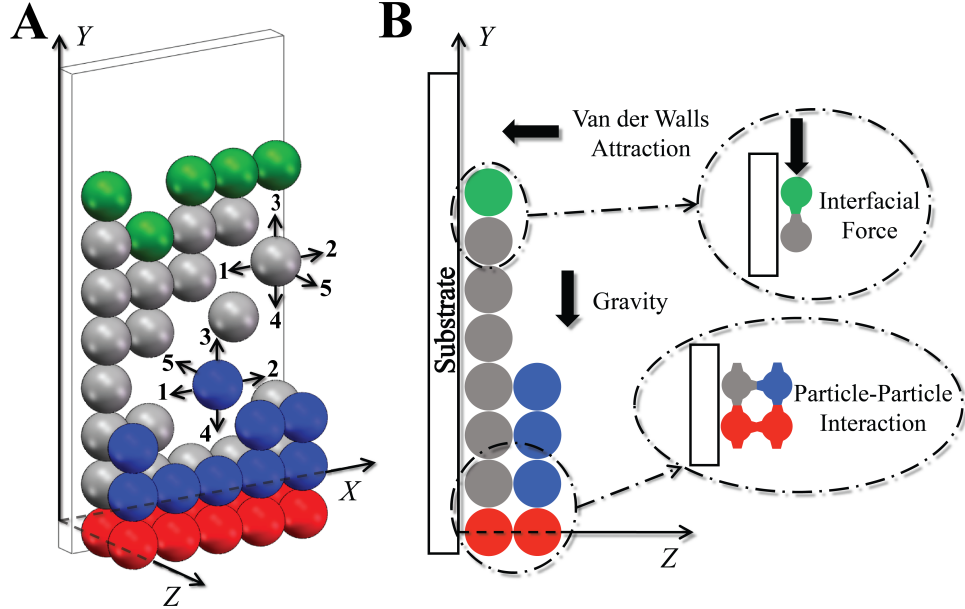


Figure 4: (A) The 3D schematics of the Ising lattice gas model, illustrating the rise of the liquid layer on the vertical substrate. Red particles represent the bulk liquid, gray and blue particles show the first and second layer of particles located at $z = 1$ and 2 , respectively, and green particles illustrate the solid-liquid interface. Numbered arrows show four in-plane and one out-of-plane nearest neighbors. (B) Cross section of the schematics, depicting the four component of the total energy, gravity, van der waals interaction with the substrate, nearest neighbor particle-particle interaction (bottom inset), and interfacial energy (top inset).

Now, we parameterize the KMC simulations of the rise of the wetting liquid film, and describe the steps therein. Then, we present the statistical results for the impact of gravity and surface tension on the average interface displacement, instantaneous velocity, and interface roughness of the liquid layer and its structure factor.

In our Ising lattice gas model, the mechanism of KMC simulations is to stochastically explore sequences of diffusive hops, by selecting events proportional to their transition rates. (93) According to the continuous time random walk, (94) the rate of transition is the particle-vacancy exchange rate from site i to site j defined by Kawasaki dynamics: (94)

$$r_{i \rightarrow j} = \nu \exp \left(-\frac{\Delta E_{i \rightarrow j}}{2kT} \right), \quad (2.6)$$

where $r_{i \rightarrow j}$ is the rate of a particle hopping from site i to j , and ν is the attempt frequency, which we set to the inverse of the number of destination sites. In our 3D model, for every hop, the number of destination sites is 5, *i.e.* As illustrated in Figure 4A, the gray particle at $z = 1$ has four in-plane and one out-of-plane direction whereas the blue particle at $z = 2$ has four in-plane and one into-the-plane direction to move, all indicated by arrows. In general, the total possible destination sites is five, which is the same as number of nearest neighbors regardless of their occupation. According to Equation 2.6, the rate of a given particle moving in a given direction certainly depends on the energy change for that move, or in essence, the details of local particles configuration.

We follow the definition of stochastic process in KMC method, and ensure the coordinate scale, maximum number of particles, and total KMC steps to be large enough to avoid finite-size effect. The steps in our KMC simulations are as follows:

1. As for the initial condition, we set the occupation number of all source sites (any $x, y = 1$, and $z = 1, 2$) to 1 (filled with particles). After a KMC hop at some later time, if any of these source sites becomes empty, we will fill it with a particle instantly. Thus, source sites are maintained as occupied at all times $t > 0$.
2. The rise of liquid layer takes place along y -direction. Therefore, we apply periodic boundary conditions along x -direction.
3. To achieve a high degree of non-volatility, we set the non-dimensionalized particle-particle interaction parameter, J , and van der Waal parameter, A , large enough to be in complete wetting regime. (95)
4. We calculate rates for all possible hops of particles using Equation 2.6. Here, $\Delta E_{i \rightarrow j}$ is the energy change before and after a particular hop.
5. We select a move by randomly choosing a hop from the list of all possible hops proportional to the hopping rates.
6. We increment the KMC time by Δt (in KMC time unit), which is the time that has elapsed during one KMC step, given by:

$$\Delta t = -\frac{\ln(\rho)}{\sum_{\substack{i,j \\ i \neq j}} r_{i \rightarrow j}}, \quad (2.7)$$

where $0 < \rho \leq 1$ is a uniformly distributed random number. (96)

7. If a particle moves beyond $y = L_y$ (top side of the simulation box), its rates will be removed from the list of possible hops, not to be selected in the next selection cycle.
8. We update the new hopping rates, and repeat from step 5.

We define the simulation box size as $L_x = 100$ (*i.e.* $1 \leq x \leq 100$) unless otherwise mentioned, $L_y = 300$ (*i.e.* $1 \leq y \leq 300$), and $L_z = 2$ (*i.e.* $1 \leq z \leq 2$), and set the thermal energy to $kT = 1/3$ throughout all KMC simulations.

2.3 Results and Discussion

2.3.1 Progression of rising liquid film

With the setup above, we now look at the impact of gravity, g' , and surface tension, σ , on the growth and interface roughness of the rising liquid layer.

Figure 5 illustrates KMC simulation results, from left to right, depicting 10 snapshots of the rise of the liquid layer along the vertical substrate in the absence of gravity and surface tension. As shown in Figure 5, the first layer illustrated in gray, which is closer to the substrate, moves upward faster than the second layer, shown in blue. This is because as particles in the first layer diffuse along the solid-liquid interface, vacancy defects are generated which diffuse downwards. Lowering van der Waals interaction, particles move from the 2nd layer ($z = 2$) to the 1st layer ($z = 1$) to fill the vacancy defects. As such the 1st layer advances faster than the 2nd layer. Once these vacancy defects reach to the bulk liquid at $y = 1$, they are immediately filled with new particles. Therefore, the rise of the bottom layer is due to the combined effects of vacancies advancing into the liquid bath, and the supplement from the 2nd layer of particles.

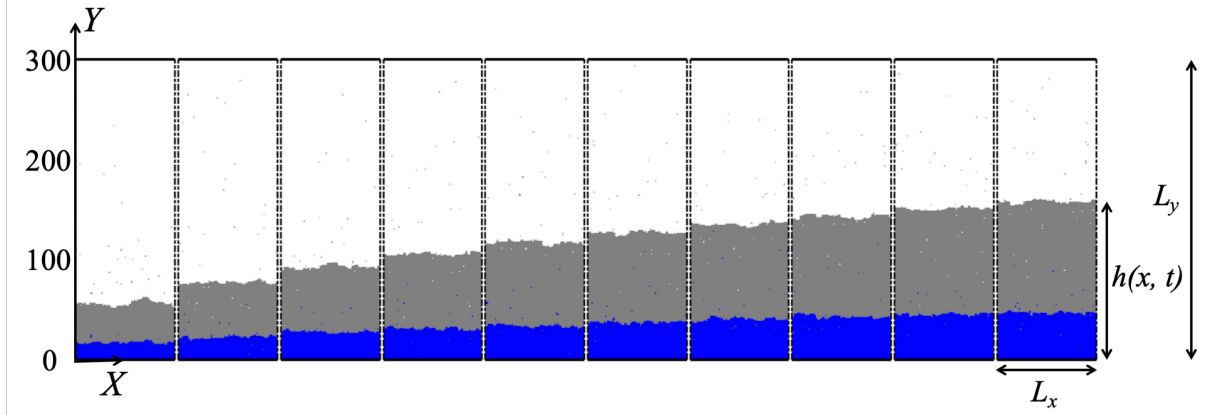


Figure 5: Top view of 10 snapshots, illustrating the rise of the liquid layer at different times, $t = 1 \times 10^7, \dots, 10 \times 10^7$ with the interval of 10^7 in KMC time unit. Occupied sites at $z = 1$ and 2 are shown in gray and blue, corresponding to bottom and top layer, respectively. Empty sites are shown in white. Parameters used are $A = 30$, $J = 3$, $g' = 0$, $\sigma = 0$.

Our results in Figure 5 also indicate that as particles diffuse and move up vertically, they create a connected path through their nearest neighbors from the top at solid-liquid interface to the bottom at the bulk liquid. We also observe free particles, without nearest neighbors, on the substrate above the solid-liquid interface, indicating the vapor phase. As these free particles diffuse, they either move downward and eventually get absorbed at the solid-liquid interface, or move upward and exit the simulation box in which case we remove the particles from the group of simulating particles. Defining the 1st layer of liquid by those particles connected through their nearest neighbors only, we now look at the average interface displacement of this 1st layer of particles and its progression in time.

2.3.2 Impact of gravity

To study the dynamics of average interface displacement of the rising liquid layer, we record the maximum local height of connected sites, $h(x, t)$, for $x = 1, 2, \dots, L_x$ at all times, $t > 0$. Averaging over independent simulations, we find the average interface displacement, $\bar{s}(t)$, measured from initial configuration ($y = 1$), written as:

$$\bar{s}(t) = \frac{1}{L_x} \sum_{x=1}^{L_x} \langle h(x, t) \rangle - 1, \quad (2.8)$$

where $\langle \dots \rangle$ stands for average over 200 independent KMC simulations for every x value while all other parameters (g' , A , J , and σ) are unchanged.

In Figure 6A, we present the results for the dynamics of the rising liquid layer for different gravitational acceleration constant, g' . In the absence of gravity (red curve, $g' = 0$), our results exhibit an initial ballistic dynamics, approximately varying linearly with time, *i.e.* $\bar{s}(t) \sim t$, followed by a diffusive dynamics, $\bar{s}(t) \sim \sqrt{t}$. We note that our results slightly deviate from true ballistic motion in which $\bar{s}(t)$ is exactly proportional to t . We attribute this deviation to the confinement along z -directions as we have considered only two layers at $z = 1$ and 2 . Overall, this result is in agreement with the experimental results performed for capillary rise geometries. (76; 77)

As gravitational acceleration, g' , increases, the long time dynamics deviates from universal law of \sqrt{t} . The results suggest that gravity slows down the rate of upward wetting with average interface displacement $\bar{s}(t) \sim t^\alpha$, where $\alpha < 1/2$. Furthermore, we notice that gravity does not

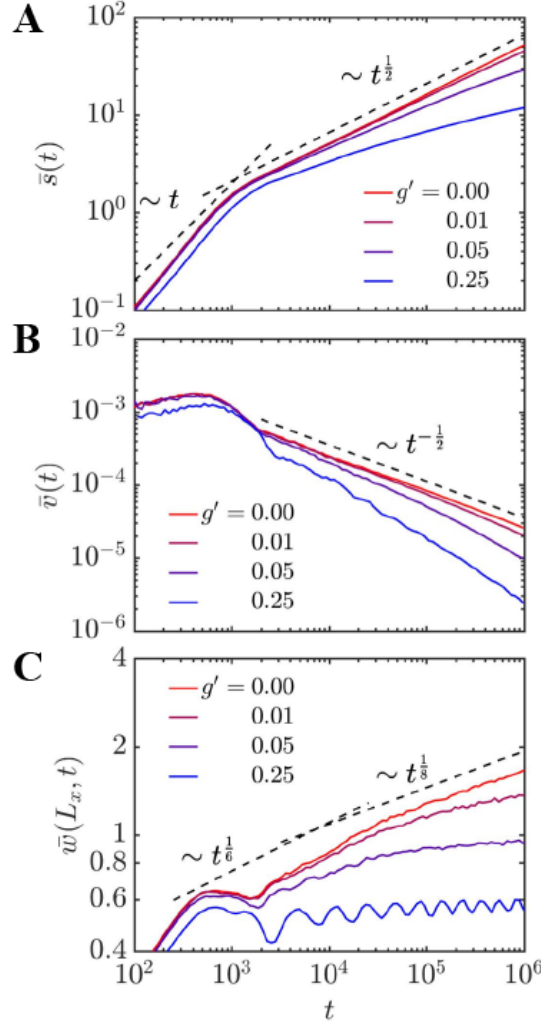


Figure 6: Log-log plot of evolution of the (A) average interface displacement, (B) instantaneous interface velocity, and (C) interface roughness of the rising liquid layer with time, t , in KMC time unit. Solid lines are averages over 200 independent KMC simulations with $A = 30$, $J = 3$, $\sigma = 0$, and $g' = 0, 0.01, 0.05$ and 0.25 , from red to blue, respectively. Dashed lines are the guide for the eye.

change the rate of wetting ($d\bar{s}(t)/dt$) at shorter times while it reduces the rate at longer times.

Although there is a small shift in $\bar{s}(t)$ at short time (blue curve in Figure 6A compared to the

red curve has shifted towards longer times), the rate of wetting has not changed at small time scales. This means that the rate of increase in average interface displacement is not affected by the gravity since the average interface displacement still advances linearly with time, *i.e.* $\bar{s}(t) \sim t$. One can also see this impact of gravity on the dynamics of wetting by looking at the instantaneous velocity of the edge of the liquid layer at $z = 1$.

The instantaneous velocity of the edge of the liquid layer (interface velocity) is subsequently calculated from time derivative of the average interface displacement, $\bar{s}(t)$:

$$\bar{v}(t) = \frac{d\bar{s}(t)}{dt}. \quad (2.9)$$

Figure 6B, illustrates the interface velocity as time progresses for the same values of gravitational acceleration, g' , shown in Figure 6A. According to Figure 6B, one can clearly see the deviation of interface velocity from universal law of $1/\sqrt{t}$ as the gravitational acceleration increases. We also notice that the interface velocity at small time scales ($t < 10^3$) slightly deviates from the constant $\bar{v}(t)$ for true ballistic motion. As discussed above, we attribute this deviation to the artificial confinement along z -direction applied to our Ising lattice gas model where particles can only hop between $z = 1$ and 2 planes.

The time dependent interface roughness is the standard deviation from average interface displacement, $\bar{s}(t)$, given by

$$\bar{w}(L_x, t) = \sqrt{\frac{1}{L_x} \sum_{x=1}^{L_x} \langle (h(x, t) - \bar{s}(t))^2 \rangle}. \quad (2.10)$$

Figure 6C illustrates the evolution of interface roughness in time, calculated from Equation 2.10 for the same values of gravitational acceleration shown in Figure 6A and B. In the absence of gravity, our result in Figure 6C is in clear qualitative agreement with the previous study conducted by Abraham *et al.* (82) As predicted by others, (82; 97) in the absence of gravity, we also observe the cross over in $\bar{v}(t)$ from $t^{(1/6)}$ at intermediate times to $t^{(1/8)}$ at longer times shown by dashed lines in Figure 6C. We also find that as gravitational acceleration, g' , increases from 0 to 0.25, depicted from red to blue in Figure 6C, respectively, the growth of interface roughness starts deviating from $t^{(1/6)}$ and $t^{(1/8)}$, at intermediate and longer times, respectively. In particular, when $g' = 0.25$ (blue curve in Figure 6C), our result seems to suggest that there will be no overall growth in interface roughness.

The impact of gravity on the interface displacement, and roughness of the rising liquid layer can also be explained using the energy change of the MC hops in Equation 2.1. According to this equation, gravity lowers the energy barrier for downward hops; hence, rates of downward hopping increase, leading to an overall directional diffusion downwards. Further increase in gravitational acceleration will completely hinder upward hopping, resulting to almost no growth in the interface displacement (not pictured). As for the interface roughness, gravity helps dampen fluctuations at the solid-liquid interface by lowering rates of upward hops, which will be energetically costly for large values of gravitational acceleration. In particular, for $g' = 0.25$ shown blue in Figure 6C, interface roughness ceased to increase in time, leading to an overall constant value.

To better understand the extent of dimensionless gravitational acceleration, we compare different dimensionless and dimensional gravitational acceleration values. For this comparison, we assume the lattice spacing used in KMC simulations to be equal to the diameter of the simulating particles. This assumption is consistent with our particle representation in Figure 4A. Furthermore, taking the particle diameter to be $\Delta x = \Delta y = \Delta z = 447$ nm, and the rising liquid to be water with density of 1000 kg/m^3 , we find the particle mass to be $4.68 \times 10^{-17} \text{ kg}$. We also nondimensionalize the energy by $kT = 4.11 \times 10^{-21} \text{ J}$. Using the relation for dimensional gravitational acceleration in Equation 2.2, we present the mapping between dimensionless and dimensional gravitational acceleration, g' and g , respectively, in Table I. It is noteworthy that g can be tuned experimentally using a centrifugal adhesion balance (CAB) equipment developed by Tadmor *et al.* (98; 99; 100; 101)

In CAB, a centrifugal arm holds the substrate at one end while rotating perpendicular to the gravitational field. With a setup in which the substrate is hanging from a hinge like a pendulum, and $0 \leq \alpha \leq 180^\circ$ being the counter clockwise angle between the vertical line going through the hinge (axis of rotation) and substrate, the gravitational acceleration along the substrate will be $R\omega^2 \sin(\alpha) + g \cos(\alpha)$. Here, ω is the angular velocity, and R is average distance of the liquid film from the axis of rotation. With this definition of R , we are assuming variation of R along the liquid film is negligible. Obviously, depending on α being smaller or larger than 90 degrees, one would increase or decrease g with ω , respectively. With this setup, the force perpendicular to the substrate, which is $R\omega^2 \cos(\alpha) - g \sin(\alpha)$, is mapped on to the Hamaker constant A in Equation 2.4. These are the steps we envision for experimental verification of the

KMC simulations. However, additional work is still warranted to perform above experiment and verify the simulation results shown in Figure 6, which is left for a future research.

TABLE I: THE MAPPING BETWEEN DIMENSIONLESS AND DIMENSIONAL GRAVITATIONAL ACCELERATION

g'	g (m/s ²)
0	0
0.01	1.97
0.05	9.83
0.25	49.2

2.3.3 Impact of surface tension

Now, we turn into the impact of surface tension, in the absence of gravity ($g' = 0$), on the dynamics of the rising liquid layer. In rising liquid layer, dynamics of solid-liquid interface is directly impacted by the surface tension as formulated in Equation 2.1 and Equation 2.5. According to this dynamics, the surface tension only affects the particles at solid-liquid interface. Essentially, interfacial tension tends to minimize the length of solid-liquid interface; therefore, interfacial perturbations with large wave lengths become energetically costly to form. In KMC simulations, surface tension will penalize the total energy change associated with hops that create perturbation in positive y -direction; thus, making upward movement energetically unfavorable. This leads to lowering the likelihood of selecting interface particles tending to move along positive y -direction, rendering a delay in the rise of the liquid layer. We observe this

delay (a shift in time) in the progression of interface displacement by increasing dimensionless surface tension parameter, σ , from 0 to 3.2, corresponding to red to blue curves in Figure 7A, respectively. Results in Figure 7A suggest that the surface tension does not alter dynamics of the liquid layer as it still exhibits an initial rise slightly larger than t , followed by a diffusive dynamics with interface displacement proportional to \sqrt{t} . We speculate that this small deviation of interface displacement from linearly varying at short time might be due to the confinement considered along the z -direction in our 3D model. Nonetheless, these results from our 3D Ising lattice gas model are in qualitative agreement with the previous work reporting the growth of liquid film height using a one dimensional Ising model. (72)

Interface velocity profile of the rising liquid layer is shown in Figure 7B for the same range of surface tension depicted in Figure 7A. The small deviation in interface displacement from ballistic move at short time exhibits small deviation in the interface velocity illustrated in Figure 7B as well. According to Figure 7B, we estimate this deviation in the interface velocity to be in the order of $\sim 10^{-3}$. Our results also suggests that increasing surface tension, shown from red to blue in Figure 7B, lowers the interface velocity at short time. This impact is more pronounced compared to that at long time as the shifts of interface velocity in time is larger at short time.

Interface roughness, $\bar{w}(L_x, t)$, is also affected by the surface tension in that as surface tension increases, evolution of perturbation at the interface is retarded, leading to a delay in growth of interface roughness. This delay is manifested by a shift toward larger time, as illustrated in Figure 7C with σ being the same as those in Figure 7A and B, increasing from red to blue,

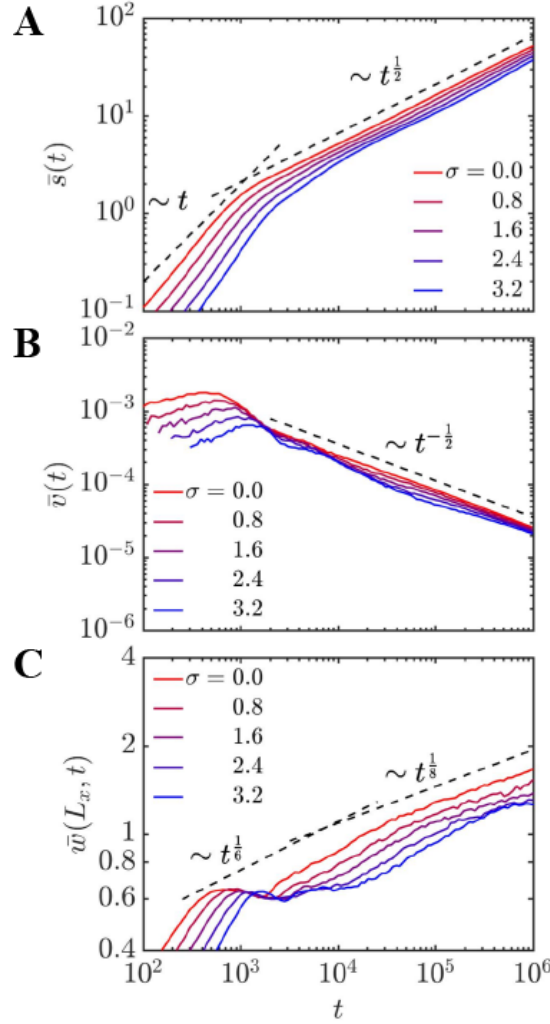


Figure 7: Log-log plot of growth of the (A) average interface displacement, (B) instantaneous interface velocity, and (C) interface roughness of the rising liquid layer with time, t , in KMC time unit. Solid lines are averages over 200 independent simulations with $A = 30$, $J = 3$, $g' = 0$, $\sigma = 0, 0.8, 1.6, 2.4$, and 3.2 , from red to blue, respectively. Dashed lines are the guide for the eye.

respectively. In particular, we observe the kinetic roughening of the interface (97; 82) in the transition from $t^{(1/6)}$ at intermediate times to $t^{(1/8)}$ at long times, as σ increases. However, to

verify whether or not interface roughness grows with $t^{(1/8)}$ at long time for large values of σ , KMC simulations need to be run for at least an order of magnitude longer than 10^6 KMC time unit performed in this work. We leave this verification to a future work.

Table II represents the mapping between dimensionless and dimensional surface tension used in Figure 7. For this mapping, we utilize above-mentioned lattice spacing and thermal energy (kT) and invoke the surface tension definition in Equation 2.5. We are hypothesizing that by using different liquids and substrate materials one could potentially tune the surface tension. We notice that the dimensional values for surface tension in Table II is rather small. To work with these dimensionless values for surface tension yet model larger dimensional surface tension, one would need to consider smaller lattice spacing. However, surface tension only slows the rise by affecting the interfacial particles upward hops. Therefore, increasing γ and consequently σ will only cause KMC simulations to spend a lot of time on moving bulk particles as opposed to interfacial particles, manifesting a shift along the time axis in the interface displacement, velocity, and roughness, as shown in Figure 7C.

TABLE II: THE MAPPING BETWEEN DIMENSIONLESS AND DIMENSIONAL SURFACE TENSION

σ	γ (mN/m)
0	0
0.8	1.65×10^{-5}
1.6	3.29×10^{-5}
3.2	6.58×10^{-5}

2.3.4 Structure factor

It is important to note that the interface roughness is also affected by the size of the simulation box, L_x , which is an upper bound for the size of the largest wave length that can be presented by our KMC simulations. To gain more information on the impact of the size of the simulation box (largest wave length) on the interface roughness, we look at the variation of structure factor of interface roughness with size of simulation box in the presence of gravity and surface tension. The structure factor of interface roughness is calculated from

$$S(k, t) = \langle \xi_k(t) \xi_{-k}(t) \rangle \quad (2.11)$$

where $\langle \dots \rangle$ stands for average over 200 independent KMC simulations, and $\xi_k(t)$ is the Fourier transform of the difference of interface displacement from the average, *i.e.*

$$\xi(x, t) = h(x, t) - \bar{s}(t). \quad (2.12)$$

The Fourier transform is written as

$$\xi_k(t) = \sum_{j=1}^n \xi(x_j, t) e^{-2\pi i(j-1)(k-1)/n}, \quad k = 1, \dots, n \quad (2.13)$$

in which $x_j = j\Delta x = j$, and $n = L_x/\Delta x = L_x$. In the absence of gravity and surface tension, the Fourier transform of interface roughness is expected to behave

$$S(k, t) \sim k^{-(2\alpha+1)} \quad (2.14)$$

at long times, where α is the roughness exponent. (97; 82) It can be shown that α is linked to the order of correlation of interface roughness with the largest wave length via

$$\bar{w}(L_x, t) \sim L_x^\alpha \quad (2.15)$$

at long times. (97; 82) We verified this behavior in $S(k, t)$ measured at 5 logarithmically spaced KMC times between $t = 10^3$ and 10^6 with $L_x = 512$ averaged over 200 independent KMC simulations, as shown in Figure 8A, indicating $\alpha \approx 0.50$, which is in reasonable agreement with the previous report. (82) Our results suggest that in the absence of gravity, as dimensionless surface tension increases from $\sigma = 0$ to 3.2, roughness exponent decreases from $\alpha = 0.5$ to 0.35, as shown in Figure 8B. We rationalize the dependence of interface roughness on the largest wave length as follows. Surface tension tends to flatten the interface, making large wave lengths energetically prohibitive to form. Formation of such long wave modes require concerted motion of points along the interface, rendering a rise in the interfacial energy. As such, impact of surface tension on the dampening of the largest wave mode becomes more pronounced. According to Equation 2.15, increasing the surface tension lowers interface roughness, and hence α . Similarity of Figure 8A and B reveals that the underlying dynamics of rising liquid

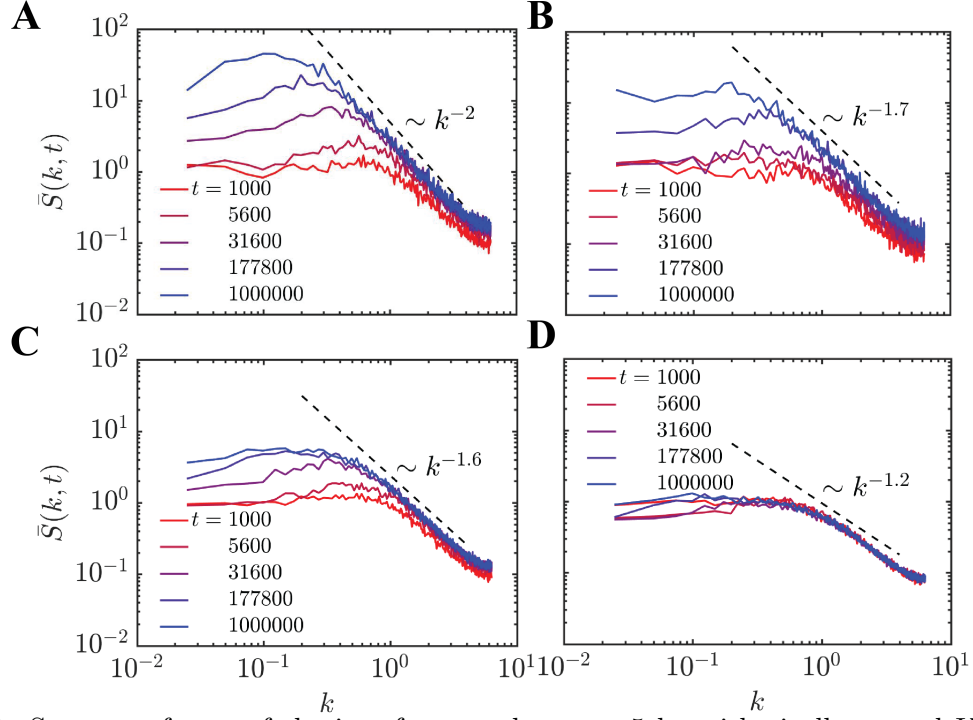


Figure 8: Structure factor of the interface roughness at 5 logarithmically spaced KMC time unit between $t = 10^3$, and 10^6 , from red to blue, respectively, averaged over 200 independent KMC simulations for (A) $g' = \sigma = 0$, (B) $g' = 0, \sigma = 3.2$, (C) $g' = 0.05, \sigma = 0$ and (D) $g' = 0.25, \sigma = 0$. Other parameters are $A = 30, J = 3, L_x = 512$, and $L_y = 300$. Dashed lines are the guide for the eye, illustrating k^{-2} , $k^{-1.7}$, $k^{-1.6}$ and $k^{-1.2}$ behavior in panels A, B, C and D respectively.

layer is only retarded once surface tension is applied at the interface. Hence, in the presence of surface tension, dynamics similar to that in the absence of surface tension will be observed yet at some longer time.

Likewise, in the absence of surface tension, we found that gravity has similar impact on the interface roughness. Figure 8C and D illustrates the decay of structure factor as time increases in the presence of gravity, $g' = 0.05$ and 0.25 , rendering the roughness exponent $\alpha \approx 0.35$

and 0.1 (see Supporting Information for $g' = 0.01$). Small α implies that interface roughness is nearly independent of the longest interfacial wave mode that can be formed theoretically during the rise of liquid layer, which indicates that interface roughness correlation in Equation 2.15 may no longer hold. The fact that structure factor for large enough gravitational acceleration at different KMC times almost overlap, as illustrated in Figure 8D, is also indicative of interface roughness being nearly independent of time as well as the longest wave mode, justifying the possible break down of interface roughness correlation mentioned above. Furthermore, smaller value of α extracted from Figure 8C and D compared to that from Figure 8B, suggests that the impact of gravity on dampening interface roughness is more evident than that of surface tension. We conjecture that is because gravitational force is a distributed force field, applied to every point in the bulk fluid; consequently, affecting every upward hop in KMC simulation. However, surface tension is a force applied to every point along the interface. Thus, concentrating only on the interface displacement, and so less effective.

2.4 Conclusions

We developed a 3D Ising lattice gas model to understand the impact of surface tension and gravity on the dynamics of a very thin liquid layer rising along a flat substrate. Utilizing our 3D lattice gas model in KMC simulations, we have shown that in the presence of surface tension alone, interface vertical displacement follows the \sqrt{t} universal law; however, the dynamics of liquid motion is retarded, leading to a delay in transition from ballistic to diffusive motion (t to \sqrt{t}) in interface displacement. We have demonstrated that in the presence of gravity, interface displacement deviates from \sqrt{t} universal law to the extent that at large value of

gravitational acceleration, the interface will cease to rise. While in the presence of surface tension, spatiotemporal fluctuations of interface roughness can be dynamically rescaled at long times, we found that in the presence of large gravitational acceleration, these fluctuations cannot dynamically be rescaled.

Overall, our work has allowed us to address how surface tension and gravity affect the interfacial dynamics. Here, we only considered single component fluid. However, additional work is warranted to show the interface as well as flow dynamics during rising (wetting) and falling (dewetting) of complex liquid films where nanoparticles are suspended. Understanding this dynamics will help unravel mechanisms of directed self-assembly of nanoparticles during dewetting of such complex liquid films.

CHAPTER 3

UNRAVELING THE MECHANISM OF A RISING THREE-PHASE CONTACT LINE ALONG A VERTICAL SURFACE USING MANY-BODY DISSIPATIVE PARTICLE DYNAMICS

Reprinted with permission from (Luo, Z. and Mehraeen, S.: Unraveling the mechanism of a rising three-phase contact line along a vertical surface using many-body dissipative particle dynamics. Langmuir, 36(26):7471-7482, 2020). Copyright (2020) American Chemical Society.

3.1 Introduction

Imbibition and spreading of liquid films on solid surfaces has taken a lot of attention in the past few decades, (61; 64; 65) and play a significant role in variety of industrial processes, particularly in printing, (10) coating (102) and oil recovery. (103) Recently, it was also shown that the spreading of a liquid film on patterned surfaces can be utilized to controllably position sub-10 nm particles into lithographically defined templates. (58; 60; 59) Harnessing the spread and controlling the properties of the thin liquid film for these applications require good understanding of underlying dynamics, particularly where the thickness of liquid film is less than few hundreds of nanometers. In-situ characterization of the spreading thin liquid films at such small length scales also has been a great challenge. As such, computational simulations have become an indispensable tool to investigate the spreading mechanisms of thin liquid films, and look at phenomena that are too small for in-situ imaging and characterization. (72; 73; 74; 75; 76)

These simulations have been utilized to study the spreading of a molecularly thin precursor film on flat surfaces, (66; 88; 67; 68; 104; 76) which has been shown experimentally by means of dynamic ellipsometry and x-ray reflectivity, (71; 77; 78; 79; 80) advancing faster than macroscopic solid-liquid-vapor contact line. 2D and 3D lattice MC simulations have been used to show a power law or \sqrt{t} behavior of spreading profile of droplets on horizontal (79; 105; 106; 107) and vertical (108; 109; 81; 83; 82) surfaces. While the MC simulations are appropriate to capture the dynamics at long time, they are unable to exhibit the flow field near the contact line, and illustrate the dynamics at short time. They are restricted to the underlying lattice structures and can only capture dynamics at irregular time points at a scale much larger than the lattice spacing. Assuming that the thickness of the precursor film follows a diffusion equation and using continuum theory, de Gennes has also shown that a diffusive profile for the contact line, creeping vertically on a standing wall, emerges. (67) Solid-on-solid model in conjunction with Langevin dynamics, and 1D diffusion equation have been utilized to describe growth of a thin film on horizontal surfaces, suggesting three different dynamics, $\sqrt{t \log(t)}$, \sqrt{t} , and power law behavior for the spread of the thin film. (110; 66; 104) 3D MD simulations of a droplet spreading on a horizontal surface suggest four different $\sqrt{\log(t)}$, \sqrt{t} , t , and power law (for liquid drop of chain-like molecules) variations of the droplet radius over a model time interval. (111; 112; 113; 114; 115; 116)

As it stands, existing literature collectively suggest that there is no off lattice computational model, looking at creeping liquid film on vertical surfaces. Furthermore, there is no theory without prior assumption of diffusive dynamics for the film thickness or the growth of the film

on vertical surfaces. As such, there is more work warranted to better understand dynamics of capillary liquid films on vertical surfaces and the impact of wall roughness on the rise of the liquid film.

Dissipative Particle Dynamics (DPD), (117; 118) as a coarse grained MD simulation, has been proposed to model complex fluids including the liquid-vapor contact line motion on surfaces, (119) and multiphase fluid flow in micro-channels. (120) However, due to repulsive nature of the conservative force in DPD, this method is not able to properly model spreading liquids with a liquid-vapor coexistence. To properly model this coexistence, Many-body Dissipative Particle Dynamics (MDPD) has been proposed. (121; 122; 123) Unlike DPD that only depends on the pairwise repulsive interaction in the conservative force, MDPD includes an attractive term to expand the conservative force. As such, MDPD is able to simulate the solid-liquid interfaces, (30) two-phase flows, (124; 125) capillary spreading of liquids, (126; 127) and liquid-vapor coexistence without simulating the vapor phase. (128; 122; 129)

In this chapter, we utilize MDPD to unravel the mechanism of spontaneous capillary rise of a very thin film against gravity on vertical flat and rough substrates. By systematically analyzing the spreading of the thin film, we also report on the displacement of the three-phase contact line, and illustrate the flow field in the close proximity of the liquid-vapor interface. We use LAMMPS package to perform the simulations.

3.2 Theoretical Model

3.2.1 MDPD model

We use MDPD model to simulate the capillary rise of a thin liquid film on a flat wall. In MDPD model, the fluid is simulated by a set of interacting particles characterized by their position \vec{r}_i , velocity \vec{v}_i and mass m_i , where i is the particle index.

In this model, interparticle forces are pairwise additive given by

$$\vec{F}_i = \sum_{i \neq j} \left(F_{ij}^C + F_{ij}^D + F_{ij}^R \right) \vec{e}_{ij}, \quad (3.1)$$

$$F_{ij}^C = A_{ij} w_c(r_{ij}) + B(\bar{\rho}_i + \bar{\rho}_j) w_d(r_{ij}), \quad (3.2)$$

$$F_{ij}^D = -\gamma w_D(r_{ij})(\vec{v}_{ij} \cdot \vec{e}_{ij}), \quad (3.3)$$

$$F_{ij}^R = \xi w_R(r_{ij}) \frac{\theta_{ij}}{\sqrt{\Delta t}}, \quad (3.4)$$

where \vec{F}_i is the resultant force acting on particle i , F_{ij}^C , F_{ij}^D , and F_{ij}^R are conservative (using Warren's approach), (130) dissipative, and random force acting on particle i due to interaction with particle j , respectively. $\vec{r}_{ij} = \vec{r}_i - \vec{r}_j$, $\vec{v}_{ij} = \vec{v}_i - \vec{v}_j$, $r_{ij} = |\vec{r}_{ij}|$, $\vec{e}_{ij} = \vec{r}_{ij}/r_{ij}$. In Equation 3.2, the weight functions are $w_c(r) = 1 - r/r_c$, and $w_d(r) = 1 - r/r_d$ which disappears at $r > r_c$ and $r > r_d$. Here, r_c and r_d is the attractive and repulsive force cutoff distance, respectively, where $r_d < r_c$. The instantaneously weighted average local density in Equation 3.2, $\bar{\rho}_i$, is defined by

$$\bar{\rho}_i = \sum_{i \neq j} w_\rho(r_{ij}), \quad w_\rho(r) = \frac{15}{2\pi r_d^3} \left(1 - \frac{r}{r_d} \right)^2, \quad (3.5)$$

where $w_\rho(r)$ vanishes for $r > r_d$ while satisfying $\int_0^{r_d} 4\pi r^2 w_\rho(r) dr = 1$. The weight functions in Equation 3.3 and Equation 3.4, are set by fluctuation-dissipation theorem,

$$w_D(r) = [w_R(r)]^2 = \left(1 - \frac{r}{r_c}\right)^2, \quad \xi^2 = 2\gamma k_B T, \quad (3.6)$$

where $k_B T$ is the Boltzmann constant, γ and ξ are the coefficients for dissipative and random force, respectively, and $w_D(r)$ and $w_R(r)$ vanish for $r > r_c$. (131) Δt and θ_{ij} in Equation 3.4 are the simulation time step and a Gaussian random variable with zero mean and unit variance, respectively. Utilizing r_c , m , and $k_B T$ as the dimensionalizing length, mass, and energy scale, respectively, without loss of generality, we assume $r_c = k_B T = m = 1$. For time integration of Newton's equations of motion with forces described in Equation 3.1, we use the velocity Verlet algorithm with the empirically introduced parameter of 0.5 to avoid energy drift and numerical errors. (132)

3.2.2 Parametrization

In the realm of MDPD model, to setup initial conditions at particle insertion stage, we use particle number density of $\rho = 6$. We choose complete wetting interaction between solid and liquid phase ($A_{ij} = -40$ between solid and liquid in Equation 3.2). To model the capillary rise of the liquid film on a flat standing substrate, we consider the liquid film subject to a driving force. The driving force, acting on the liquid film, is simulated by the degree of wettability assigned to the wall. To understand the impact of surface roughness on the rise of the thin liquid film, we consider three different surface structures, (i) flat surface, (ii) patterned surface with

square cavities, which are frequently used in directed self-assembly of nanoparticles, (60; 59) and (iii) rough surface, where solid-surface particles are randomly distributed. We do not allow liquid particles penetration into the flat wall-surface; however, due to substrate porosity of the rough wall-surface, particles penetration into the surface is unavoidable. Therefore, we will place a specular reflective boundary condition behind the rough wall-surface to prevent the liquid particles from penetrating indefinitely into the wall. We would like to emphasize that treatment of boundary conditions for hydrophilic flow is still an open area of research. (129) In the rigid-wall model, particles representing the wall are kept motionless, which causes slight density fluctuation at the solid-liquid interface. We will discuss the details of liquid particles distribution in the solid phase later in the results section.

In MDPD, it is more convenient to work with dimensionless model parameters, however, to keep our model instructive, we provide common dimensionless parameters used in our simulations in Table III with their corresponding dimensional values.

In Table III, we relate the dimensionless to dimensional parameters using (127)

$$r_c = \left(\frac{\rho}{\rho^*}\right) \left(\frac{\sigma}{\sigma^*}\right) \left(\frac{\eta^*}{\eta}\right)^2, \quad (3.7)$$

$$m = \left(\frac{\rho}{\rho^*}\right)^2 \left(\frac{\sigma}{\sigma^*}\right)^3 \left(\frac{\eta^*}{\eta}\right)^6, \quad (3.8)$$

$$\tau = \left(\frac{\rho}{\rho^*}\right) \left(\frac{\sigma}{\sigma^*}\right)^2 \left(\frac{\eta^*}{\eta}\right)^3, \quad (3.9)$$

TABLE III: MAPPING BETWEEN DIMENSIONLESS AND DIMENSIONAL MDPD PARAMETERS

Description	Symbol	MDPD units	Physical units
Particle mass	m	1	2.29×10^{-23} kg
Thermal energy	$k_B T$	1	4.11×10^{-21} J
Attractive force cutoff distance	r_c	1	5.93×10^{-9} m
Repulsive force cutoff distance	r_d	0.75	4.45×10^{-9} m
Fluid (hexane) density	ρ	6	660 kg/m ³
Surface tension	σ	7.51	0.0185 N/m
Dynamic viscosity	η	7.41	2.97×10^{-4} kg/ms
Liquid-liquid attraction parameter	A_{ll}	-40	-5.84×10^{-10} N
Solid-liquid attraction parameter	A_{sl}	-37.5	-5.48×10^{-10} N
Repulsion parameter	B	25	7.61×10^{-35} Nm ³
Viscous dissipation	γ	18	4.28×10^{-12} kg/s
Amplitude of random force	ξ	6	8.61×10^{-16} Ns ^{0.5}
Velocity Verlet parameter	λ	0.5	none
Time unit	τ	1	9.65×10^{-11} s
Time step	Δt	0.01	9.65×10^{-13} s

where the physical units of r_c , m , and τ are obtained from dimensional parameters labeled with an asterisk. In MDPD model, we nondimensionalize the length, mass, time, and energy by r_c , m , τ , and $k_B T$, respectively.

3.2.3 Static contact angle measurement

To extract the static contact angle from a set of particles configuration, first we locate the solid-liquid and liquid-vapor interfaces as follows. We discretize the entire three dimensional simulation box into voxels with side length of $0.25 r_c$. This particular length is to make sure that majority of voxels in the liquid phase encapsulate at least one dissipative particle. For every voxel, we define an indicator function, being 1 if there is at least 1 liquid particle, which represents the liquid phase, and no solid particle in the voxel, and 0 otherwise. Then, we adopt

a moving average using a fixed window length of three, and a Gaussian kernel to smoothen the value of indicator function within the liquid phase. The smooth value of the indicator function allows us to capture the solid-liquid and liquid-vapor interface with the indicator function isosurface value of 0.2. Figure 9 illustrates the two dimensional schematic of this method, capturing an interface, shown in red, which separates solid (gray particles) and vapor (blank area) from the liquid phase (cyan particles). It is noteworthy that we only focus on the solid-liquid and liquid-vapor continuous interfaces, using the above mentioned interface capturing technique.

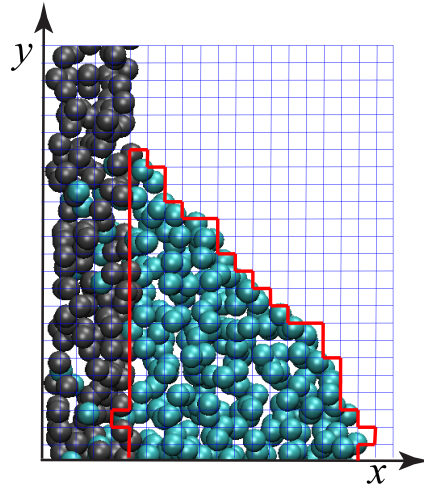


Figure 9: Two dimensional schematic of interface (red line) capturing technique, distinguishing solid (black particles) and liquid (cyan particles) from vapor (blank area) phase.

Using this technique, we characterize the wetting properties of the liquid thin film, spreading between two parallel plates, by extracting the static contact angle at the contact line, θ_s , for different values of solid-liquid attraction parameter, A_{sl} , as shown in Figure 10. We will demonstrate the relationship between static contact angle and solid-liquid attraction parameter. The system is set up with a $5 \times 25 \times 5$ simulation box, along the x -, y -, and z -direction, respectively, and periodic boundary conditions along the y - and z -direction, as shown in Figure 10 left panel. To represent the walls, we place solid particles in a two dimensional square lattice configuration in y - z plane at $x = 0$ and $x = 5$ as shown by gray particles in Figure 10. It is noteworthy that we use two dimensional particle arrangement to ensure a well defined frame of reference perpendicular to the wall to compute external work done by the wall particles on the liquid particles. For the two dimensional arrangement of wall particles, we utilize the lattice (as opposed to random) structure to avoid particles occasionally passing through the wall. This is particularly important when we calculate interfacial tension using Irving-Kirkwood model (133) as discussed below. Next, we randomly generate 750 particles, illustrated in cyan in Figure 10, to represent the liquid phase in the gap between the walls, initially located between $0 \leq x, z \leq 5$, and $10 \leq y \leq 15$. To find the correlation between static contact angle and solid-liquid attraction parameter, we vary A_{sl} and measure static contact angle accordingly. For each A_{sl} value, we run a simulation up to 10^5 time steps to form a well-defined contact angle at the solid-liquid interface.

Figure 10 depicts the formation of static contact angle for different values of A_{sl} from -40 to -10 with the interval of 10. Static contact angle is computed by finding the slope of the

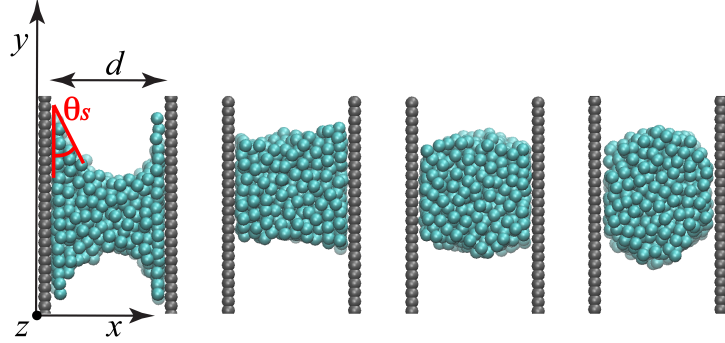


Figure 10: The equilibrium particles configuration for MDPD attraction parameter in increasing order, $A_{sl} = -40$ to -10 with the interval of 10, from left to right, respectively.

tangent to the initial part of the liquid-vapor interface formed at the three-phase contact line and the vertical line, as shown in the far left panel of Figure 10. We calculate static contact angle depicted in red in Figure 10, and average over 10 simulations.

To verify the results from contact angle measurements in Figure 10, we use Young's equation (92) given by

$$\cos(\theta_s) = \frac{\gamma_{sv} - \gamma_{sl}}{\gamma_{lv}} \quad (3.10)$$

where γ stands for the interfacial tension, and subindex s , v , and l represents solid, vacuum,

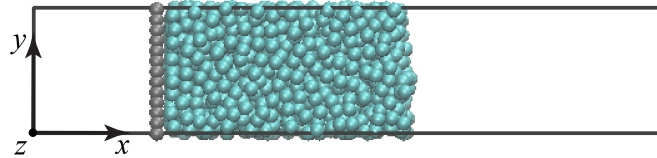


Figure 11: Configuration setup to compute γ_{sl} for various A_{sl} . Gray particles represent the solid phase, and cyan particles illustrate the liquid phase.

and liquid phase, respectively. To determine the interfacial tension, we pursue a separate set of simulations (119; 134) as depicted in Figure 11. These simulations are performed in a box of $25 \times 5 \times 5$ in x -, y -, and z -direction, respectively. We form a solid phase (wall) by freezing the particles in a two dimensional square lattice configuration in y - z plane positioned at $x = 5$. We set the number density of the solid phase particles (shown gray in Figure 11) to $\rho = 6$ per unit area, which is identical to volume density of particles in the liquid phase (shown cyan in Figure 11). For the configuration illustrated in Figure 11, we find that:

$$\gamma_{sl} = -\gamma_{lv} + \frac{1}{A_{yz}} \sum_{i < j}^N \left(F_{ij,x}^C r_{ij,x} - \frac{1}{2} \left[F_{ij,y}^C r_{ij,y} + F_{ij,z}^C r_{ij,z} \right] \right) + \frac{1}{A_{yz}} \sum_{i=1}^N \sum_{k=1}^M F_{ik,x}^C r_{ik,x}, \quad (3.11)$$

where the first term, $-\gamma_{lv}$, is to account for the interfacial tension at the liquid-vacuum interface on the right side of the simulation box, A_{yz} is the solid-liquid interfacial area parallel to the y - z plane, M and N are the total number of particles in the solid and liquid phase, respectively, and $F_{ij,\alpha}^C$ and $r_{ij,\alpha}$ indicate the conservative force and position vector along α direction, respectively. In Equation 3.11, the first summation is over every pair of particles in the liquid phase, indicating the stress tensor using Irving-Kirkwood model, (133) and the second summation represents the contribution of solid particles (*i.e.* external potential) to the stress tensor.

To find γ_{lv} in Equation 3.11, we perform simulations in the absence of the solid wall. In that case, γ_{sl} is replaced by γ_{lv} on the left side of the equation from which we determine γ_{lv} . Since the vacuum is not modeled by dissipative particles, there will be no contribution from γ_{sv} in Equation 3.10. Figure 12 compares the results from direct measurement of contact

angle (red) in MDPD simulations using interface tracking technique discussed above, and from Young's equation Equation 3.10 (blue). We observe a small deviation between the MDPD simulation results and those from the prior work by Henrich *et al.* (127) (shown black in Figure 12) for $A_{sl} \geq -15$. We attribute this difference to the two dimensional solid wall particles configuration, which is different from the three dimensional configuration implemented in the prior work.(127) Since the number density of particles per unit area in the solid wall in our model is equivalent to the volume density of solid particles in the prior work,(127) we anticipate larger interaction between the liquid and solid wall in our model, leading to static contact angle of 180° at smaller A_{sl} in absolute value. Overall, we find that the comparison in Figure 12 is in reasonable agreement with the previous studies, (129; 127) suggesting consistent results and chosen simulation parameters.

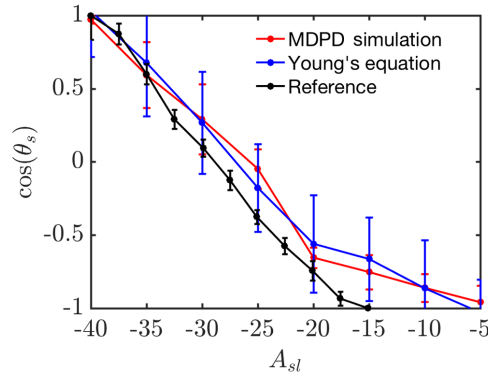


Figure 12: Comparison of cosine of the static contact angle, θ_s , as a function of A_{sl} , from MDPD model (red), Young's equation (blue) both averaged over 10 simulations, and the work by Henrich *et al.* (127) Error bars indicate the corresponding standard deviation.

3.3 Results and Discussion

In this section, we study spontaneous capillary rise of a liquid thin film against gravity in two separate systems, double- and single-wall configurations in which vertical walls are partially submerged into a liquid reservoir. In both systems, a liquid reservoir is placed below the solid substrate to provide liquid for capillary rise. Due to small MDPD size, hence mass (see Table III), gravitational force is a few orders of magnitude smaller than pair and hydrodynamic interactions. Thus, we ignore gravity in force calculations in the MDPD model. However, we allow for the evaporation. Any liquid particle that is separated from the liquid, will enter the vapor phase. If it reaches to the top of the simulation box, it will be removed from the simulation.

3.3.1 Spontaneous capillary rise of liquid film

3.3.1.1 Double-wall configuration

In double-wall geometry, we consider the capillary rise of a liquid film through the gap between two parallel standing walls. We define the simulation domain as $L_x = 6$, $L_y = 311$ and $L_z = 5$, in which liquid particles rise in y -direction with a periodic boundary condition in z -direction.

Figure 13, from left to right, illustrates the progression of the liquid film, rising through the gap between the walls. We generate each rough solid wall by randomly throwing 4500 particles into a box of $1 \times 150 \times 5$ in x -, y -, and z -direction, respectively. We model the liquid reservoir by randomly generating 16440 particles in a box of $6 \times 90 \times 5$ in x -, y -, and z -direction, respectively, positioned underneath the solid walls with 1 unit immersion depth, as shown in Figure 13. We

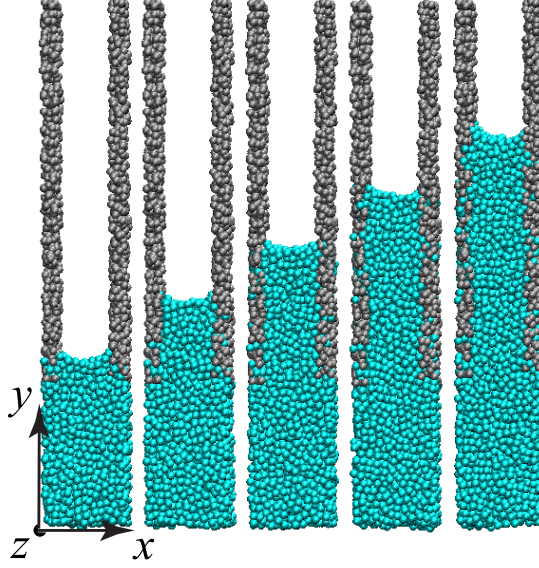


Figure 13: Front view at x - y plane taken from MDPD simulations illustrating the progression (from left to right) of spontaneous capillary rise of a thin liquid film in double-wall geometry.

set the gap between the walls to 4 units along x -direction. To have an uninterrupted stream of liquid entrained by the liquid film within the gap, we continuously insert particles into the reservoir from the bottom not to interfere with dynamics of particles at higher elevations within the gap between the walls. For reservoir, below the walls, we apply periodic boundary conditions in x - and z -direction, whereas for the liquid within the gap we use periodic boundary conditions along the z -direction only. As shown in Figure 13, far left panel, the initial meniscus at the liquid-vapor interface as well as dynamic contact angle are formed slightly above the entrance to the gap between the walls where the liquid film comes into contact with the reservoir. Using interface capturing technique discussed before, we measure the change in height of liquid film with respect to the height at initial condition along the gap center-line in x - y plane. Averaging

over independent simulations, we find the average height of capillary rise in time, $\bar{s}(t)$, which can be written as

$$\bar{s}(t) = \langle h(t) \rangle, \quad (3.12)$$

where $\langle . \rangle$ stands for averaging over 10 independent MDPD simulations, and $h(t)$ is the height of the liquid film at the center-line ($x = L_x/2$).

Figure 14 illustrates the evolution of average height at the center-line, $\bar{s}(t)$ against MDPD time in double-wall geometry. The results in Figure 14 exhibit an initial ballistic dynamics in which average height varies approximately linearly with time, $\bar{s}(t) \sim t$, followed by a transition to a diffusive dynamics regime during which $\bar{s}(t) \sim \sqrt{t}$.

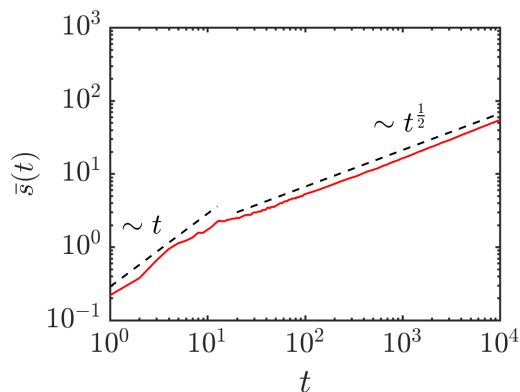


Figure 14: Evolution of height of liquid film in MDPD time unit (red), averaged over 10 simulations and measured at the center-line ($x = L_x/2$) during spontaneous capillary rise through the gap between two standing solid walls shown in Figure 13. Dashed lines are the guide for the eye.

3.3.1.2 Single-wall configuration

The computational tool that we have developed to illustrate the dynamics of capillary rise in double-wall geometry can also be utilized to unravel the underlying dynamics of spreading liquid films when only a single wall is present. Capillary rise in single-wall configuration is frequently used in dip coating process, and directed self-assembly of nanoparticles into lithographically defined templates. (58; 60; 59)

It is known from the capillary rise experiments, where a thin liquid layer creeps upward along a vertical substrate, that the height of the liquid layer increases proportional to \sqrt{t} (reminiscent of a diffusive motion) until the liquid layer stops growing due to the surface evaporation and gravity.(76) Unlike the double-wall configuration in which both walls restrict the lateral expansion of liquid layer, in single-wall configuration, gravity plays an important role in limiting the thickness of the liquid layer. Therefore, to account for the impact of gravity on limiting the liquid layer thickness, we apply an external repulsive lateral force once the particles move beyond a predefined thickness. Our simulations indicate that in the absence of the repulsive force and due to the liquid-vapor surface tension, liquid tends to form a droplet as soon as the liquid comes into contact with the vertical surface. We find that the size of the droplet increases over time as it pulls more liquid from the reservoir at the bottom. The liquid layer, climbing on the surface, cannot become very thick in which case the weight of the layer will be larger than the shear force provided by the surface-liquid interface. Therefore, gravity limits the thickness of the liquid layer on the surface. However, in MDPD model, the particle size and mass are so small such that gravity is not comparable to hydrodynamic and van der Waals

forces. Therefore, the gravitational force cannot be applied to the particles; instead, we apply a repulsive force if the liquid layer thickness becomes larger than a certain limit. This repulsive force is implemented by placing an array of fixed 'ghost' particles (with $A_{ij} = 0$ and $B = 25$ in Equation 3.2) across and parallel to the single wall on the other side of the liquid layer.

In single-wall configuration, we partially immerse a substrate with rough surface into a liquid reservoir. We model the single rough solid wall and the liquid reservoir as explained above in double-wall configuration. To mimic the impact of gravity on limiting the thickness of the rising liquid layer, we place randomly 4500 'ghost' particles in a box of $1 \times 150 \times 5$ in x -, y -, and z -direction, respectively, between $5 \leq x \leq 6$ in parallel to the solid wall. We apply periodic boundary conditions along x - and z -direction in the reservoir, and only z -direction in the liquid layer.

Figure 15, from left to right, illustrates the progression of capillary rise of a thin liquid layer on a single wall. The layer of ghost particles, not shown in Figure 15, on the right of the liquid layer clearly provide necessary repulsion to restrict the horizontal expansion of the liquid layer as shown at different time points of the evolution of the liquid layer in Figure 15. Limiting the thickness of liquid layer then leads to a well-defined and constant dynamic contact angle which will be discussed later in this section.

To verify the dynamics of the liquid film, we compute the height of liquid layer at the contact line from the initial configuration in x - y plane. We compute this height for three different solid wall surfaces, rough surface with surface roughness (standard deviation) of 0.13 along y - and z -direction, flat surface, and patterned surface with square cavities of size $1 \times 4 \times 4$ in x -, y -,

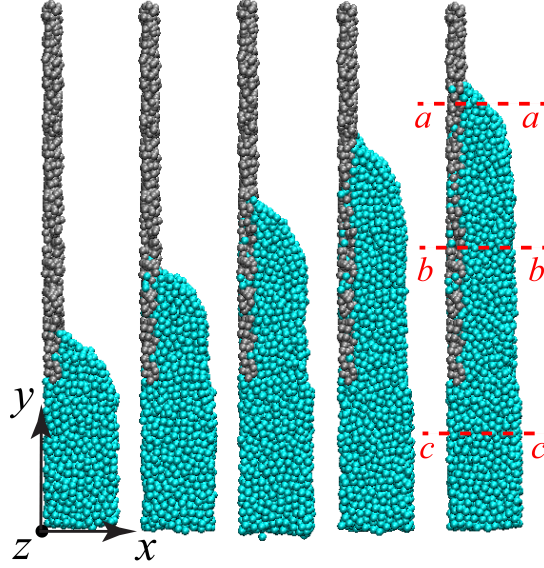


Figure 15: Side view of MDPD simulations, from left to right, illustrating the progression of spontaneous capillary rise of a liquid film along a standing single wall partially immersed into a liquid reservoir at the bottom.

and z -direction, respectively, with edge-to-edge distance of 4 between the cavities, as shown in Figure 16. By looking at the displacement of contact line on these surfaces, we will gain insight into the impact of surface roughness on the rise of the liquid thin film. Given that the elevation of contact line slightly varies along the z -direction, we use the maximum y -position along z -direction of the moving contact line averaged over 5 simulations, denoted by $\bar{s}(t)$.

Figure 17 depicts $\bar{s}(t)$ against MDPD time, t , in single-wall geometry with three different surface configurations as shown in Figure 16. Similar to the double-wall system discussed above, the results in Figure 17 also exhibits an initial ballistic motion, with contact line displacement varying linearly with t at short time, $\bar{s}(t) \sim t$, followed by diffusive dynamics, $\bar{s}(t) \sim \sqrt{t}$, at

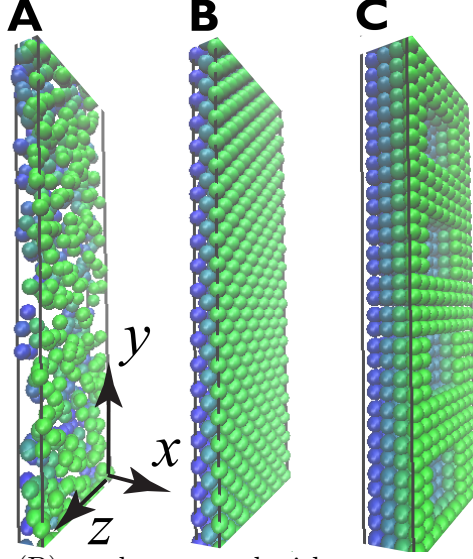


Figure 16: Rough (A), flat (B), and patterned-with-square-cavity (C) wall-surface structure (in y - z plane) along which displacement of the contact line is measured in time. Wall color varies with depth from green to blue corresponding to top to bottom surface. See text for characteristics of rough and patterned surfaces.

long time limit. Figure 17 also suggests that time-dependence of the contact line displacement is not impacted by the surface roughness and architecture. The fact that all three curves in Figure 17 exhibit a ballistic motion followed by a diffusive dynamics of the moving contact line confirms that the rising mechanism is independent of the surface roughness.

We also notice that the time at which $\bar{s}(t)$ transition from t to \sqrt{t} has increased in single-wall system in Figure 17 compared to that in double-wall system in Figure 14. We correlate this broadening of transition time from double-wall to single-wall system to the absence of the second wall in the latter. We explain this difference in transition time as follows. Underlying diffusive dynamics of capillary rise in both systems is driven by the vacancies generated at

the contact line, and diffusing from the contact line to the reservoir, as indicated in previous studies. (82) We speculate that the presence of the second wall leads to more vacancy creation at the contact line; hence, the system quickly reaches equilibrium between vacancy diffusion from top to bottom and liquid particles replacement from bottom to top. As such, single-wall system is slowly equilibrated with defect (vacancy) diffusion, and so the transition time to diffusive regime where $\bar{s}(t)$ asymptotes to \sqrt{t} is further delayed. Note that these simulations only model a short period of time in the real experiment. (76; 82) Overall, we find that our results are in reasonable agreement with previous experiments (76) and KMC models, (82; 135) illustrating capillary rise for geometries where gravitation was neglected.

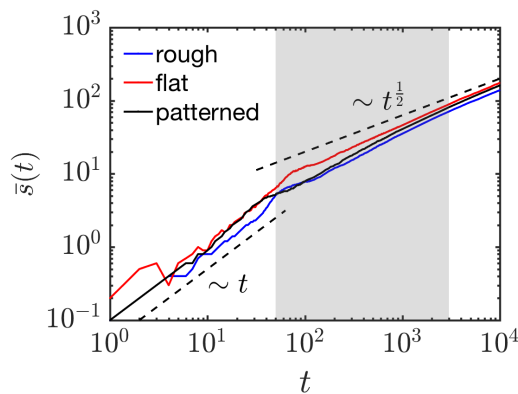


Figure 17: Log-log plot of evolution of the maximum interface displacement (averaged over 5 simulations) as a function of MDPD time during the rise of a liquid film along a rough (blue), flat (red), and patterned-with-square-cavities (black) single-wall surface, shown in Figure 16. Dashed lines are the guide for the eye. Shaded area locates the period during which dynamic contact angle decreases (see Figure 27 for details).

To better understand the effects of the rough wall on the dynamics of the liquid layer, we also look at the density variation across the layer. To illustrate density variation in x -direction across the liquid layer, we measure the particle densities at three different cross sections, marked by **aa**, **bb**, and **cc**, from top to bottom, respectively, in Figure 15 and Figure 18.

The density profile for solid phase in **aa** and **bb** plane, shown by red line in Figure 18, illustrates an approximately constant value at $\rho = 6$, which demonstrates the density for wall with which we started the simulation. We observe a liquid particles density of roughly $\rho = 6$ in the liquid phase at cross section **aa** and **bb**. We correlate the density fluctuation observed in section **aa** to the close proximity to the contact line, and the presence of high vacancy concentration. Also note the fast decay of liquid particles density between $4 \leq x \leq 5$, shown in section **aa** and **bb** in Figure 18, close to the repulsive ghost particles between $5 \leq x \leq 6$ (not shown in Figure 18). Minor liquid particle penetration into the solid phase between $0 \leq x \leq 1$, shown in section **aa** and **bb**, is mitigated by the presence of reflective boundary condition implemented at the far left where $x = 0$. Furthermore, the constant density of $\rho = 6$ in the liquid phase in cross section **cc** indicates the stability of continuous particle motion from the bottom of reservoir as the liquid layer moves up.

Note that in hydrophilic flows, particles penetration into the wall can be reduced by increasing the repulsion between the wall and liquid particles. This solution is not satisfactory, and leads to a fuzzy solid-liquid interface as suggested by other studies. (129) Extra force can also be applied to penetrated particles to push back, which disrupts the solid-liquid interaction, and alters the wetting behavior. (136) Treatment of the boundary conditions for hydrophilic flows

is still an open area of research. Further studies are needed at the molecular level, which is not attempted here.

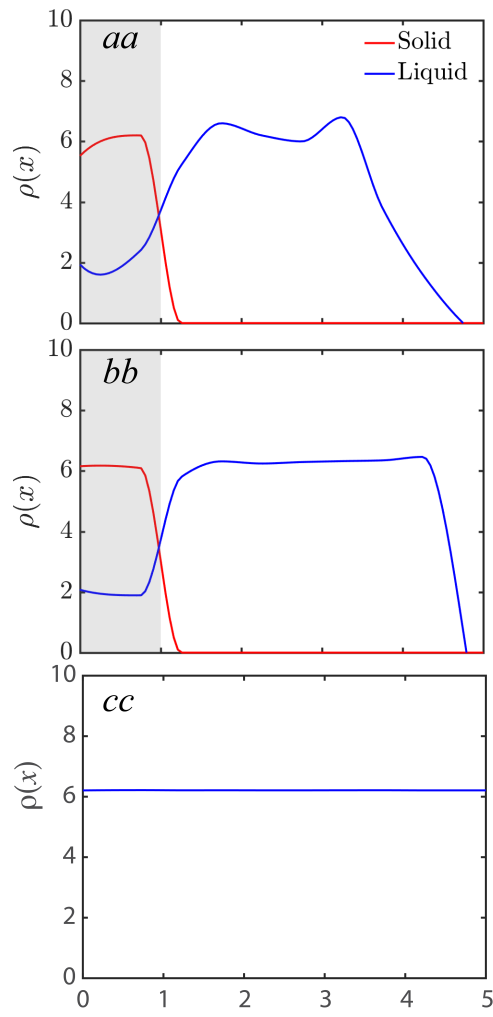


Figure 18: Particle density profile in the solid (red) and liquid (blue) phase at three cross sections *aa*, *bb* and *cc*, shown in the right panel in Figure 15. Shaded area in cross section *aa* and *bb* highlights the solid wall location.

3.3.2 Dynamic contact angle

Using MDPD model discussed before, we now look at the progression of advancing contact angle and its variation during capillary rise of the liquid film. To calculate the dynamic contact angle, θ_d , we locate the liquid-vapor and solid-liquid interfaces in single-wall system using interface tracking technique discussed above.

As shown in Figure 27A, θ_d is the angle between the linear fit to the liquid-vapor interface and the vertical line (solid-liquid interface). Starting from the configuration in which the position of initial meniscus is well defined, we present the variation of θ_d with MDPD time averaged over 5 simulations (blue line) in Figure 27B. Red line in Figure 27B indicates the moving average of θ_d , with window size of 7 and the Gaussian kernel. Results in Figure 27B suggest that θ_d is initially increasing with time right after meniscus is formed, and liquid layer starts rising. After approximately $t \approx 50$, θ_d starts decreasing up to approximately $t \approx 3000$ after which θ_d fluctuates about a stable angle. Considering the maximum displacement of meniscus, $\bar{s}(t)$, we find a correlation between θ_d and $\bar{s}(t)$. Results in Figure 27B indicates that θ_d is increasing when $\bar{s}(t) \sim t$ ($\bar{s}(t)$ is proportional to t). The period during which θ_d decreases, shaded in Figure 27B, nearly coincides with the transition from a fast ($\bar{s}(t) \sim t$) to a slow ($\bar{s}(t) \sim \sqrt{t}$) moving meniscus shown in Figure 17. Our results suggest two marked transitions, the first being approximately at $t \approx 50$ when $\bar{s}(t)$ begins to transition from t to \sqrt{t} , and second being approximately at $t \approx 3000$ at which $\bar{s}(t)$ fully transitions to \sqrt{t} . We shaded the time between these two transitions in θ_d , as illustrated in Figure 27B. θ_d stays approximately constant after $\bar{s}(t)$ fully transition to a diffusive regime ($\bar{s}(t) \sim \sqrt{t}$).

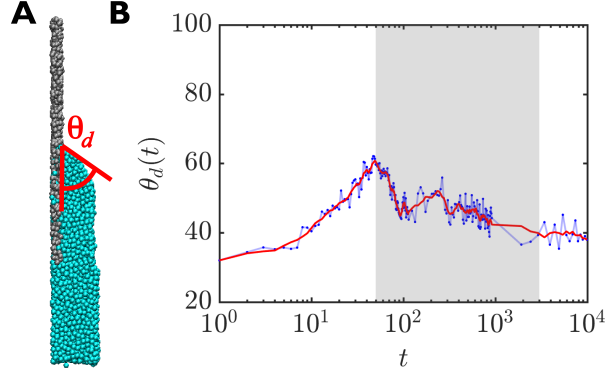


Figure 19: (A) Extracting dynamic contact angle between the fitted tangent to the interface and a vertical line (angle between two red lines) using interface tracking technique. (B) The variation of dynamic contact angle (blue) and moving average of dynamic contact angle (red) vs. MDPD time. Shaded area locates the range where the dynamic contact angle decreases.

3.3.3 Velocity and vorticity profile

MDPD model enables us to reveal the velocity profile in the thin liquid layer as it rises. To illustrate the velocity profile, we use linearly varying radial basis functions (RBF) to interpolate particles instantaneous velocity at uniform grid points with 0.5 unit spacing along x-, y-, and z-direction. At every point on the grid, the velocity will be equal to the weighted sum of instantaneous velocities of particles, which are within the RBF cutoff distance (unit length) from the grid point. Contribution of the particle velocity at a grid point decreases proportional to the Euclidian distance between the particle position and the grid point. Using the above mentioned interpolated velocities at the grid points, we illustrate the velocity field during the rise at time $t = 7900$ in MDPD time units with black arrows in x-y, z-y, and x-z plane, averaged over 8 simulations, shown in Figure 20A to C, respectively. We use the velocity field in Figure 20 to determine the distribution of vortices, which prevents a direct convection from

the reservoir at the bottom to the top of the rising film. Presence of these vortices suggests a series of circulations and an unsteady flow in the thin film as it rises along the wall. To confirm the unsteady flow field, we look at vorticity field, $\vec{\omega}$.

We compute the z-, x-, and y-component of $\vec{\omega}$ from

$$\omega_z = \frac{\partial v_y}{\partial x} - \frac{\partial v_x}{\partial y}, \quad \omega_x = \frac{\partial v_z}{\partial y} - \frac{\partial v_y}{\partial z}, \quad \omega_y = \frac{\partial v_x}{\partial z} - \frac{\partial v_z}{\partial x}, \quad (3.13)$$

where v_x , v_y , and v_z are the velocity components in x-, y-, and z-direction, respectively, at the grid points. Figure 20A to C illustrate variation of ω_z in x-y plane at $z = L_z/2 = 2.5$, ω_x in z-y plane at $x = 3$, and ω_y in x-z plane at $y = 40$, respectively, color coded with blue to red, from negative to positive vorticity, respectively.

Presence of distribution of vortices and irregular velocity field as depicted in Figure 20 suggests that the transport of a vacancy defect from the top of the liquid layer to the bottom towards the reservoir is performed similar to a random walk. This random walk pattern of defect diffusion is also consistent with prior studies using lattice kinetic Monte Carlo simulations. (81; 83; 108; 82; 59) Brownian motion of vacancy defects also leads to a diffusive motion of the contact line, giving rise to its displacement proportional to $\sim \sqrt{t}$, which confirms our finding using MDPD model shown in Figure 17.

Understanding the flow field in thin films with suspended nanoparticles, and that how they are transported from reservoir to the substrate will help control their directed self-assembly. Although suspended nanoparticles have not been considered here, we can potentially use this

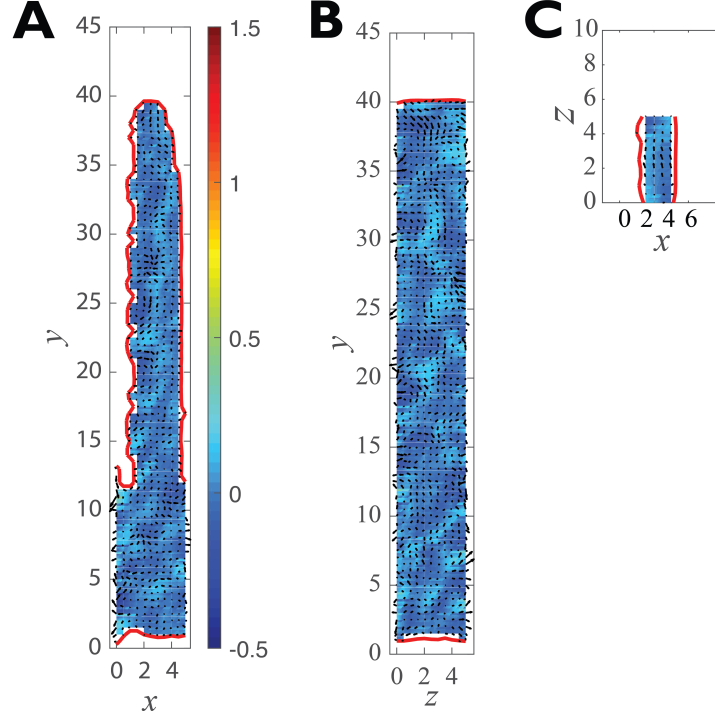


Figure 20: Velocity (black arrows) and vorticity (colormap) field in (A) x-y plane at $z = L_z/2 = 2.5$, (B) z-y plane at $x = 3$, and (C) x-z plane at $y = 40$, during capillary rise of the liquid thin film along a single wall positioned between $0 \leq x \leq 1$ (not pictured), averaged over 8 simulations. Red line indicates solid-liquid and liquid-vapor interface. Absence of an interface indicates positions where the periodic boundary condition is applied.

computational tool to visualize, and will be able to probe nanoparticles dynamics and reorganization in directed self-assembly particularly prior to deposition on to templated substrates, which will be studied elsewhere.

3.4 Conclusions

In the present work, we utilize the MDPD method to probe the mechanism of spontaneous capillary rise of a liquid thin film along a double and single flat wall. Adjusting the interaction

parameters between liquid and the wall allows us to manipulate wettability of the liquid and tune solid-liquid interfacial properties. With this computational platform, we have shown that the contact line displacement during capillary rise in double- and single-wall systems exhibits two regimes, a ballistic motion followed by a diffusive dynamics of the three-phase contact line. Our results suggest that the dynamics of advancing contact line in both regimes is independent of the surface roughness. From averaged velocity field, we found that the transport from reservoir at the bottom to the rising contact line at the top, involves with an unsteady flow. Averaged vorticity field also confirmed a distribution of clockwise and counter clockwise local circulations, dictating a random walk pathway if a particle rising from the reservoir is traced. Likewise, for a vacancy defect entering at the moving contact line from the top and moving towards the bottom, we find a random walk motion traversing through the cascade of local vortices.

Here, we only considered the capillary rise (wetting) of the liquid film. Additional work is warranted to show the flow and interface dynamics during falling (dewetting) of liquid films, and in particular complex fluids where nanoparticles are suspended in the liquid phase. Ultimately, understanding the complex fluid dynamics during dewetting will reveal mechanisms of directed self-assembly of nanoparticles, particularly on patterned substrates.

CHAPTER 4

A MOLECULAR VIEW OF THE DISTORTION AND PINNING FORCE OF A RECEDING CONTACT LINE: IMPACT OF THE NANOCAVITY GEOMETRY

4.1 Introduction

The spreading of a liquid film on a templated substrate is commonly used in various applications including coating, printing, and cleaning, (10; 102; 103) as well as DSA-n into lithographically defined templates. (58; 60; 59) Many studies have been conducted to understand, both theoretically and experimentally, the underlying mechanisms of liquid film spreading on rough surfaces. (65; 137; 138; 139) These studies have holistically focused on two aspects of the film spreading: the contact angle hysteresis, and contact line pinning.

The contact angle between solid-liquid and liquid-vapor interfaces is commonly used to characterize the ability of wetting a substrate. On a smooth substrate, the contact angle is determined by the interfacial tensions according to Young's equation, (92) while on a rough substrate, e.g. pillars, grooves, and the like, the surface roughness comes into play and largely impact the wetting behavior. Two models are extensively used to interpret the relation between surface architecture and wetting behavior of liquid droplet on substrates: Wenzel and Cassie Baxter model. (140; 141; 142; 143) There are still active areas of research to investigate which model is appropriate to understand wetting behavior on rough surfaces using contact

angle calculations, and wetting conditions for the surface structure. In particular, there is still a debate to the extent that whether the wetting behavior is contact line or contact area dependent. (144; 145; 146; 147) Nevertheless, existing theories suggest that the complexity of the substrate geometry and composition plays a significant role in the contact angle variation, wetting dynamics, and contact line pinning of rough surfaces.

Studies have shown that wetting and contact line pinning of complex substrates is caused by either surface roughness or heterogeneity. (148; 149; 150; 151) Particularly, it has been reported that the wetting behavior of a droplet passing through a capillary pore is dependent on the wedge angle of pore entrance, (148) and that surface roughness affects wetting and dewetting of droplets. (152; 153; 154) In addition, several studies have considered a droplet sliding over hydrophobic surfaces, (19; 155) all of which imply that the wetting pattern and shape of droplet can be rectified by changing the property or shape of heterogeneity, (150; 151) such as hydrophobic and hydrophilic stripes, (156; 157) and chemical chessboard patterns. (19)

To understand the mechanism of liquid spreading and pinning on rough and patterned substrates, computational simulations of different conditions at microscopic scales have also been used. These simulations have provided insight into various measurements including local capillary, (148; 56) interaction forces between solid surface and liquid, (33; 158) both of which are generally difficult to measure experimentally. In particular, to study the influence of solvent molecular structure on the droplet spreading dynamics on flat surfaces, MD simulations have been used. (84; 86; 40) Spreading dynamics of thin films rising on flat (72; 82) and rough (159) walls has also been investigated using MC simulations.

All of aforementioned works have focused on the pinning and spreading dynamics of liquid droplets on various surfaces. Joanny and Nadkarni *et al.*, however, showed theoretically(160; 63) and experimentally(161) the pinning force exerted by a circular geometrical surface inhomogeneities on a liquid film (in contrast to droplets). Nevertheless, to our knowledge, spreading dynamics of liquid films around geometrical inhomogeneities other than circular objects, and their pinning forces exerted on the liquid film much larger than droplets is still lacking. Furthermore, the flow field at the contact line of the liquid film, and in the vicinity of the geometrical inhomogeneities has been overlooked. Such knowledge will aid in developing strategies to control directed self-assembly of nanoparticles into nanocavities, and patterned surfaces.

In the present chapter, we utilize MDPD simulations(121; 122; 130) in LAMMPS package to understand the mechanisms of pinning of a receding liquid film passing over a flat surface with a noncircular nanocavity in three dimensions, and measure the associated pinning force exerted by the nanocavity on the contact line. MDPD has been introduced as an extension of DPD,(117; 118; 131; 162; 132) which is a coarse-grained MD simulation, and allows one to model hydrodynamics of fluids while maintaining necessary structural properties of the components of the system. MDPD exhibits the capacity to simulate the liquid-vapor interface without simulating the vapor phase while accounting for evaporation at the liquid-vapor interface.(163; 164; 26; 19; 148)

In the evolution of pinning process, we focus on the progression of a receding contact line, measurement of its distortion, pinning force, internal flow field near the contact line, and variation of receding contact angle. We utilize a machine learning technique to capture solid-

fluid and fluid-vapor interfaces from the results generated by the MDPD model. The shape of liquid-vapor interface is used to calculate the pinning force exerted on the receding contact line. We compare the measured pinning force for the liquid film receding over a circular, elliptical, square, and triangular nanocavities. We will also quantify the contact line distortion, and contact angle variation. Our approach discussed in this work can be readily extended to look at the distortion of the receding contact line moving over multiple nanocavities of various shapes, and measure the pinning force applied to the contact line by the nanocavities.

4.2 Theoretical Model

4.2.1 MDPD model

We utilize MDPD model, as described in chapter 3.2, to understand the kinetics and dynamics of contact line receding over a nanocavity.

4.2.2 Simulation setup

In this section, we present results from simulations, which are carried out in 3 dimensions. We build the substrate using 35680 uniformly distributed solid particles with their positions fixed throughout the entire simulation. We excavate a nanocavity with various geometries in cross section from the substrate. We cover the substrate by a thin liquid film in the form of a box, composed of 10735 particles, representing the liquid phase. We construct a layer of frozen solid particles, perpendicular to the substrate, mimicking a piston. We then fill the nanocavity with the liquid particles, and construct the liquid film as mentioned above. In the simulation, we first equilibrate the liquid particles to form the liquid-vapor interface. Then, we move the

piston downward along the substrate with a constant speed. Moving the piston down will make the liquid film slide over the substrate; hence the nanocavity.

To account for the interaction of the liquid film and solid substrate, we allow the liquid particles to partially penetrate into the solid substrate to feel the force from the substrate. We place a bounce-back reflection boundary on the other side of the substrate to prevent the indefinite penetration of the liquid particles. We apply periodic boundary conditions parallel to the substrate, and perpendicular to the direction of the piston.

We summarize all parameters (otherwise refer to Table III) used in the simulations in Table IV, where the attraction coefficients are indicated by liquid-liquid attraction, A_{ll} , substrate-liquid attraction, A_{sl} , and piston-liquid attraction, A_{pl} . In our simulations, we non-dimensionalized the parameters in Table IV with respect to the characteristic mass, length, energy and time.

TABLE IV: MAPPING BETWEEN DIMENSIONLESS AND DIMENSIONAL MDPD PARAMETERS

Description	Symbol	MDPD units	Physical units
Liquid-liquid attraction parameter	A_{ll}	-40	-5.84×10^{-10} N
Solid-liquid attraction parameter	A_{sl}	-30	-4.38×10^{-10} N
Piston-liquid attraction parameter	A_{pl}	-20	-2.92×10^{-10} N
Piston velocity	v_p	0.005	0.369 m/s

4.2.3 Machine learning classification

To capture the vapor-liquid smooth interface, which is made of collection of discrete particles in MDPD simulations, we utilize a machine-learning algorithm (Support Vector Machine (SVM) with radial basis functions), (165; 166; 167) and predict a continuous contact line as it traverses over the substrate surface patterned with the nanocavity.

4.3 Results and Discussion

4.3.1 Progression of receding liquid film

In this work, we utilize MDPD simulations to understand the dewetting behavior of a liquid film, in contrast to a liquid droplet, passing over a nanocavity of various shapes. The simulation box size is set to be 16, 45 and 25 in MDPD units (see Table IV for unit conversion) along x -, y - and z -dimension, respectively. Dewetting is mostly driven by the gravity, which pulls the liquid film downward. In MDPD simulations, however, the size of coarse grained liquid particles (cyan in Figure 21) are so small that renders almost negligible gravitational force compared to other forces such as van der Waals and hydrodynamic forces. Therefore, to account for gravitational forces in MDPD simulations of the dewetting contact line, we put a piston (red in Figure 21) with a hydrophilic surface at the bottom of the liquid film. In the simulations, we move the piston downward with a constant speed of 0.005 in MDPD units (see Table IV).

MDPD simulation results indicate several stages as the contact line moves over the nanocavity, all in MDPD units (see Table IV), as shown in Figure 21A to Figure 21E. In these simulations, we color coded the liquid, substrate, and piston by cyan, gray, and red particles, respectively. As the piston goes down, the liquid film slides over the flat substrate, before reaching the

nanocavity. At this time, the contact line is stabilized, and the contact angle is formed, as illustrated in Figure 21A. The contact line is deformed once it reaches the nanocavity. We attribute this deformation to the liquid-liquid attraction, which is higher than solid-liquid attraction. A liquid parcel is trapped in the nanocavity, which attracts more liquid from the bulk of the moving film on the top. This leads to a slow motion of liquid particles right above the nanocavity, compared to liquid particles elsewhere, as shown in Figure 21B. The contact line then slides along the edge more slowly than far away from the nanocavity, which leads to a bent liquid-vapor interface as the contact line reaches the periphery of the nanocavity. Although we do not directly model the vapor phase, it is accounted for in MDPD simulations.^(163; 164; 26; 19; 148) Furthermore, liquid particles are allowed to cross the liquid-vapor interface from liquid to vapor phase. In this work, we observed the evaporation from liquid-vapor interface, and removed any evaporated particle when it reached to the top of the simulation box in the y -direction. Despite the fact that the contact line is highly bent around the nanocavity, the contact line is relatively unaffected at the far ends, shown in the dewetting progression in Figure 21C and Figure 21D.

Our simulation results suggest that the contact line pinning is merely a consequence of attraction from the liquid particles trapped in the nanocavity, which is left behind after the contact line is completely detached from the periphery of the nanocavity in Figure 21E. Upon depinning, once the contact line is completely detached from the nanocavity, almost straight contact line is resumed and stabilized, as shown in Figure 21E.

We superposed the snapshots shown in Figure 21, in the top view in Figure 22A. We then apply an interface capturing technique, which is based on a machine learning algorithm (support

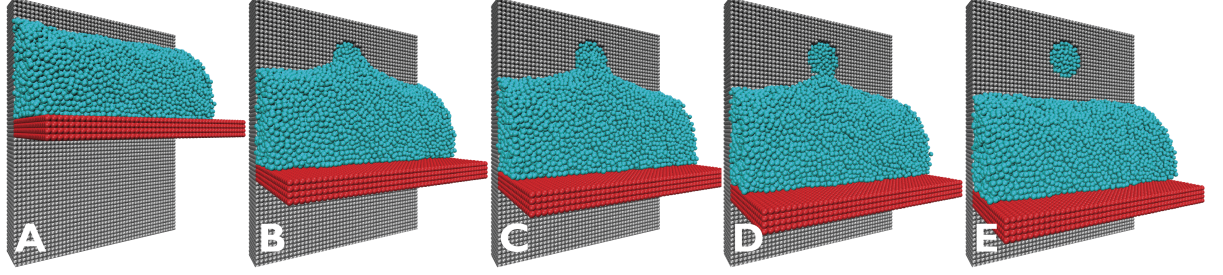


Figure 21: (A-E) Progression of dewetting of a liquid film (cyan) sliding over a solid substrate (gray) with a circular nanocavity. Dewetting is driven by a hydrophilic piston (red) moving down while in contact with the liquid film.

vector machine). (165; 166; 167) In using the machine learning algorithm, we assume the liquid-vapor interface to be the decision boundary. Using the particle representation of liquid film, the machine learning algorithm develops continuous vapor-liquid interfaces as the contact line recedes from top to bottom, light to dark blue, respectively, as illustrated in Figure 22A. The small fluctuations along the contact line, far away from the nanocavity, is driven by the thermal fluctuations in the underlying particle representation of fluid phase.

4.3.2 Distortion

In order to measure the pinning force exerted by the nanocavity to the liquid film, we define the distortion by the distance in the y -direction, between the attachment point of contact line to the periphery of the nanocavity, and far end of the horizon, nondimensionalized by the pair-potential cutoff distance, r_c , as shown in Figure 22B.

With the aforementioned definition of distortion, we compare the impact of nanocavity shape on the distortion of the contact line while keeping the cross-sectional area of the nanocavity

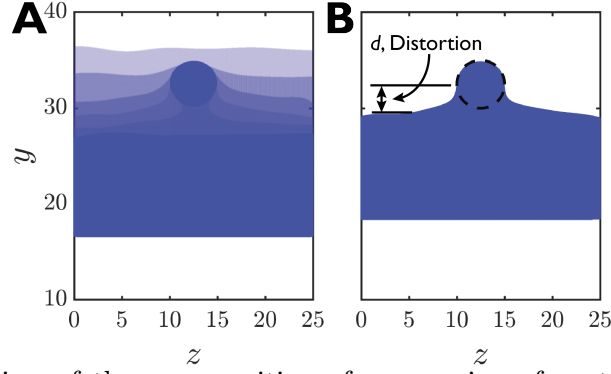


Figure 22: (A) Top view of the superposition of progression of contact line pinning as it is receding over a circular nanocavity, from top to bottom, light to dark blue, respectively. (B) The schematic of distortion definition.

fixed. The progression of pinning of a contact line as it goes over a circular nanocavity is illustrated in Figure 23A-D top row at different times (in MDPD time units), $t = 0, 8 \times 10^4, 1.5 \times 10^5$, and 1.6×10^5 , respectively. Likewise, Figure 23A-D bottom row shows the progression of the contact line receding over a horizontally oriented elliptical nanocavity. In these figures, the black dashed line shows the top view of the position of circular (top panels) and horizontally oriented elliptical (bottom panels) nanocavity. To calculate the distortion, we captured the liquid-vapor interface using Support Vector machine learning algorithm.⁽¹⁶⁸⁾ In aforementioned simulations, the circular nanocavity has the radius of 2.5 and depth of 2, and the horizontally oriented elliptical nanocavity has the major and minor axis of 7.06 and 3.54. The major and minor axes of the elliptical nanocavity were chosen in such a way to keep the cross section area of the nanocavity in xy -plane identical to that of the circular nanocavity. We also set identical depth for both nanocavities. We note that contact line pinning and distortion depends

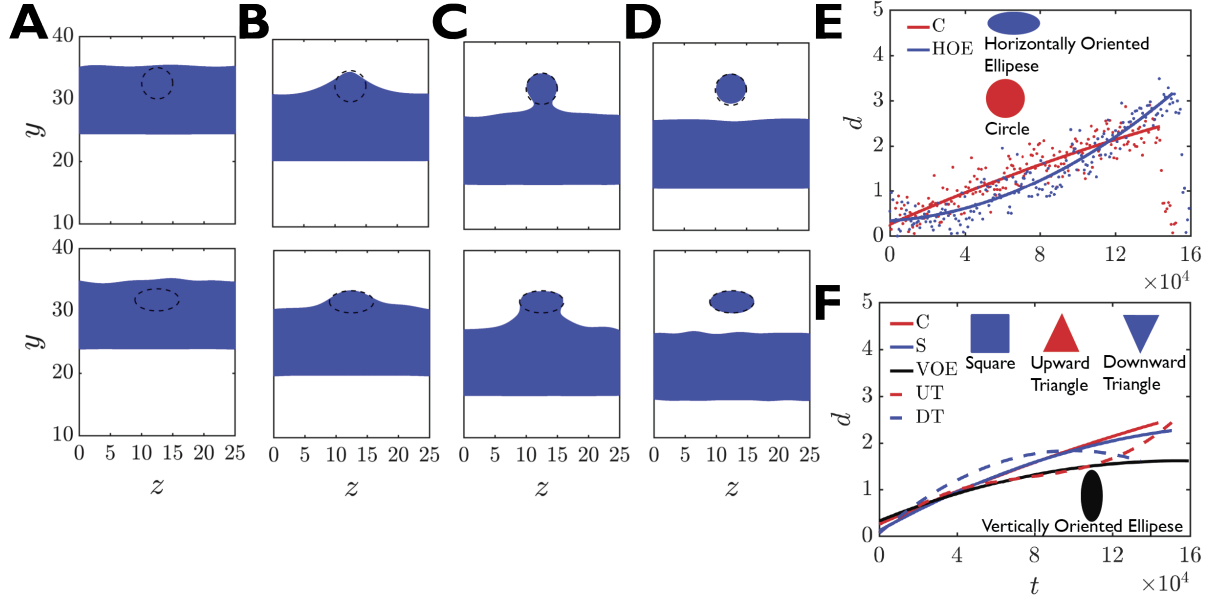


Figure 23: (A-D) Progression of contact line pinning for circular (top) and horizontally oriented elliptical (bottom) nanocavities. (E) The variation of contact line distortion with time (in MDPD units) for circular (C, red) and horizontally oriented elliptical (HOE, blue) nanocavities. Lines are the best fit to the instantaneous distortion (dots). (F) Variation of contact line distortion with time for square (S), vertically oriented elliptical (VOE), upward triangular (UT), and downward triangular (DT) nanocavities. Contact line distortion with time for circular nanocavity was also included for reference.

on the wedge angle, which has been reported for nanovalves. (148) In this work, we restrict the simulations to a set of nanocavities with 90° wedge angle, i.e. walls of the nanocavities are perpendicular to their base. In these simulations, the liquid film thickness far from the nanocavity was 15.

The variation of corresponding distortion (d) calculated at equally spaced time intervals, from $t = 0$ up to the depinning time (in MDPD time units) as the contact line slides over the nanocavity is depicted in Figure 23E. Here, we set $t = 0$ at the beginning of pinning, when the

contact line is still flat. Red and blue dots indicate the instantaneous distortion measured from MDPD simulations for circular and horizontally oriented elliptical nanocavity, respectively, and the lines are the respective polynomial fit.

Our simulation results in Figure 23E suggest that curvature of the boundary of the nanocavity has a large impact on the distortion. In particular, boundary points with high curvature rapidly increase the distortion during contact line receding. Figure 23E shows that horizontally oriented ellipse (blue line) with two high curvature points across the major axis, initially has a distortion less than that of a circular nanocavity (red line). Before reaching to these points, contact line slides over low curvature part of the boundary in horizontally oriented elliptical nanocavity. As such the distortion is initially low. Once the contact line goes past the major axis, distortion rapidly rises and goes past that of circular nanocavity.

Figure 23F compares the distortion, obtained from fitting to the MDPD simulations results (not shown for clarity), for a few other nanocavity geometries with the same cross-section area and depth as those of the circular nanocavity, including square (solid blue) with side length of 4.43, vertically oriented ellipse (solid black) with the major and minor axes of 7.06 and 3.54, respectively, upward (dashed red) and downward (dashed blue) equilateral triangle with side length of 6.73. As a reference, we also include the distortion for circular nanocavity (solid red) of the same cross-section area and depth in Figure 23F.

According to Figure 23F, vertically oriented ellipse shows the smallest distortion as it has only two points with high curvature on its boundary, one on the top and the other at the bottom. However, the curvature of these two points on the major axis of ellipse is less than

that of the corners on the boundary of a triangle and square. Upward triangle with three high curvature points seems to be the one with second lowest distortion. However, initially only the top vertex contributes to the rise of distortion as the contact line recedes from top to bottom. Once the contact line reaches the two vertices at the bottom, the distortion rises rapidly and becomes identical to that of square with two vertices at the bottom. In downward triangle however, the top two vertices initially contribute to the distortion. As a result, it shows the highest initial distortion among all. Nevertheless, as the contact line gets closer to the third vertex with high curvature at the bottom, distortion reduces. Before the contact line depins, the distortion becomes as low as that in vertically oriented ellipse with one high curvature point at the bottom. Square nanocavity with four high curvature vertices on the other hand, causes a distortion similar to that of circle with constant curvature around the boundary. The results suggest that this similarity in distortion can be due to similar overall curvature in circle and square, considering that flat edges in square have zero curvature.

Comparing Figure 23E and F reveals that at depinning, horizontally oriented ellipse and upward triangle generate the highest distortion among five geometries studied in this work. We conjecture that in addition to the presence of high curvature points on the boundary, the large distance between the two high curvature points across the major axis in horizontally oriented ellipse, and large bottom side length in upward triangle also contributes to the largest distortion at depinning as shown in the Figure 23A-D (bottom).

4.3.3 Pinning force

We utilize the distortion calculated above for each geometry to measure the corresponding pinning force. We calculate the pinning force acting on the receding contact line, which is pinned by the nanocavity, from (160; 161; 169)

$$\bar{f}_p = \frac{f_p}{\pi\sigma\theta_0^2}, \quad f_p = \int_l \sigma (\cos \theta_l - \cos \theta_0) dl \quad (4.1)$$

where \bar{f}_p is the pinning force, f_p , nondimensionalized by the liquid-vapor surface tension σ , l is the length of the receding contact line, and θ_l is the instantaneous contact angle along the pinned contact line. The θ_0 in Equation 4.1 is the equilibrium contact angle without pinning in the absence of the nanocavity for the liquid. To compute the pinning force in Equation 4.1, we discretize the contact line into N equally spaced intervals. As such, Equation 4.1 is written as a series:

$$\bar{f}_p \approx \frac{\sum_{i=1}^N (\cos \theta_{l_i} - \cos \theta_0) l_i}{\pi\theta_0^2}. \quad (4.2)$$

where $N = 3$ and 5 for small and large distortions, respectively.

Considering $\theta_0=83$ (water on silicon substrate), we present the pinning force from Equation 4.2 vs. distortion in Figure 24A, where symbols represent the simulation data, and lines are the linear fits. Symbols and lines are color coded from red to blue, respective to upward triangular, horizontally oriented elliptical, square, circular, downward triangular, and vertically oriented elliptical nanocavities. Here, as previously proposed for circular inhomogeneities, (160; 161) we are assuming that the pinning force is linearly proportional to distortion

for other nanocavity geometries as well. For every above mentioned nanocavity geometry, we performed 5 simulations to further lower the variance in the slope of fitted lines.

From Figure 24A, we find the slope of fitted lines, which is equivalent to the spring constant of the nanocavity expressed by

$$k = \frac{\bar{f}_p}{d}. \quad (4.3)$$

Figure 24A suggests that spring constant of the contact line for localized perturbation varies across different nanocavity geometry. According to Figure 24, the spring constant is the largest for the upward triangular nanocavity, and decreases for horizontally oriented elliptical, square, circular, downward triangular, and vertically oriented elliptical nanocavities, in that order.

Figure 24B compares the spring constant for the corresponding nanocavity geometries in Figure 24A with the one from the experiment, (161) illustrated by the dashed line, using three different micron sized polystyrene spherical beads. Error bars for the simulation results highlight the standard deviation sampled over 5 different simulations. It is noteworthy that the results from the experiment have indicated a fixed spring constant for the three different circular cross-section areas. We find that the spring constant from the simulations for the circular nanocavity is in reasonable agreement with that from the experiments. Results in Figure 24B also suggest that the spring constant varies across different nanocavity geometries despite equal cross-section area and total volume of nanocavities. Overall, Figure 24A and B indicate that the pinning force acting on receding contact line and associated spring constant are dependent on the geometry of nanocavity. Our findings suggest that the upward triangular

nanocavity imposes the largest pinning force while the vertically oriented nanocavity exerts the smallest for a given distortion.

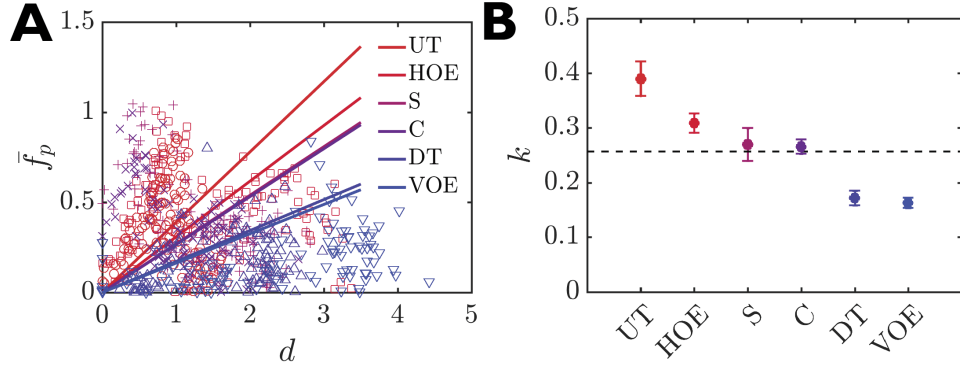


Figure 24: (A) The variation of pinning force against distortion for upward triangular (UT), horizontally oriented elliptical (HOE), square (S), circular (C), downward triangular (DT), and vertically oriented elliptical (VOE) nanocavities, color coded from red to blue, respectively. Symbols are the distinct force-distortion measurements taken from MDPD simulations and solid lines are the fits. (B) Comparison of spring constants taken from the linear fits in Figure 24A (solid lines) with that from experiment (dashed line), using spherical defects.

4.3.4 Pathline

To further understand the interaction of a nanocavity with the receding contact line, we consider the pathlines of tracer particles at the receding contact line in the vicinity of the nanocavity. We find that majority of the liquid particles, which ultimately remain inside the nanocavity after depinning, are not initially placed in the nanocavity, i.e. liquid inside the nanocavity is constantly recycled as the receding contact line is approaching. To further verify this finding, we sample 7 tracer particles, which are initially positioned at equally spaced loca-

tions on the contact line when it is located slightly above the nanocavity. We then monitor the tracers' trajectories. A snapshot of such trajectories is shown in Figure 25A and B, respective to front and side view. We also consider the trajectories of similar particles starting at the contact line when it is located right above the nanocavity, shown in Figure 26A and B, front and side view, respectively. We color coded the trajectories from red to blue to distinguish the direction of the tracers' motion from beginning to the end.

These trajectories suggest that a particle starting at the contact line mostly follows a projectile motion in clockwise fashion, starting from the substrate, moving up along the liquid-vapor interface, and then going down towards the substrate. The pathlines in Figure 25 and Figure 26 also imply a rotational flow field in addition to the brownian motion near the contact line. Such caterpillar motion was first reported by Dussan *et al.*(170) for an advancing contact line in front of a precursor layer along the substrate, and sliding liquid drops. (155) We observe similar circular motion and rotational flow of liquid particles yet for a receding contact line and in the presence of a nanocavity. Furthermore, we notice that some pathlines starting on both sides of the nanocavity in Figure 26A, ultimately lean towards the center of the nanocavity, which we attribute to the pinning of the contact line to the periphery of the nanocavity.

4.3.5 Dynamic contact angle

Pinning of a contact line to a nanocavity not only affects the distortion and pinning force, but also the dynamic contact angle. The variation of both advancing and receding dynamic contact angles in sliding liquid drops have extensively been studied before. (171; 19; 172; 173; 174; 175) However, almost all molecular simulations and computational models have focused on advancing

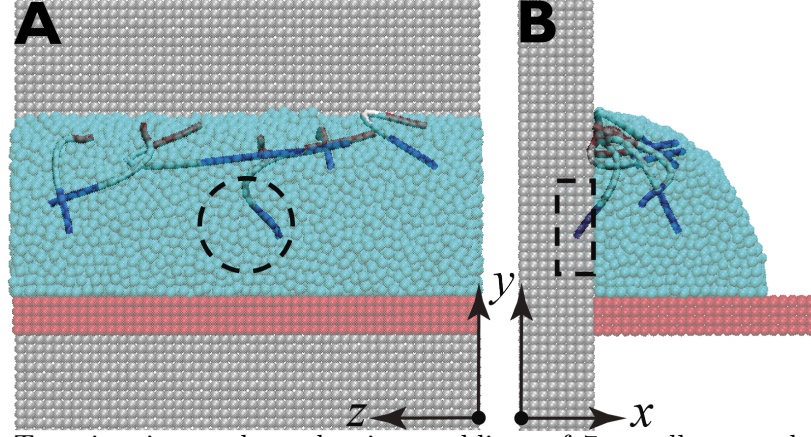


Figure 25: (A) Top view in yz -plane showing pathlines of 7 equally spaced tracer particles sampled along the contact line slightly above the nanocavity. The pathlines are color coded from red to blue, respective to the progression of trajectories. The dashed line represents the circular nanocavity. (B) Side view in xy -plane displaying the pathlines following a large circular (caterpillar) motion.

or receding dynamic contact angles for axisymmetric fluid geometries, such as spreading or evaporating droplets. However, variation of dynamic contact angle along a pinned contact line, which is not axisymmetric, for different fluid-solid interactions, and in the presence of a nanocavity with various shapes has not been explored. Here, we discuss the impact of a nanocavity on the dynamic contact angle measured for different nanocavity shapes, at various points on the receding contact line while it is pinned to part of the periphery of the nanocavity.

We illustrate the dynamic contact angle variations along three cross sections, **a-a** (red), **b-b** (magenta), and **c-c** (blue), as shown in Figure 27A. Cross section **a-a** and **b-b** are equally spaced from the side-end to the nanocavity centerline, with a separation of 8.33 (in MDPD units), while cross section **c-c** is the centerline of the nanocavity. Dynamic contact angle

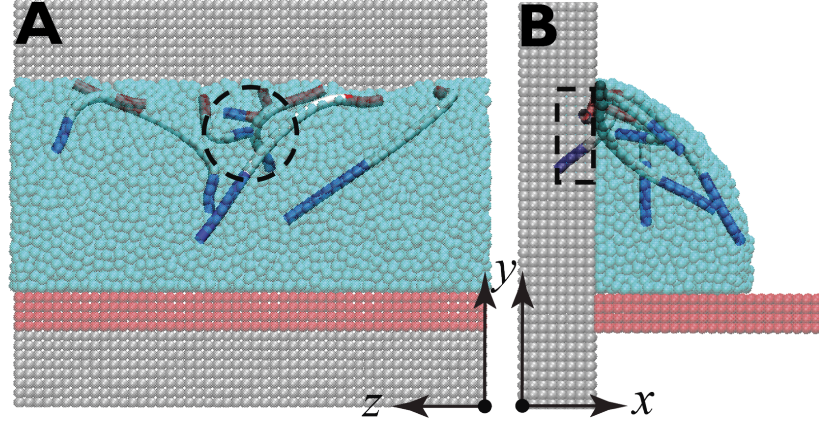


Figure 26: (A) Top view in yz -plane showing pathlines of 7 equally spaced particles sampled along the contact line, when it is right above the nanocavity. The pathlines are color coded from red to blue, corresponding to the progression of trajectories. The dashed line represents the circular nanocavity. (B) Side view in xy -plane displaying the pathlines following a large rotational flow field.

hysteresis for the three cross-sections, **a-a**, **b-b** and **c-c**, are averaged over 10 simulations, and shown in Figure 27B. Shaded area in Figure 27B highlights the onset of pinning and depinning events. Top to bottom panels in Figure 27B correspond to different solid-liquid pair-potential attraction parameter $A_{sl} = -30, -35$, and -38 , respectively. As the magnitude of A_{sl} increases, the liquid becomes more hydrophilic.

The results in Figure 27B suggest that the dynamic contact angle along **a-a** cross section is slightly affected, up to a few degrees, by the presence of the nanocavity and pinned contact line, regardless of the solid-liquid pair-potential attraction strength, A_{sl} . However, the dynamic contact angle for points on the contact line that are closer to the nanocavity centerline, further decreases by the contact line pinning, as shown by dynamic contact angle variation along the **b-**

b cross section. This reduction in the dynamic contact angle is the largest along the nanocavity centerline, as illustrated by the dynamic contact angle along the **c-c** cross section. The dynamic contact angle in **b-b** and **c-c** cross section continues to decrease with the progression of the pinning as shown by dynamic contact angle variation in shaded area in Figure 27B. The results also suggest that the difference between dynamic contact angles along **a-a** and **c-c** cross sections for the smallest solid-liquid pair-potential attraction strength considered in this work, $A_{sl} = -30$, can be as large as 28° , as depicted in the top panel of Figure 27B. Such a reduction in the dynamic contact angle upon pinning is indicative of a clamping effect, which is localized at the nanocavity, and is the largest at the nanocavity centerline. Since this clamping effect is directly correlated with the dynamic contact angle, it vanishes once it gets to about two diameters away from the nanocavity centerline, where cross section **a-a** is located. We note that the clamping effect has an implication on directed self-assembly of nanoparticles into templated surfaces, (58; 60; 59) which can generate a guided pathway for the nanoparticles towards the nanocavities. The clamping effect can also aid in trapping the nanoparticles in the nanocavities, and blocking the nanoparticles on the way out.

Increasing A_{sl} in magnitude from -30 to -35 also revealed that as the liquid becomes more hydrophilic, the clamping effect reduces as shown in Figure 27B. Likewise, for $A_{sl} = -38$, that is close to the liquid-liquid pair-potential attraction strength, $A_{ll} = -40$, the results in Figure 27B, bottom panel, suggest a small change, up to a few degrees, in the dynamic contact angle even along the **c-c** cross section. This result implies that hydrophilicity of the substrate and distance from the nanocavity are two key factors in providing the clamping effect. Besides

the clamping effect, increasing A_{sl} forces the contact line to further slide over the periphery of the nanocavity before it is pinned. Such sliding of the contact line is manifested in the delay for the unset of pinning, started at $\sim t = 0.4 \times 10^4$ (in MDPD time units) for $A_{sl} = -30$, compared to $t = 0.7 \times 10^4$ for $A_{sl} = -35$, shown by shaded area in Figure 27B, top and middle panel, respectively. Sliding of the contact line and the subsequent contact-line pinning is further delayed to $\sim t = 1.3 \times 10^4$ for $A_{sl} = -38$, as illustrated in Figure 27B, bottom panel.

To unravel the effect of nanocavity geometry on the variation of dynamic contact angle across the pinned contact line, we performed aforementioned analysis using various nanocavity geometries shown in Figure 28A-E. Figure 28A to E illustrate snapshots of a pinned contact line around the periphery of a nanocavity with upward triangle, horizontally oriented ellipse, square, downward triangle, and vertically oriented ellipse cross section, respectively, at $t = 10^4$ during MDPD simulations with $A_{sl} = -30$. In these simulations, the contact line is forced to move from top to bottom, while the piston (red plate in Figure 28) is pulled down. We then measured the contact angle variation during the pinning and unpinning events, along the three cross sections depicted in Figure 27A, whose results are shown in Figure 29. The results compare the dynamic contact angle variations, averaged over 10 simulations, for the downward triangular, horizontally oriented elliptical, square, circular, upward triangular, and vertically oriented elliptical nanocavity, from red to blue, respectively, as illustrated in Figure 29A to C, respective to cross sections **a-a**, **b-b**, and **c-c**.

The results suggest that variation of the dynamic contact angle is almost indistinguishable across different nanocavity geometries, at distances far from the nanocavity, as shown along

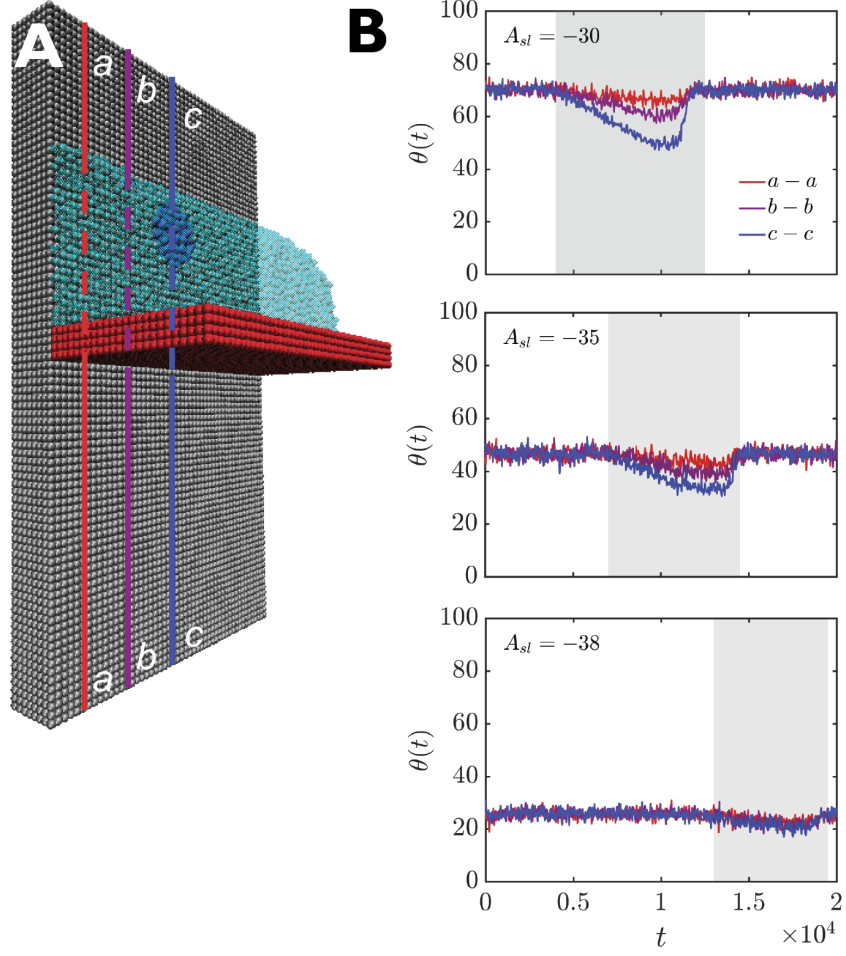


Figure 27: (A) A receding contact line is pinned once the liquid (cyan) is pulled down by the piston (red) to go over a circular nanocavity (blue) on an otherwise flat substrate (gray). Dynamic contact angle is monitored along a-a (red line), b-b (magenta line) and c-c (blue line) cross sections. (B) The variation of dynamic contact angle against the MDPD time along a-a, b-b and c-c cross sections, with $A_{sl} = -30$, -35 and -38 , from top to bottom, respectively, averaged over 10 simulations.

cross section a-a in Figure 29A. These distances are generally longer than two diameters away from the center of the nanocavity for equivalent circular nanocavity of the same cross-section

area. Our simulation results suggest that variation of the dynamic contact angle is minimal, up to a few degrees, along cross section **a-a**.

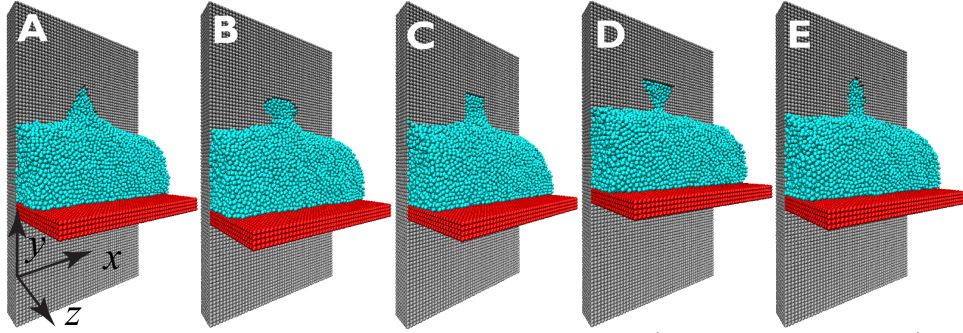


Figure 28: A pinned contact line is depicted while the liquid (cyanMDPDparticles) is going over a nanocavity with upward triangle, horizontally oriented ellipse, square, downward triangle, and vertically oriented ellipse cross section, A to E, respectively, as the piston (red plate) is pulled down.

However, the impact of nanocavity geometry on the dynamic contact angle is more pronounced as we get closer to the nanocavity along cross section **b-b**, which is one diameter away from the center of the nanocavity for the equivalent circular geometry, as depicted in Figure 29B. Results in Figure 29B indicate that vertically oriented ellipse exhibits the least variation in the dynamic contact angle (~ 7 degrees), while upward triangle and horizontally oriented ellipse show the most variation (~ 16 degrees) with respect to the equilibrium receding contact angle, along **b-b** cross section. Such dynamic contact angle variation persists along cross section **c-c** on the nanocavity centerline as shown in Figure 29C. The dynamic contact

angle variation reaches its maximum on cross section c-c for all nanocavity geometries, with the largest being for upward triangle and horizontally oriented ellipse. The dynamic contact angle variation along cross section c-c decreases for square, circle, and downward triangle. The smallest variation of dynamic contact angle occurs on the vertically oriented ellipse centerline. The shaded regions in Figure 28 marks the union of the onset of pinning and complete depinning processes for the 6 geometries studied.

We conjecture that the dynamic contact angle variation is correlated with the length perpendicular to the direction of the contact-line motion along which contact line is pinned. In particular, for vertically oriented ellipse, the largest length perpendicular to the direction of the contact-line motion is the minor axis, which is smaller than the side of square and triangle, and diameter of the equivalent circle. Hence, it has the least dynamic contact angle variation, as shown in Figure 29B and C. On the other hand, upward triangle, and horizontally oriented ellipse have the largest length perpendicular to the direction of contact-line motion, along which the contact line is eventually pinned. Side length of the equilateral triangle is 6.73, and major axis of the horizontally oriented ellipse is 7.06. We note that the downward triangle has also the same side length as the upward triangle; however, the dynamic contact angle variation in downward triangle is not as large as that in the upward triangle. Our results suggest that the length of pinned contact line right before depinning matters. In downward triangle, right before depinning, the contact line is pinned very close to the bottom vertex, which leaves a small length along which the contact line is pinned. In contrast, for the upward triangle, the length along which the contact line is pinned before depinning, is almost the full side length (6.73), which

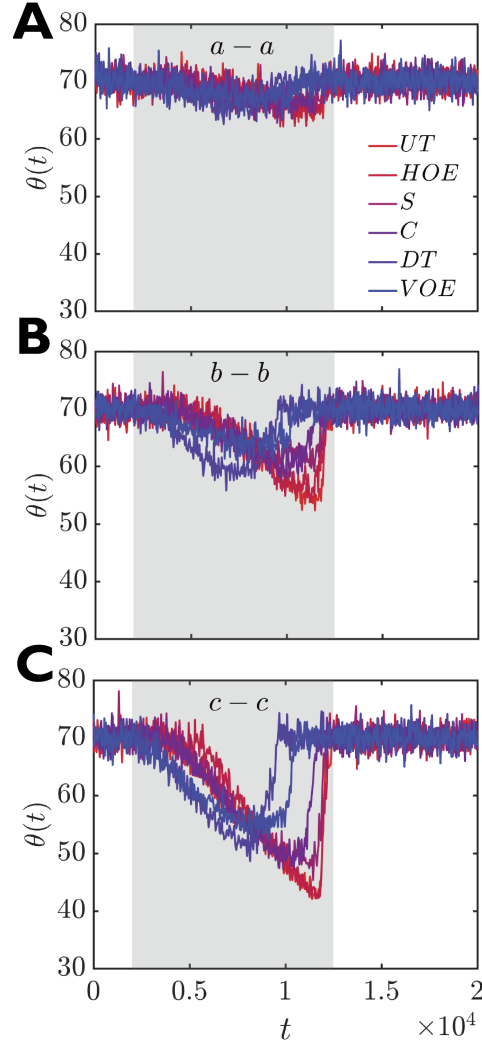


Figure 29: Variation of the dynamic (receding) contact angle along **a-a** (A), **b-b** (B), and **c-c** (C) cross section, as shown in Fig. Figure 27A. The dynamic contact angle variations are color-coded from red to blue, respective to Upward Triangular (UT), Horizontally Oriented Elliptical (HOE), Square (S), Circular (C), Downward Triangular (DT), and Vertically Oriented Elliptical (VOE) nanocavity.

is clearly larger than the side of the square (4.43) or diameter of the equivalent circle with the same surface area (5). Consequently, the dynamic contact angle variation in upward triangular

nanocavity is larger than that in square and circular nanocavity. Our simulations also indicate the effective length of the pinned contact line before depinning in horizontally oriented ellipse is smaller than the upward equilateral triangle side length. As such, the variation of the dynamic contact angle is the largest in the upward triangle.

To confirm the magnitude of the change in the dynamic contact angle, we measured its largest variation during the unpinning event, whose results are shown in Figure 30 for the 6 geometries considered above. In Figure 30, dots correspond to the maximum of the variation of the contact angle averaged over 10 simulations, and error bars indicate the standard deviation. We find that the results shown in Figure 30 are also correlated with the spring constant of the pinning force associated with the above mentioned geometries, illustrated in Figure 24B. These results suggest that the nanocavity geometries with large spring constant most likely exhibit a large variation in dynamic contact angle during depinning. We attribute this direct correlation to the fact that for a fixed distortion, nanocavities with large spring constant will experience a large pinning force. This large force will in turn pull the liquid in the direction opposite to the flow direction, lower the dynamic contact angle along the c - c direction, and consequently increase the change in the dynamic contact angle.

In this work, although we have focused on the impact of nanocavity shape on the distortion, pinning force, and dynamic contact angle variation, the aforementioned analyses can be readily extended to nanopillars, which we leave for a future work.

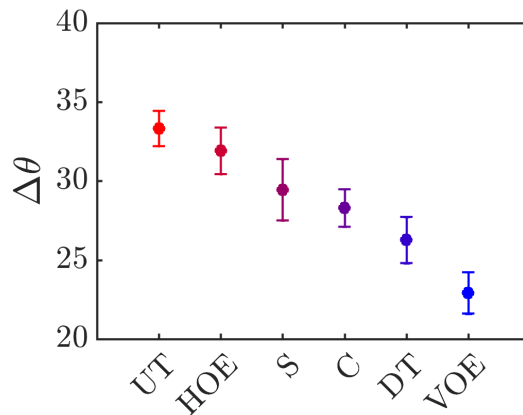


Figure 30: Maximum variation of the dynamic contact angle along cross section **c-c** for the 6 geometries in Figure 29C averaged over 10 simulations (dots) and the respective standard deviation shown by the error bars.

4.4 Conclusions

In the present study, we performed a series of coarse-grained MD simulations to provide a molecular view of the impact of the nanocavity geometry on the pinning force, distortion, and contact angle of a receding contact line for a liquid film while it is pinned to the periphery of a localized perturbation in the form of a nanocavity. Our simulations have demonstrated the effect of geometry of a localized perturbation in the form of a nanocavity, on the pinning force as a function of distortion, and the corresponding spring constant. We showed that the distortion of the contact line largely varies across different nanocavity geometries. The results presented here suggest that high curvature points on the periphery of the nanocavity has a significant impact on not only the distortion, but also the pinning force, and consequently the spring constant of the nanocavity. In addition, the effective length perpendicular to the

receding direction during depinning is directly correlated with the maximum variation of the receding contact angle, and spring constant of the nanocavity. We found that upward triangular nanocavity has the largest, while the vertically oriented elliptical nanocavity has the smallest spring constant among the geometries considered in this work. We showed that the flow field in the proximity of liquid-vapor interface of a receding contact line in a thin liquid film that is partially pinned, follows a caterpillar-motion, similar to the mechanism of an advancing contact line in precursor thin films. Our results indicated a localized confinement due to variation of the dynamic contact angle along the pinned contact line, which is akin to the clamping effect. It was also shown that the clamping effect, caused by the reduction of the receding contact angle, is impacted by the nanocavity geometry and hydrophilicity of the liquid. Overall, we believe the simulation results provided in this work have the potential to assist with the design of the nanocavity geometry, and guide the experimental efforts in making capillary assisted SA of nanoparticles into nanocavities, which occurs at the receding contact line, robust with high yield on large areas.

Here, we only considered the dewetting of the liquid film in the presence of a single nanocavity. Additional work is warranted to show the interface dynamics in the presence of a grid of nanocavities, and nanoparticles suspended in the liquid. Ultimately, understanding the fluid dynamics during dewetting on patterned surfaces will unravel the mechanisms of guided SA of nanoparticles into substrates, which are templated with nanocavities.

CHAPTER 5

IMPACT OF TEMPLATE GEOMETRY AND CONFINEMENT ON DIRECTED SELF-ASSEMBLY OF NANOPARTICLES

5.1 Introduction

Directed self-assembly of nanoparticles (DSA-n) onto templated surfaces is currently gaining attraction due to the continuous progress in miniaturization of nanodevices for numerous applications, including plasmonics, (37; 176; 17; 177) semiconducting devices, (41; 178; 179; 180) and photovoltaics (32; 48; 49; 181). The surface-modified substrate serves as a template on which nanoparticles can be selectively arranged into configuration with a morphology that is complementary to that of the template. (182; 183; 184; 185) Taking advantage of lithographically-patterned template, DSA-n is able to induce orientation-dependent interactions and organize individual components in the bottom-up fabrication process that help create complex morphology beyond classical self-assembly. (29; 30; 26; 186; 187) The specific design of template in DSA-n also provides an opportunity to exploit the collective properties of nanoparticle assembly with controlled geometries, compositions and functionalities. (54; 31; 56; 57; 188) These controlled geometries include ordering and orientation of particle assembly on substrate, which can be demonstrated by developing appropriate experimental setups.

Studies have shown that the evaporation of a liquid drop on a templated surface can facilitate the self-assembly process; (189; 178; 55) however, the inherent restriction on size of template

prevents the scalability of evaporative DSA in large area production. In contrast to DSA with liquid drops, several studies applied gravitation-induced dewetting of a tilted liquid film in between two parallel fixed plates, the bottom of which is lithographically-defined. (190; 191; 192; 193) Another commonly used setup involves relative sliding of a liquid film in between two plates, either one plate drags the liquid film over the templated slide beneath the liquid film. (52; 53; 57; 194) Both aforementioned techniques demonstrate uncontrolled aggregation, defects, or scalability for DSA-n at sub-10 nm, due to the mixed long range molecular forces from different layers of micrometer-thick liquid film and Brownian motion acting on the nanoparticles. (195; 58; 196; 59)

Recent progress in spreading mediated DSA-n at sub-10 nm regime has provided a direction to control the long-range molecular forces by creating a very thin film sliding over the templated surface. This thin film allows high yield of single nanoparticle positioning in the nanocavities with specific ordering or alignment. (60; 197) The spreading mediated DSA involves with spontaneous climbing of a thin liquid film along a vertical substrate with a thickness of about 100 nm, followed by a receding meniscus sliding over a templated substrate. Although the fabrication technique is able to achieve ordered arrays of nanoparticles on the templated substrate with single particle resolution at each nanocavity, the underlying dynamics of nanoparticle deposition is still unclear. Moreover, high fabrication cost, and numerous tunable parameters such as liquid film property, and template geometry hinder experimental exploration of parametric relation in improving the yield with scalability. To address the difficulties, computational mod-

eling offers some flexibility to explore a variety of parametric conditions, and investigate the dynamics of DSA-n at sub-10 nm.

Recent Brownian Dynamics BD simulations have shown that the Brownian motion and pairwise interactions strongly affect the dynamics of DSA-n at sub-10 nm; thus, creating an undesirable random assembly on the templated surface. (59; 60) BD and Dissipative Particle Dynamics (DPD) simulations were also reported as a suitable platform to investigate the dynamics of DSA-n at interface. (198; 199; 200; 201) Nevertheless, to simulate air-fluid interface in DSA-n, one requires to model the gas phase (air) in addition to the liquid phase, which exceedingly increases the computational cost. In this chapter, we utilize the Many-Body Dissipative Particle Dynamics (MDPD) simulations, which are a modified version of DPD simulations. As a coarse-grained technique, MDPD is capable of incorporating both microscopic and mesoscopic physics while recovering properties of multiphase fluids at time. In addition, MDPD is able to simulate free liquid/vapor interfaces by including both attractive and repulsive soft potentials that achieve a cubic pressure-density relation. (130) This is particularly useful when a gas-liquid interface needs to be modeled. Compared to MD simulations, with MDPD simulations, one can potentially reach a spatial scale several orders of magnitude larger than that captured by MD simulations. (129)

MDPD has been extensively used in studies of sliding liquid drop, (19) liquid film pinning, (148) capillary imbibition and drainage, (126) and evaporation-mediated DSA-n. (202) To study DSA-n of sub-10 nm particles using MDPD simulations in this chapter, we model the interactions among the solid substrate, liquid and nanoparticles within the receding thin liquid

film sliding over a templated substrate. We pay a particular attention to the mechanism of the self-assembly and driving forces that govern the yield to be able to control DSA-n process.

5.2 Theoretical Model

5.2.1 MDPD model

We utilize MDPD model, as described in chapter 3.2, to understand the mechanisms of DSA-n, kinetics, and dynamics of nanoparticles.

To account for the mass and volume difference between conventional particle (liquid, solid) and nanoparticle in MDPD model, we replace the cutoff distance (r_c and r_d in Equation 3.6) with three alternatives for $r_{c,ij}$ and $r_{d,ij}$ by introducing the nanoparticle radius R ,

$$r_{c,ij} = \begin{cases} r_{c,11} = r_c & \text{if a pair of regular particles} \\ r_{c,12} = R + r_c & \text{if a pair of regular particle and nanoparticle} \\ r_{c,22} = 2R + r_c & \text{if a pair of nanoparticles} \end{cases} \quad (5.1)$$

Correspondingly, we set $r_{d,ij} = 0.75r_{c,ij}$ for all three cutoff distances in Equation 3.6.

5.2.2 Simulation setup

In this chapter, we model a vertical solid substrate using uniformly-arranged particles in fcc configuration (hereafter solid particles), and fix their positions throughout the entire MDPD simulation. In the middle and on the surface of the substrate, we create a square array of cylindrical nanocavities (hereafter nanocavities) with identical radius, depth, and interspacing. Above the nanocavity array, we construct a thin liquid film by randomly placing liquid particles

and nanoparticles in a box laid on over the substrate, which will serve as the initial condition for MDPD simulations. We then place a thin layer of frozen particles, perpendicular to the substrate, mimicking a piston, which bounds the liquid film from below, as shown in Figure 31. To set up the simulations, we first equilibrate the liquid film to achieve a well-defined liquid-vapor interface, followed by pulling the piston downward with a constant speed along the substrate. The motion of piston will drag the liquid film, and force it to slide over the substrate and the nanocavity array.

In order to avoid undesired penetration of liquid particles into the substrate and piston, the lattice constant of fcc structure is chosen to be smaller than the average distance between liquid particles. This limit will lead to particle distribution for the substrate and the piston to be denser than that for the liquid film. We only allow shallow penetration of liquid particles into the nanoparticles by adjusting the nanoparticle-liquid interaction parameters, A_{nl} and B_{nl} , in Equation 3.2. We apply periodic boundary conditions in the z -direction.

In our simulations, we use dimensionless quantities, which are nondimensionalized by the physical units of length, mass, time, and energy of a real liquid. The characteristic length, mass, time, and energy units were discussed in chapter 3.2. We summarize these parameters in Table V (otherwise refer to Table III), where the liquid-liquid, substrate-liquid, and piston-liquid attraction parameters are indicated by A_{ll} , A_{sl} , and A_{pl} , respectively.

TABLE V: MAPPING BETWEEN DIMENSIONLESS AND DIMENSIONAL SIMULATION PARAMETERS

Description	Symbol	MDPD units	Physical units
Attraction parameter	A_{ll}	-40	-5.84×10^{-10} N
Attraction parameter	A_{sl}	-30	-4.38×10^{-10} N
Attraction parameter	A_{nn}	-300	-4.38×10^{-9} N
Attraction parameter	A_{nl}	-150	-2.19×10^{-9} N
Circular cavity diameter	d_{ca}	5	2.97×10^{-8} m
Circular cavity depth	h_{ca}	2	1.19×10^{-8} m
Piston velocity	v_p	0.005	0.369 m/s

5.3 Results and Discussion

5.3.1 Progression of DSA-n on template substrate

We perform MDPD simulations to study the mechanisms of DSA-n from a receding liquid film on to a templated substrate. In these simulations, we take into account the impact of confinement (liquid film thickness) and nanoparticle density on the yield. We measure the yield by the percent of nanocavities in the array, which are filled by the nanoparticles. For the initial condition, we set the thickness of liquid film to $d = 5$, and the concentration of nanoparticles to $\rho = 0.07$ after equilibration. Equilibration is performed by running the simulation long enough to achieve a stable liquid-vapor interface between the thin liquid film and the vapor phase. We then move the piston to drag the liquid film downward with a constant speed of v_p (see Table V), and slide over the array of nanocavities in the substrate. Figure 31A-D shows the DSA-n and progression of receding liquid film from top to bottom. Gray, purple, and cyan particles represent the substrate, piston, and liquid film, respectively. Figure 31E is the top view of Figure 31D, where the liquid particles have been removed for clarity, yellow

particles represent the nanoparticles that are still in the liquid thin film, and red particles are those directly self-assembled. We clearly observe the pinning phenomena at the receding contact line, which is shown by the corrugated contact line, while the meniscus is sliding over the nanocavities. In the simulations, liquid evaporation is also observed, which leads to either liquid droplets formation, or moving particles in the gas phase.

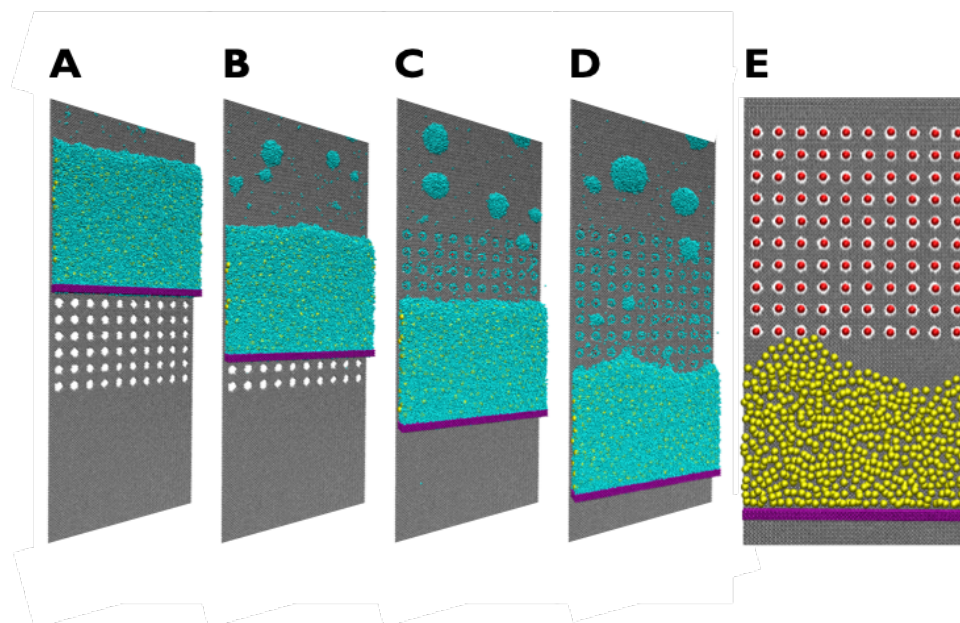


Figure 31: Progression of a liquid thin film sliding over a substrate with templated array of circular nanocavities from top to bottom (A-D) is shown while the purple piston is pulled down to conduct DSA-n. Top view of panel D indicates deposition of nanoparticles (red particles), where liquid particles (cyan) are turned off for clarity (E).

The results shown in Figure 31 indicate 100% yield for DSA-n via a receding liquid film. To investigate whether the same yield is achievable via an advancing liquid film, we conduct an MDPD simulation with an advancing liquid film going over the same templated substrate, as shown in Figure 32A-D. For this simulation setup, we partially submerge the bottom of the substrate in a liquid bath with same initial concentration of nanoparticles. This setup allows a thin liquid film to emerge from the liquid bath, and climb the substrate surface, while we restrict the liquid film thickness to $d = 5$, which is the same thickness as that in the receding liquid film test mentioned above. The advancing liquid film exhibits a yield of 0.5 when the liquid film completely covers the nanocavity array in the substrate as shown in Figure 32E. For clarity, the MDPD (cyan) particles illustrating the liquid phase have been turned off in Figure 32E.

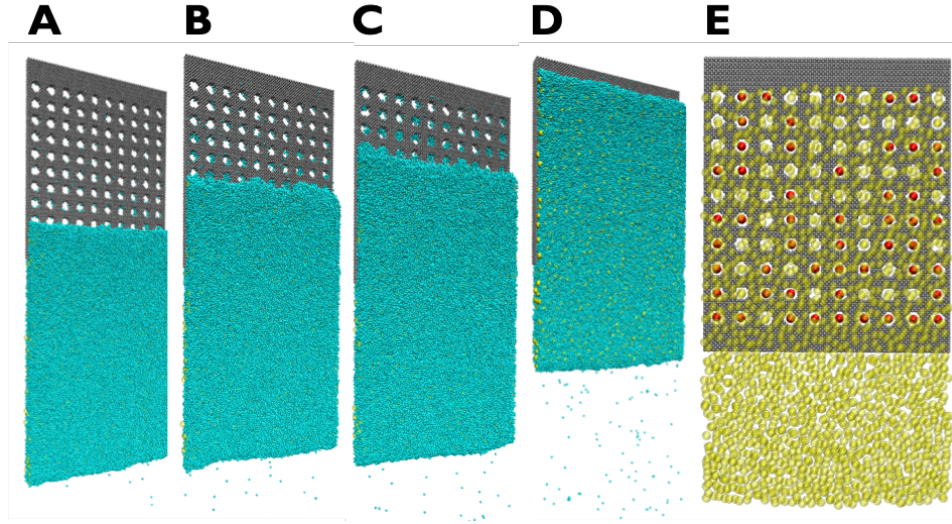


Figure 32: Progression of an advancing liquid film (cyan) with suspension of nanoparticles, moving over a templated substrate (gray) with an array of circular nanocavities (white holes) from bottom to top (A-D). Top view of the same snapshot in D while liquid particles are turned off for clarity. Red particles represent directly self-assembled nanoparticles, whereas yellow ones illustrate those in the bulk liquid.

Despite the similar construction of substrate and liquid film, and particle interaction parameters between advancing and receding liquid film simulations, there is a considerable difference in the yield of DSA-n. MDPD simulation results indicate that the former has yield of 0.5 whereas the latter has yield of 1. As we will discuss later, we hypothesize that one mechanism of DSA-n is by random motion of nanoparticles. We also hypothesize that the receding contact line prevents the self-assembled nanoparticles from leaving the nanocavities, which cannot be

enforced by the advancing contact line. To prove these hypotheses, we will look at the impact of the liquid film confinement, nanoparticle density, and template geometry on the yield in DSA-n.

5.3.2 Confinement impact on the yield of DSA-n

5.3.2.1 DSA-n phase diagram

To explore the yield of DSA-n as a function of liquid film thickness (confinement) and nanoparticle density, we perform a series of MDPD simulations. In these simulations, we measure the yield while varying the liquid film thickness, d , from 3 to 15 with an interval of 2, and nanoparticle density, ρ , from 0 to 0.15 with an interval of 0.01 in Figure 33. We determine the yield after the receding contact line crosses the bottom most line in the array of 10×10 circular nanocavities, as shown in Figure 31E. To obtain the statistics of the DSA-n, we measure the yield by averaging over all four quadrants of 5 subarrays. Subsequently, we calculate the standard deviation using the yield of each quadrant, which was found to be less than 0.07 for any combination of d and ρ as mentioned above. We then use machine learning to predict the yield for any $3 \leq d \leq 15$ and $0 \leq \rho \leq 0.15$. We employ the neural network for the machine learning algorithm, and use the calculated yield obtained from the discretized d and ρ as discussed above for the training dataset. The yield phase diagram is shown in Figure 33 color coded from red to blue, respective of 1 to 0. From the phase diagram in Figure 33, we observe that for a given nanoparticle density, the yield decreases as thickness of liquid film increases. A small liquid film thickness leads for further confinement of nanoparticles, and increases the chance of nanoparticles randomly move to the nanocavities. From the phase diagram in Figure 33,

we also find that yield is generally low at low and high densities, and reaches its maximum at about $\rho = 0.07$. The range at which the yield is maximum also decreases with the liquid film thickness. To further justify our observations, we look at the yield variation through the phase diagram at constant nanoparticle density and liquid film thickness, as discussed below.

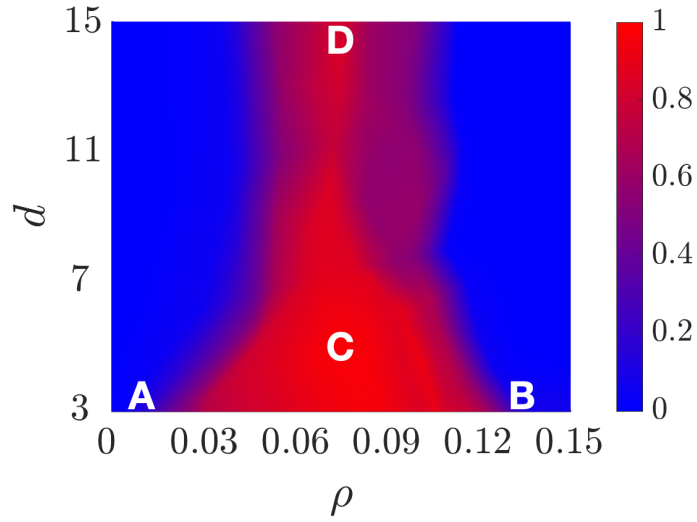


Figure 33: The phase diagram of yield of DSA-n as a function of nanoparticle density, ρ , and the liquid film thickness, d . Nanoparticle configuration for points A-D on the phase diagram are visualized in Figure 36.

5.3.2.2 Thickness variation

To better understand the variation of yield in the phase diagram, we take a close look at yield at constant density while varying the thickness of liquid film. Figure 34 shows the variation of yield vs. thickness at 3 nanoparticle densities, $\rho = 0.05$ (red), 0.07 (blue), and 0.09 (black). According to Figure 34, the yield decreases with the thickness of liquid film regardless of the density. However, the reduction of yield with thickness at nanoparticle densities of $\rho = 0.05$ and $\rho = 0.09$ is more pronounced than that at $\rho = 0.07$. The yield at $\rho = 0.07$ is slightly higher than 80% on average over the range of thickness shown in the phase diagram in Figure 33. The results suggest that DSA-n at $\rho = 0.07$ leads to a yield higher than that at other densities.

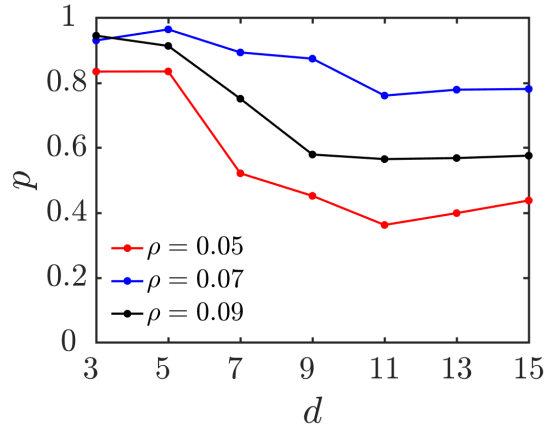


Figure 34: The yield of DSA-n (p) into a 10×10 array of circular nanocavities against the liquid film thickness (d) at fixed nanoparticle density, $\rho = 0.05$, 0.07 , and 0.09 , corresponding to red, blue, and black, respectively.

5.3.2.3 Nanoparticle concentration variation

We also look at the yield in the phase diagram while allow ρ to vary from 0 to 0.15 while keeping liquid film thickness constant at $d = 3, 5$ and 7 . As is shown in Figure 35, the yield of DSA-n is minimum at low and high densities, and is maximum at densities of about $\rho = 0.07$. Furthermore, the range at which the optimum yield is observed decreases with the liquid film thickness, as illustrated in Figure 35. The results from Figure 34 and Figure 35 suggest that there is a range of nanoparticle density and liquid film thickness in which the yield is optimum. We note that this range also depends on the two underlying variables, nanoparticle density and liquid film thickness.

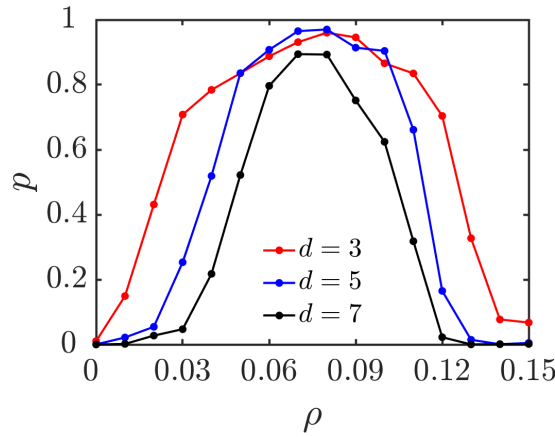


Figure 35: The yield of DSA-n vs. concentration of nanoparticles at fixed liquid film thickness of $d = 3, 5$ and 7 , respective to red, blue, and black.

We present the particle configurations for four selected points, A-D, on the phase diagram in Figure 33. These configurations are shown in Figure 36A-D, respectively. Top panels are the last snapshot of the MDPD simulations, where the piston (purple block) has reached to the bottom of the substrate (gray). We measure the yield from the 10×10 array of circular nanocavities (white holes), which are etched out of the substrate. In these simulations, the red and yellow particles represent deposited, and suspended nanoparticles in the bulk liquid, respectively, and liquid particles (cyan) are not pictured for clarity. Figure 36A and B demonstrate low yield while they have identical liquid film thickness, hence identical confinement; however, the nanoparticle density in A ($\rho = 0.01$) is much lower than that in B ($\rho = 0.14$). The results also indicate very different nanoparticle configurations. The nanoparticle configuration is very sparse in Figure 36A, whereas it is closely packed and relatively ordered with short range correlation in Figure 36B.

In contrast, Figure 36C and D demonstrate relatively high yield and identical nanoparticle density; however, they differ in liquid film thickness. The former has a liquid film thickness of $d = 3$, whereas the latter has a liquid film thickness of $d = 13$. The results suggest that both nanoparticle configurations are disordered despite different liquid film thicknesses. From the yield at points A to D shown in Figure 36A to D (top row), we conjecture that large density does not necessarily leads to a high yield. Indeed we find that at large densities, the near neighbor distance between nanoparticles are minimal on average, which leads to high attraction between the nanoparticle; hence, there is an energetic barrier for a nanoparticle to randomly move into a nanocavity. Obviously, at low nanoparticle densities, there is not enough

nanoparticles to randomly explore the nanocavities either. Furthermore, at low nanoparticle density, if a nanoparticle moves into a nanocavity, it is very likely that it freely goes back to the bulk to increase the system entropy. Overall, we find that there is an optimal nanoparticle density which most likely leads to the maximum yield. The optimal density should depend on the liquid properties and substrate, liquid, and nanoparticle interaction characteristics.

Our results also indicate a correlation between the yield and ordering of the nanoparticles in the bulk. In particular, for points C and D on the phase diagram, we observe that the high yield occurs where the system is disordered. Middle row of Figure 36C and D illustrates the 2D bond orientational order parameter per particle color coded from blue to red, respective to 0 (very disordered) and 1 (very ordered). We determine the 2D bond orientational order parameter (203) per particle as well as the bulk average to quantify crystalline ordering of the nanoparticle monolayer. The bond orientational order parameter is defined by:

$$\Psi_6 = \left| \left\langle \frac{1}{nn} \sum_{k=1}^{nn} e^{6i\theta_{jk}} \right\rangle \right|, \quad (5.2)$$

where nn is the number of nearest neighbors, which are determined by the Voronoi diagram. (204). In Equation 5.2, θ_{jk} is the bond angle between particle j and its nearest neighbor k , and $i = \sqrt{-1}$.

Point B with the lowest yield of 0.1, and the largest density among the four points on the phase diagram has the largest bond orientational order parameter of 0.7, which is indicative of a relatively ordered phase, as shown in Figure 36B, middle row. In contrast, points C and D

with yield of 1 and 0.93, respectively, have bond orientational order parameter of 0.46 and 0.47, respectively, which is indicative of a relatively disordered phase, as illustrated in Figure 36C and D, middle row. Overall, these results suggest that ordered phases of nanoparticles generally hinder high yields most likely due to energetic barrier for a nanoparticle to move from the bulk to the nanocavity. Figure 36 bottom row shows the liquid film configuration, demonstrating the existence of droplets, which are left behind, and liquid particles (cyan) that are not part of the liquid film. These particles indeed represent the vapor phase, which is modeled by MDPD simulations.

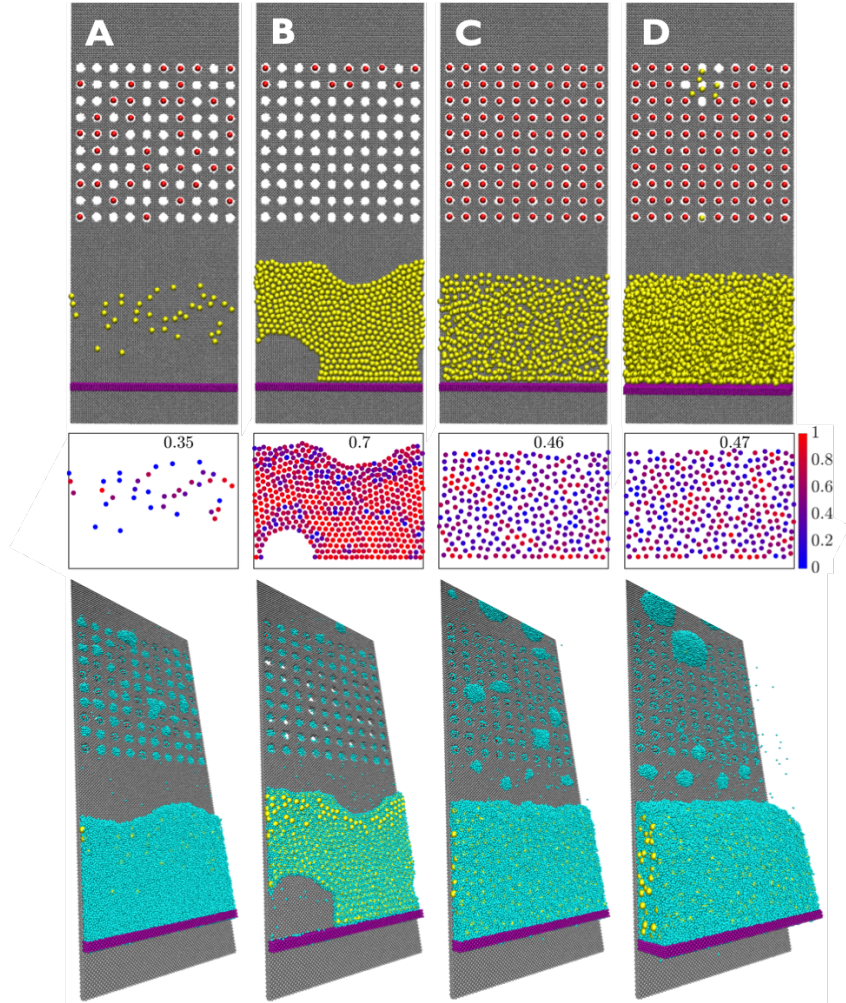


Figure 36: The top view of last snapshot of MDPD simulations corresponding to four different points on the phase diagram in Figure 33 (A-D). Middle row panels illustrate the corresponding orientational order parameters per particle color coded from blue to red, respective of 0 to 1 high. The average particle's 2D bond orientational order parameter is shown at the top of each panel. Bottom row panels depict the 3D view of the same snapshots in the top row, while liquid particles (cyan) are turned on. All particle configurations are obtained at the same MDPD time step in MDPD simulations.

5.3.2.4 Dynamics of the nanoparticles in the confinement

To understand the mechanisms of DSA-n using MDPD simulations, we visualize the trajectory of three nanoparticles from point C on the phase diagram in Figure 33 ($d = 5$, $\rho = 0.07$, and $\text{yield}=1$) that are eventually deposited in the last row of nanocavities in the array of 10×10 (white circular holes). Figure 37A illustrates the top view of these trajectories that are color coded with the time progression, from blue to green, initial to final position, respectively. Liquid particles are turned off for clarity in Figure 37A. In Figure 37A, the red particle indicates the presence of an already deposited nanoparticle while the three targeted nanoparticles are hovering over the nanocavities. We note that these three nanoparticles are all deposited before the receding meniscus reaches to the corresponding nanocavities. These trajectories indicate that sometimes the nanoparticles jump over empty nanocavities without going into them. Random hopping over empty nanocavities is indicative of a random process by which nanoparticles in the liquid confinement are deposited in DSA-n.

To further justify the random hopping mechanism, we visualize the x-, y-, and z-trajectories of the nanoparticles. Figure 37B illustrates the x-trajectory of the nanoparticle marked by a white arrow at the bottom in Figure 37A. In Figure 37B, the gray bands indicate the x-position of nanocavities, the purple dashed line highlights the time at which the piston (purple block) goes over the last row of nanocavities, and the cyan dashed line marks the time at which the receding contact line slides over the designated nanocavity in which the nanoparticle has already been deposited. Figure 37C depicts the y-trajectory of all 100 nanoparticles that are deposited in the simulation that led the yield of 1 for point C on the phase diagram in Figure 33. In

Figure 37C, the blue line illustrates the trajectory of the receding contact line, and the green line shows the trajectory of the nanoparticle highlighted with the white arrow in Figure 37A. From the results in Figure 37C, we determine that 95 nanoparticles are deposited before the receding contact line reaches them, and only 5 nanoparticles are deposited at the same time that the contact line goes over their corresponding nanocavities. The red trajectory in Figure 37C shows the path of one of such nanoparticles.

Figure 37C has an important implication about the mechanisms of DSA-n, suggesting that the major factor is the random hopping in and out of the nanocavity before the receding meniscus reaches there. The current hypothesis in the literature is a DSA-n mechanism via the force that is exerted from the angled receding meniscus on to the nanoparticle, dragging of the nanoparticle, and pushing it into the nanocavity. (52) In the random hopping mechanism however, the receding meniscus does not push the nanoparticle into the nanocavity. In the high nanoparticle density regime, the presence of a nanoparticle monolayer prevents the nanoparticle from coming out of the nanocavity after hopping. After deposition, the angled receding meniscus also lowers the likelihood of the nanoparticle to randomly come out of the nanocavity.

Figure 37D depicts the z -trajectory (displacement perpendicular to the substrate) of the highlighted tracer in Figure 37A. Besides, the horizontal displacement in trajectory for each tracked nanoparticle is at most two layers of cavities that we hypothesize it due to the densely packed nanoparticles within liquid film. The results show random transition between two distinct levels at $z = 1.5$ and $z = 3.0$, indicating the presence of double layers of nanoparticles in the bulk. Once the piston (dashed purple line) goes over the nanocavity, and the nanoparticle

is deposited, the tracer nanoparticle starts randomly transitioning in and out of the nanocavity. This observation further supports the hopping mechanism hypothesis, which is indicative of the hopping mechanism. The horizontal dashed red line represents the templated substrate surface below which the nanoparticle is considered to be trapped in a nanocavity. After the tracer nanoparticle is deposited into the nanocavity, its motion will be stabilized along the x- and y-direction if the nanoparticle does not transition outside the nanocavity, as shown in Figure 37B and C. Figure 37E illustrates the likelihood the marked tracer nanoparticle being in and out of the nanocavity. The likelihood is determined by finding the ratio of the cumulative time during which the tracer nanoparticle stays inside and outside the nanocavity over the sum of the two time spans. The likelihood of being inside or outside the nanocavity can be utilized to determine the Boltzmann weighted factor of the Gibbs free energy contribution to the nanoparticle deposition.

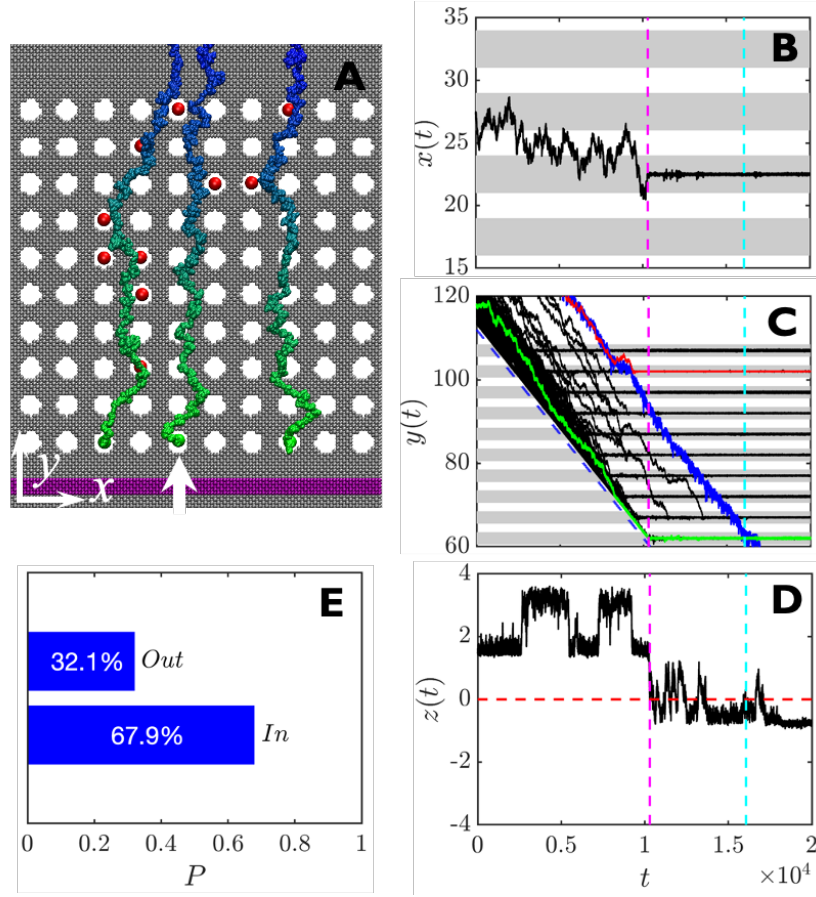


Figure 37: Top view of trajectories of 3 tracer nanoparticless from their initial (blue) to final (green) position over a templated substrate with 10×10 array of circular nanocavities (A). x-trajectory vs. MDPD time for the tracer nanoparticle marked by a white arrow in A, where purple and cyan dashed lines indicate the MDPD time at which the piston and receding contact line goes over the marked nanoparticle deposited in the nanocavity (B). y-trajectories of all 100 nanoparticles involved in the DSA-n, where blue line is trajectory of the receding contact line, green line is trajectory of the marked tracer nanoparticle, and red line is the trajectory of a nanoparticle that is directly self-assembled by the receding interface (C). z-trajectory of the marked tracer nanoparticle where the dashed red line represents the surface of the templated substrate (D). Likelihood of the marked tracer nanoparticle being in and out of the nanocavity.

5.3.2.5 Impact of the local confinement on the yield of DSA-n

We hypothesize that in addition to the liquid film thickness (bulk confinement), the local confinement, which is the confinement developed in the vicinity of the receding contact line, and generated by the angled moving meniscus, improves the yield. To investigate the effect of the local confinement on the yield, we compare the yield from two different MDPD simulations of a receding liquid film, one by pulling the piston (purple block) downward, and the other by placing a hydrophilic flat plate (purple block) on the liquid parallel to the substrate, and pulling the plate downward that is commonly used in DSA-n experiments (52; 53; 41; 31; 54; 195; 205), as shown in Figure 38A and B, respectively. In Figure 38A and B, the first panel from the left on the top row illustrates the top view of a snapshot during the DSA, the middle and right panel in the top row shows the side view with and without the liquid particles (cyan) for clarity. In the latter case, the speed of the contact line, and the templated substrate, liquid, and nanoparticle properties, and liquid film thickness ($d = 5$) are identical to those of the former. The only difference is the driving force, which pulls the liquid film downward. That is the piston in the former, and the plate parallel to the liquid in the latter. From the side views, it is obvious that the contact angle formed by the moving flat plate is larger than that formed by the moving piston. Furthermore, the receding contact line created by the moving piston seems to get strongly pinned by the array of nanocavities, hence large fluctuations in the contact line position as opposed to the relatively straight contact line formed by the moving flat plate.

First, we confirm that the presence of the flat plate in the latter simulation is not affecting the nanoparticle pair interactions compared to those in the former. To ensure identical nanoparticle interactions, we compare the distribution of the nearest neighbor distances between nanoparticles. We calculate the nearest neighbor distance by measuring the center-to-center distance between every pair of nearest neighbors, which are defined by Voronoi diagram. (204) Bottom panels in Figure 38A and B suggest relatively identical distribution of the nearest neighbor distances for two simulations, where dashed blue and red lines are the median and mean of the distributions, respectively. The MDPD simulation results indicate a similar median of 3.3 for both distributions. Despite identical properties, we note very different yields for both simulations, being 0.77 in the former, and 0.24 in the latter.

We conjecture that the large difference in yield is due to the conformation of the contact line and local confinement developed by the receding meniscus. In particular, for a small receding contact angle where piston is pulling the liquid film downward, the space between the angles meniscus and substrate is more confined compared to that formed by downward moving flat plate. As such, already deposited nanoparticles more readily find a way out of the nanocavities at the time the meniscus goes over the nanocavities; hence the likelihood of liberating the trapped nanoparticle increases in the receding liquid film pulled downward by the flat plate. Overall, these results suggest that the extra local confinement at receding meniscus helps improve the yield of DSA-n.

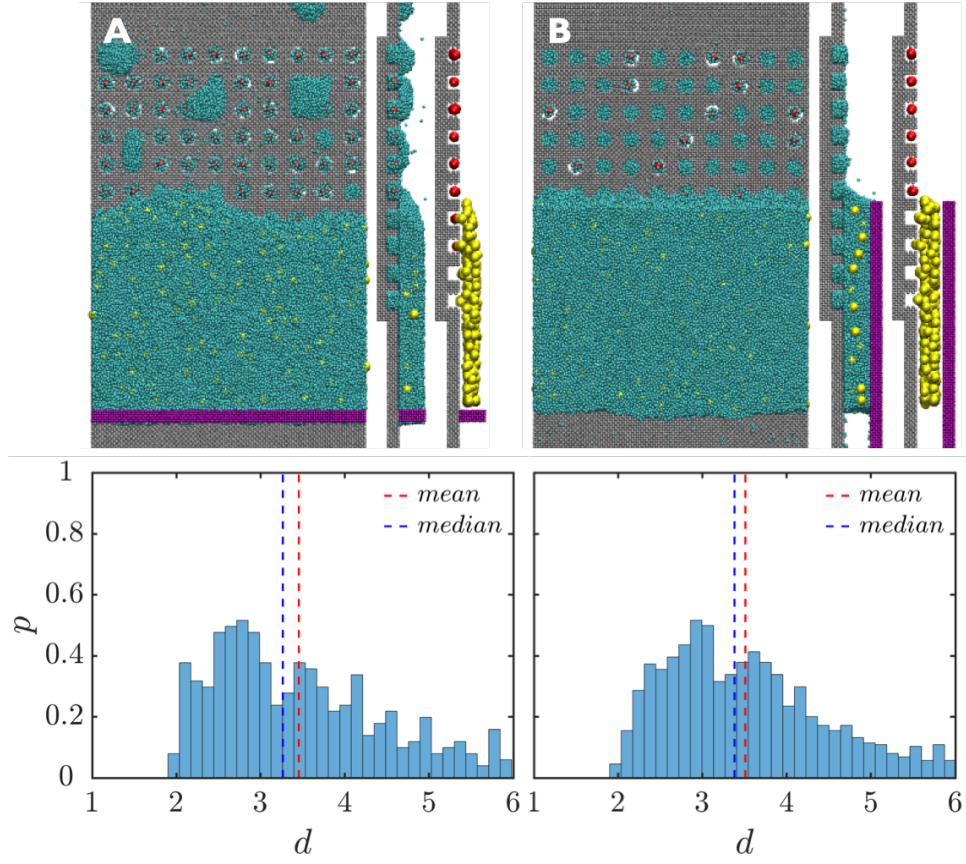


Figure 38: Comparison of the top and side views with the liquid film turned on (blue cyan particles) and off for clarity, and nanoparticle configurations between receding liquid film by moving a piston (A) and a flat plate (B). Panels in the bottom row compares the distribution (blue histogram), mean (red dashed line), and median (blue dashed line) of nearest neighbor distances for the two aforementioned MDPD simulations.

In addition to the contact angle, configuration of the contact line, and the yield, we observe differences in the velocity and vorticity profile in the liquid film for the two aforementioned setups shown in Figure 38. We interpolate the particle velocities to obtain velocity field for the uniform 3D grid points using an inverse multi-quadratic radial basis function (RBF). The RBF-based interpolation method enables us to illustrate the velocity and vorticity profile in xy -plane for the receding film by the piston, and flat plate, as shown in the side views in Figure 39AB and CD, respectively. The instantaneous profiles are shown in Figure 39A and C, and the profiles averaged over 5 independent simulations are illustrated in Figure 39B and D, all at time $t = 12000$ during the MDPD simulations. The black arrows represent the instantaneous velocity field, while the vorticity field is color coded from blue to red, corresponding to low and high, respectively. Solid-liquid and liquid-vapor interfaces are also shown by a red line. The presence of vortices and irregular instantaneous velocity field in Figure 39AC suggest circulations and dominant Brownian motion in the receding liquid film.

In both simulations, the averaged velocity profiles indicate localized flow into the nanocavities, which suggest a mechanism for bringing the nanoparticles into the nanocavities. From the velocity and vorticity profiles, we do not see considerable differences between the two DSA setups, which seem to suggest that the major contributing factor to the large difference in their yield is the receding contact angle, and deformation of the receding contact line by the array of nanocavities. The contact angle in the film pulled by the piston is smaller than that in the film pulled by the flat plate. Furthermore, the contact line in the film pulled by the piston is more pinned and deformed compared to that in the film pulled by the flat plate.

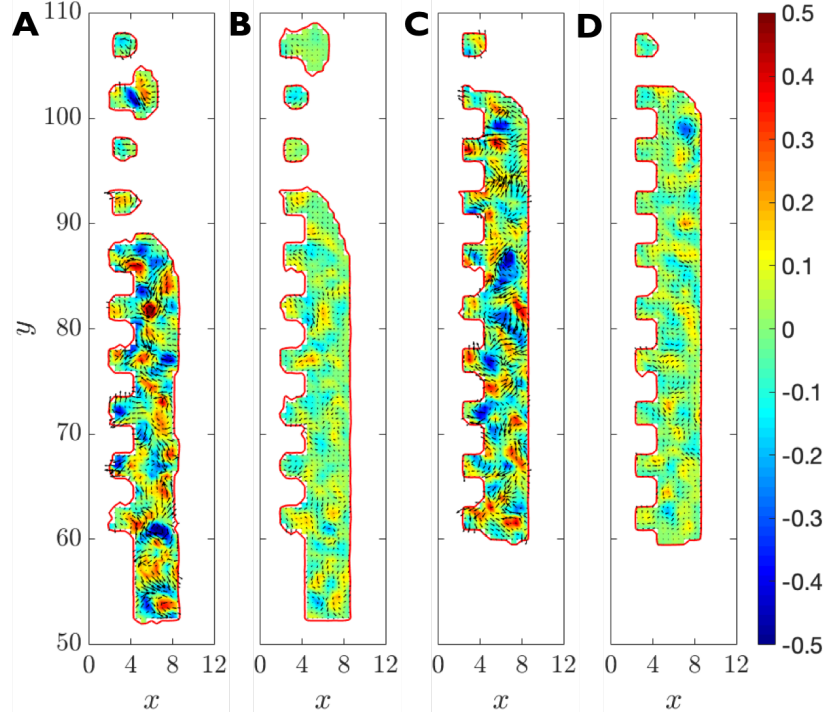


Figure 39: The comparison of velocity and vorticity profile in DSA-n the liquid film pulled by the piston (AB), and a flat plate (CD). Panels A and C represent instantaneous profiles, while panels B and D represent profiles averaged over 5 independent simulations. Red contour line indicates solid-liquid and liquid-vapor interface, arrows show velocity field, and vorticity field is color coded from blue to red, low to high, respectively.

5.3.3 Impact of the template geometry on the yield of DSA-n

Above mentioned results indicate that the template geometry indirectly affecting the yield via modification of the contact angle and deformation of contact line. We hypothesize that the

template geometry can also impact the yield by means of the nanocavities interspacing and their geometry. We will discuss these effect as follows.

5.3.3.1 Impact of the nanocavity interspacing on the yield of DSA-n

We examine the interspacing between the nanocavities by varying their center-to-center distance in both x - and y -direction, and compare the yield of DSA-n. For the sake of comparison, we compare the yield with reference to a simulation with $d = 5$ and $\rho = 0.02$. We particularly chose a reference with low yield to study how the template geometry can improve the yield. We vary the center-to-center distance from 3.5 to 5 with an interval of 0.75. Figure 40 illustrates the top and side views of the liquid film and nanoparticle configurations with center-to-center distance of 3.5 (A), 4.25 (B) and 5 (C), respectively. The left and right panels in Figure 40A-C depict the top view with liquid turned on and off for clarity, respectively. The left panels are snapshots taken during the DSA, and the right panels are those taken once the contact line goes past the bottom line of nanocavities in the array. The two middle panels are the side views with the liquid film turned on and off for clarity, corresponding to the intermediate snapshots shown in the left panels. In these simulations, we keep the cavity radius fixed at 1.5.

The simulation results indicate a continuous decrease in the yield from 0.31 to 0.24 to 0.20 as center-to-center increases from 3.5 to 4.25 to 5, as shown in Figure 40A to C, respectively. From the side views in Figure 40A-C, we also observe an increase in the solid-liquid contact angle with center-to-center distance, which is accompanied by less deformations of the receding contact line. The results corroborates with the previous hypothesis about the role of receding meniscus on the overall yield of DSA-n. In particular, small receding contact angle creates a

local confinement for the nanoparticles that are already trapped in the nanocavities. This local confinement lowers the likelihood of the nanoparticles randomly escaping from the nanocavities; hence, increasing the yield. Overall, the simulation results suggest that decreasing the center-to-center distance provides more pinning, and lowers the contact angle, which increases the local confinement, preventing the nanoparticles from leaving the nanocavities; therefore, rendering an increase in the yield.

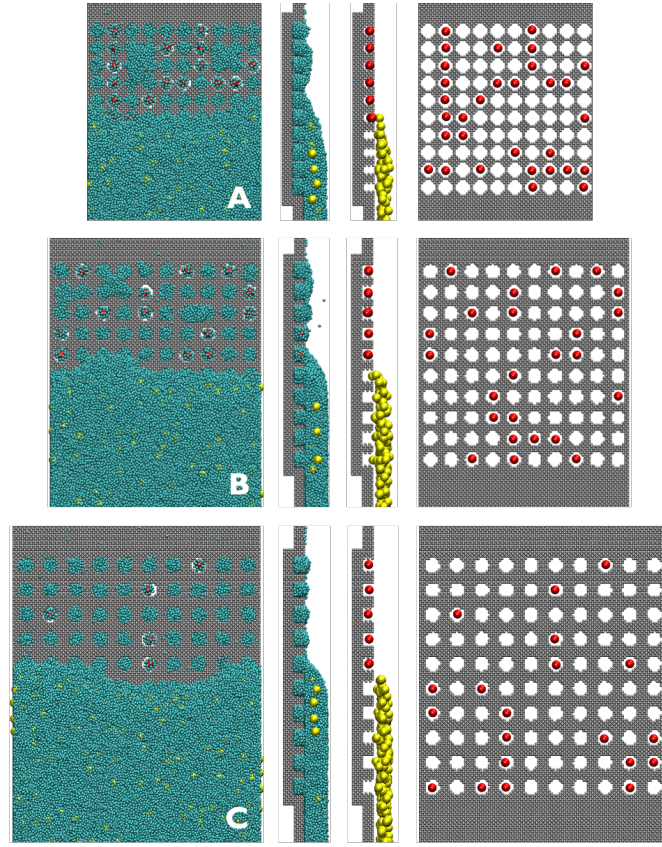


Figure 40: An intermediate (left three panels) and final (right panels) snapshots of MDPD simulations of DSA-n on templated substrate with increasing center-to-center distance between nanocavities from 3.5 (A), to 4.25 (B), and 5 (C). Far left and right panels are the top views with liquid (cyan particles) turned on and off for clarity, respectively. The middle panels are the side views, corresponding to the left panels, with and without the liquid film visualized. All snapshots are taken at the same time point.

5.3.3.2 Impact of the circular nanocavity radius on the yield of DSA-n

We also investigate the extent to which the nanocavity radius, as another form of template geometry modification, impacts the yield. We increase the radius of circular nanocavities in the 10×10 array from 1.5 to 2 with a separation of 0.25, while keeping the center-to-center distance between the nanocavities constant at 5. Above mentioned simulations are performed at constant liquid film thickness of $d = 5$ and nanoparticle density of $\rho = 0.02$. UP TO HERE

Figure 41 illustrates the results taken from the MDPD simulations of the falling liquid film with nanocavity radius of 1.5 (A), 1.75 (B) and 2 (C). The right three panels illustrate the intermediate configuration of the liquid film (cyan particles) and nanoparticles, with gold being suspended nanoparticle in the liquid film, and red being the one that is deposited. The far left panels are the top views and the two middle panels are the side views with the liquid film turned on and off for clarity. The far right panels show the top view of the final configuration with the liquid film turned off for clarity. Results in Figure 41A to C suggest that increasing the nanocavity radius from 1.5 to 1.75 to 2 renders an increase in the yield from 0.18 to 0.59 to 0.70, respectively. Although the change in the contact angle is not considerable, the impact on yield is obvious. The side views with the liquid film turned off indicate that the higher yield in Figure 41C compared to the yield in Figure 41A most likely is due to the increase in the number of deposited nanoparticles before the meniscus get to the nanopartricles.

The side views show that nanoparticles are already trapped in the nanocavities long before the receding contact line reaches there, which agrees with the hopping mechanisms hypothesized earlier in this chapter. The larger nanocavity radius increases the likelihood of nanoparticles

randomly hopping into the nanocavities, since the likelihood is proportional to the nanocavity surface area in the xy -plane. From the side views, it is obvious that the presence of other nanoparticles suspended in the bulk help block those that are already deposited. For small nanocavity radius, there is none trapped between the substrate and the nanoparticles suspended in the bulk above the substrate, as shown in the side view of Figure 41A. As the nanocavity radius increases, the number of trapped nanoparticles increases, which leads to an overall increase in the yield. However, increasing the nanocavity radius beyond a threshold will lead to multiple depositions in a given nanocavity.

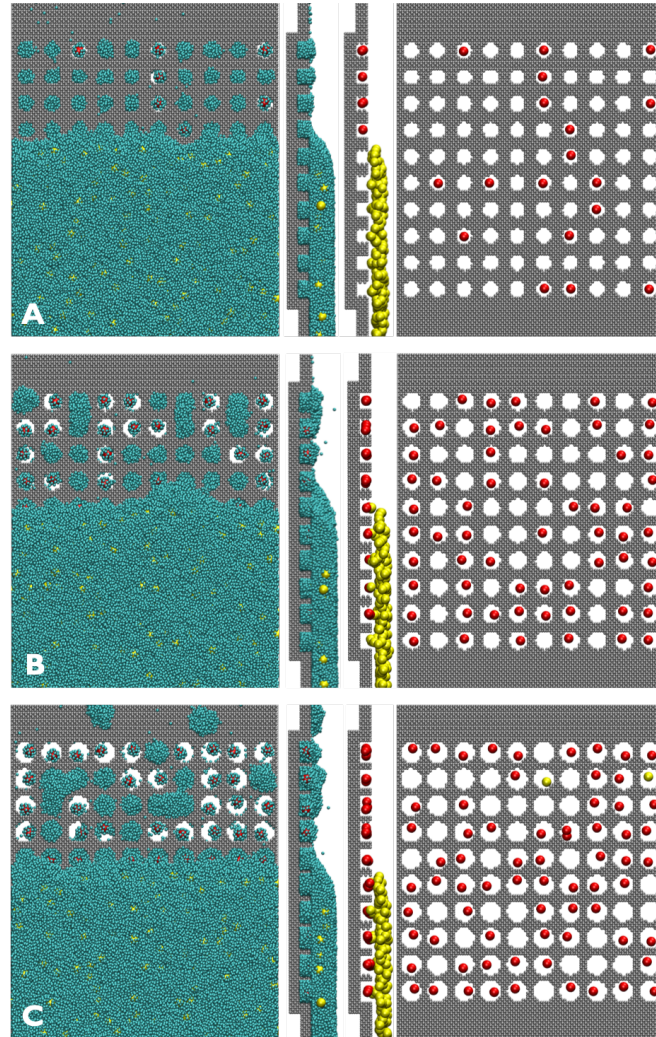


Figure 41: The three left panels show an intermediate snapshot taken from the MDPD simulations, and the right panel was taken when the contact line went past the array. Nanocavity radius increases from 1.5 (A) to 1.75 (B) to 2 (C), the left and right panels show the top views, and the middle two panels illustrate the side views of the far left panel. In the left two panels, liquid film is turned on whereas in the right two panels it is turned off for clarity. All intermediate snapshots were taken at the same time point during the simulations.

5.4 Conclusions

We performed a series of MDPD simulations to unravel the mechanisms of DSA-n, and investigate the factors that improve the yield. From these simulations, we developed the yield phase diagram with two independent variables, the liquid film thickness, commonly known as degree of confinement, and the nanoparticle density. The simulation results indicate that there is an optimum density, where the yield is maximized, regardless of the film thickness. However, at the optimal density, the maximum yield decreases with the film thickness. We found that at low nanoparticle density, DSA-n is entropically prohibitive, and at large density, it is energetically unfavorable.

The trajectories of nanoparticles taken from the simulations suggest a hopping mechanism for DSA-n. According to this mechanism, nanoparticles random hop in and out of nanocavities. At low density, the likelihood of hopping into a nanocavity is low as it is entropically unfavorable. At high density, the likelihood of hopping into a nanocavity is also low since it is energetically unfavorable. In this view, nanoparticle deposition is not driven by the receding liquid-vapor interface, although the interface helps prevent the nanoparticles from hopping out of nanocavities. In this regard, lowering receding contact angle provides a local confinement at the contact line, which increases the yield by not allowing the trapped nanoparticles to transition out of the nanocavities. The major factor in trapping the nanoparticles is the presence of other nanoparticles in the bulk, which creates a shielding layer, blocking the deposited nanoparticles on the way out.

Using these simulations, we also compared the effect of two experimental setups on the yield by generating a receding contact line pulling the film via (1) a piston, and (2) flat plate parallel to the substrate. Given relatively identical velocity profile in both setups, we attributed the difference in the yield to the contact angle, which was found to be larger in the latter; hence, a lower yield. Our simulations also shed some light on the impact of substrate geometry on the yield of DSA-n. In particular, an increase in center-to-center distance of circular nanocavities studied here decreases the yield at least in the range of film thickness and density considered in this work. The driving force is mainly the receding contact angle, which increases with the center-to-center distance between nanocavities in the array; hence, lowering the local confinement, and the yield. Furthermore, an increase in the radius of circular nanocavities increases the yield via increasing the likelihood of nanoparticle hopping into the nanocavities followed by a blockage of its way out.

In this work, we neglected several factors, which may impact the yield. These factors include, the receding contact line velocity, temperature, shape of nanocavities and their arrangement in the array. Further work is warranted to refine these factors, and confirm their influence on the DSA-n mechanism and the overall yield.

CHAPTER 6

FREE ENERGY CONTRIBUTIONS TO TEMPLATE-ASSISTED SELF-ASSEMBLY OF NANOPARTICLES FROM STEERED MOLECULAR DYNAMICS SIMULATIONS

6.1 Introduction

Directed self-assembly of nanoparticles (DSA-n) over a templated surface is a critical technical process for extensive applications in miniaturization of nanodevices, including semiconducting, (178; 179; 180; 41) plasmonic, (37; 17; 176; 177) and photovoltaic devices (49; 48; 181; 32). The pre-designed templated surface is able to selectively capture nanoparticles, induce interaction-based orientation and even organize them into a complex structure using a bottom-up fabrication process. (182; 183; 184; 185; 29; 206; 26) Taking advantage of the great potential in template-assist DSA-n, many studies have utilized a thin liquid film sliding over a templated surface to realize the assembly process, which allows high yield of nanoparticle deposition with specific ordering or alignment. (52; 53; 57; 194; 60; 197) In DSA-n at sub-10 nm, the thin liquid film provides a restriction of long-range molecular interactions from multiple nanoparticle layers, that in turns facilitates the positioning of nanoparticles in DSA-n. (195; 58; 196; 59) Although the fabrication strategy of template-assisted DSA-n is able to achieve ordered arrays of nanoparticles over large areas of the templated surface, the yield of self-assembly is sensitive to the nanoparticle density. This variation of yield at different nanoparticle density indicates

that among other parameters, the density is one of the structural determinants of the efficiency of DSA-n, and plays a key role in the energetics of the complex self-assembly process. In this process, computational modeling has come illustrative to aid with explaining the contributions to the associated free energy.

Calculation of free energy change between two states, in the liquid film and on the templated surface, for a self-assembled nanoparticle will be immensely aided in locating the optimal yield. Various molecular-simulation-based approaches such as probability ratio method (PRM) in molecular dynamics (MD) studies aimed at estimating the free energy were initiated. (207) PRM tracks the positions of neighboring molecules as a function of time, which are transformed into a probability distribution function with respect to the states of tracked nanoparticle. The probability distribution function is then used to calculate the relative free energy. (208; 209; 158) Nevertheless, reports indicate that PRM may suffer from insufficient sampling, in addition to the unreliable estimates of the probability density distribution across the surface. (208) An alternative method to the PRM is the thermodynamic integration (TI) in which the position-dependent potential of mean force, as a representative of free energy, acting on the molecule of interest at different positions is integrated over the distances of constraint forces. (210; 211; 212) Both PRM and TI are equilibrium methods that require the simulation environment to be at equilibrium during the transition of tracked molecule. This means the simulation needs to regain an equilibrium state after each motion of tracked molecule. As such, aforementioned techniques seem not suitable for measuring free energy contributions to the DSA-n, considering

that the process is continuously out of equilibrium. The lengthy equilibration processes can therefore lead to a high computational cost.

Enlightened by the Jarzynski's equality in statistical mechanics, the steered molecular dynamics (SMD) extends the realm of free energy calculation to non-equilibrium simulations at an efficient computational cost. (213; 214; 215) SMD simulations have been widely applied in revealing mechanical process of protein binding, folding and stretching. (216; 217; 218; 219; 220) Recently some studies have also attempted to apply SMD simulations in free energy calculations by employing Jarzynski's equality. (221; 222; 223; 224) Jarzynski's equality is a relation that explains the free energy between two equilibrium states, ΔE_{12} , in terms of the external work done through a non-equilibrium process between above-mentioned two states, W_{12} . (213) The work is obtained from an ensemble of finite-time measurements of external work performed on the system during the transition, i.e.

$$\exp(-\beta\Delta E_{12}) = \langle \exp(-\beta W_{12}) \rangle \quad (6.1)$$

where $\beta = (k_B T)^{-1}$, k_B is the Boltzmann constant, T is the temperature, and $\langle . \rangle$ represents averaging over independent simulations. Applying Jarzynski's equality, SMD simulations enable free energy calculations from non-equilibrium processes. To obtain an accurate estimate of free energy, one needs to collect enough samples as the average of exponential term in Equation Equation 6.1 requires a large number of independent SMD simulations.

The purpose of this chapter is to utilize Jarzynski's equality to calculate the free energy contributions to the DSA-n into templated surfaces from SMD simulations. For SMD simulations, we use many-body dissipative particle dynamics (MDPD) simulations. As coarse-grained molecular dynamics (MD) simulations, MDPD simulations are capable of combining both microscopic and mesoscopic interactions while capturing the properties of fluid interfaces (225; 148) at much larger scales than traditional MD simulations, (129; 130) such as those in evaporation-mediated DSA-n. (202) Without loss of generality, we focus on directed self-assembly of a spherical nanoparticle into a circular nanocavity, which is etched out of a substrate with an otherwise flat surface. The self-assembly is observed in two cases: from (1) a stagnant bulk thin liquid film, and (2) a thin liquid film with flow field and a receding interface to the nanocavity. In the second case, to generate the flow field and receding interface in the thin liquid film, we model a hydrophilic surface with a downward moving piston. The transition of states is induced by attaching one end of a spring to a tracer nanoparticle while pulling the other end towards the nanocavity in the substrate, mimicking the DSA-n. Free energy variation is calculated as a function of pulling distance. All MDPD simulations are performed using LAMMPS package at a constant temperature in a manner that satisfy the Markov property and detailed balance.[ref18] The initial states, which depends on the positions and velocities of the nanoparticles, liquid, and the tracer particle are sampled from the canonical ensemble corresponding to the Hamiltonian of the particle system. We will also discuss the free energy profile, compare the difference in the free energy between stagnant and moving thin liquid film, and highlight the impact of the flow field and the receding interface on the free energy profile at various nanoparticle densities.

6.2 Theoretical Model

6.2.1 MDPD model

We utilize MDPD model, as described in chapter 5.2, to understand the energetics during the DSA-n.

6.2.2 Simulation setup

In current work, we uniformly place frozen particles with fcc configuration to model a vertical solid substrate with a cylindrical cavity (hereafter nanocavity) positioned in the center. On top of substrate surface, we place a thin liquid film by randomly distributing liquid particles, and nanoparticles to cover the nanocavity. We place a piston perpendicular to the substrate to hold the liquid film. The presence of the piston enables us to slide the liquid film over the substrate by controlling the motion of piston. We apply the periodic boundary conditions in the x -direction along the substrate surface throughout the SMD simulations. We performed the SMD simulations by attaching a spring between a fixed end and a tracer nanoparticle, which has the same properties as other nanoparticles in the liquid film. We shrink the spring with a constant rate, v_s , which exerts a continuous pulling force to the tracer nanoparticle, along the $-z$ -direction towards the bottom of the nanocavity. There is no constraints applied on the tracer nanoparticle in the x - and y -direction, so that the motion along these directions are solely dependent on the interactions of the tracer nanoparticle and the surrounding particles. Since one end of the spring is fixed at the center of the nanocavity at $z = 0$, a deposition process induced by compressing the spring is followed. We select a soft spring constant, k_s , such that the tracer nanoparticle is not too constrained in the z -direction. During SMD simulations, we record

the spring force and the position of the tracer nanoparticle, which are used to calculate the external work and free energy contribution using Jarzynski's equality in Equation Equation 6.1.

It is convenient to use nondimensionalized parameters in MDPD simulations; hence we map the simulation parameters into dimensionless quantities with respect to the characteristic units of length, mass, and time obtained from a real liquid. We summarize all simulation parameters in Table Table IV in which the attraction coefficients subscripts l, s, and n stands for liquid, substrate or piston, and nanoparticle, respectively.

TABLE VI: MAPPING BETWEEN DIMENSIONLESS AND DIMENSIONAL SIMULATION PARAMETERS

Description	Symbol	MDPD units	Physical units
Attraction parameter	A_{ll}	-40	-5.84×10^{-10} N
Attraction parameter	A_{sl}	-30	-4.38×10^{-10} N
Attraction parameter	A_{nn}	-300	-4.38×10^{-9} N
Attraction parameter	A_{nl}	-150	-2.19×10^{-9} N
Circular cavity diameter	d_{ca}	5	2.97×10^{-8} m
Circular cavity depth	h_{ca}	2	1.19×10^{-8} m
Piston velocity	v_p	0.005	0.369 m/s
Spring velocity	v_s	0.006	0.369 m/s
Spring constant	k_s	500	1.23 N/m

6.3 Results and Discussion

We are interested in how the free energy of directed self-assembly of a nanoparticle into a nanocavity changes as a function of the nanoparticle z coordinate. This free energy profile is represented as a function of z coordinate of tracer nanoparticle, meanwhile, it is also called the

potential of mean force (PMF) as a function of reaction coordinate. In this section, we discuss an approach to calculate the free energy utilizing the Jarzynski's equality with respect to the aforementioned internal coordinate. In order to apply Jarzynski equality to calculate the free energy change in DSA-n, we model the DSA of a tracer nanoparticle. Using Steered Molecular Dynamics (SMD), we apply a guiding potential to force the tracer nanoparticle to move from a random position in the thin liquid film on the substrate toward the bottom of the nanocavity. We use the following harmonic function for the guiding potential

$$h(z, l_t) = \frac{k}{2}(z - z_0 - l_t)^2, \quad (6.2)$$

where z_0 and l_t are the z -coordinate of the fixed end and the instantaneous equilibrium length of the guiding spring at time t , respectively, and z is the z -coordinate of the tracer nanoparticle, which is attached to the other end of the guiding spring.

6.3.1 Stagnant liquid film

We perform the SMD simulations by moving the guiding potential via changing l_t linearly with rate v_s

$$l_t = l_0 - v_s t, \quad (6.3)$$

where l_0 is the initial equilibrium length of the guiding spring. Following stiff-spring approximation, (218) we find that the tracer nanoparticle closely follows the center of the harmonic

potential, i.e. $z \approx z_0 + l_t$. We then obtain the change in the free energy between state "0" (initial state) and any other state at time "t" from

$$\Delta F = F(l_t) - F(l_0) = -\frac{1}{\beta} \log \langle \exp(-\beta W_{0 \rightarrow t}) \rangle, \quad (6.4)$$

we compute the external work between the two states using

$$W_{0 \rightarrow t} = \sum_{i=1}^n f_{i-1}^z (z_i - z_{i-1}) \quad (6.5)$$

where $W_{0 \rightarrow t}$ is the cumulated work from time "0" to time $t = n\Delta t$, f_i^z is the spring force that is exerted on the tracer nanoparticle within time interval Δt between time step $i - 1$ and i along the z direction, and z_i is the z -coordinate of the tracer nanoparticle at the end of time step i . Using MDPD simulations, we model a thin liquid film of thickness 3, containing suspended sub-10 nm particles of diameter 1.5 while covering a hydrophilic flat surface with a cylindrical nanocavity whose base diameter and height are 3 and 2, respectively, all in MDPD units (see Table Table IV for unit conversion).

To further investigate the impact of density of nanoparticles in the liquid film on the free energy, we look at various nanoparticle density ranging from 0 to 0.1 with an interval of 0.02. We equilibrate the liquid film and nanoparticles before we start the SMD simulations. Once equilibration is complete, the tracer nanoparticle is placed in the thin liquid film. The x - and y -position of the tracer nanoparticle is randomly chosen to be within a square box of 5×5 centered at the nanocavity center in xy -plane, while we set its z -position to be $z = 5.5$. Selection of

the aforementioned square box for random placement of the tracer nanoparticle is based on a DSA-n into an array of nanocavities in the reported experiments. (197; 58; 60) Considering the center-to-center distance of neighboring nanocavities in the grid to be 5, we assume the repeat unit for the grid will be the square box from where deposition starts. Once again, we equilibrate the system under constant temperature, this time in the presence of the tracer nanoparticle. We note that if the tracer nanoparticle is pulled from somewhere outside the square box after equilibration, the associated external work will be very large. To avoid large variations in calculating the average external work in SMD simulations, we discard initial conditions where the tracer starts outside the square box mentioned above after the equilibration stage.

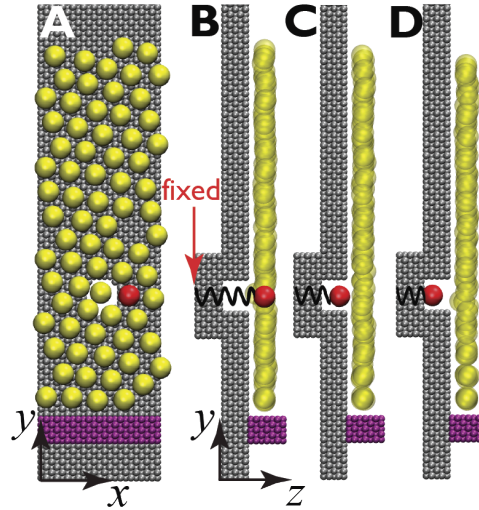


Figure 42: (A) The top view of the liquid film (not shown for clarity) over a templated surface (gray) with a nanocavity (white circle), gold nanoparticles (yellow), and the tracer nanoparticle (red), used as the initial condition for the SMD simulation. (B-C) The side views, illustrating the progression of the SMD simulation, where the tracer is guided from the bulk liquid to the bottom of the nanocavity, respectively, by contraction of the black spring while the liquid film is stagnant.

Figure 42 illustrates the schematics of the SMD model and the way the tracer is guided in DSA-n for a particular nanoparticle density of $\rho = 0.08$. In order to control the thickness of the liquid film, prevent it from further spreading, and keep the thin liquid film stagnant, we have provided a hydrophilic wall, which is shown by the purple block in Figure 42. Figure 42A shows the top view of the initial setup where the tracer (red particle) is off the center of the nanocavity (white hole in the substrate). At nanoparticle density of $\rho = 0.08$, we observe nearly hexagonal lattice formation of nanoparticles (yellow particles) in the bulk liquid (not shown for clarity). Figure 42B-D illustrate the side views of the progression of SMD simulation in that order as the tracer is pulled by the black spring towards the nanocavity. The guiding spring has one end fixed at $z = 0$, while the other end moves toward the bottom of the nanocavity. We perform this guiding by progressively reducing the equilibrium length of the spring, l_t , with the rate of v_s , as shown in Equation Equation 6.3. As the SMD simulation proceeds, the spring steadily pulls the tracer nanoparticle in $-z$ direction, while the liquid film constantly covers the nanocavity, depicted in Figure 42B-D. We then measure the spring force and the tracer displacement in every time step of the simulation from which we calculate the external work in Equation Equation 6.5 to directly self-assemble the tracer into the nanocavity.

To calculate the free energy by averaging the external work in Equation Equation 6.4, we sample 100 trajectories for each of the 6 nanoparticle densities considered in this work. During the SMD simulations and particularly at high nanoparticle density, we sometimes observe competition between the tracer and another nanoparticle to enter the nanocavity. The simulations indicate much larger work for cases where two nanoparticles are directly self-assembled

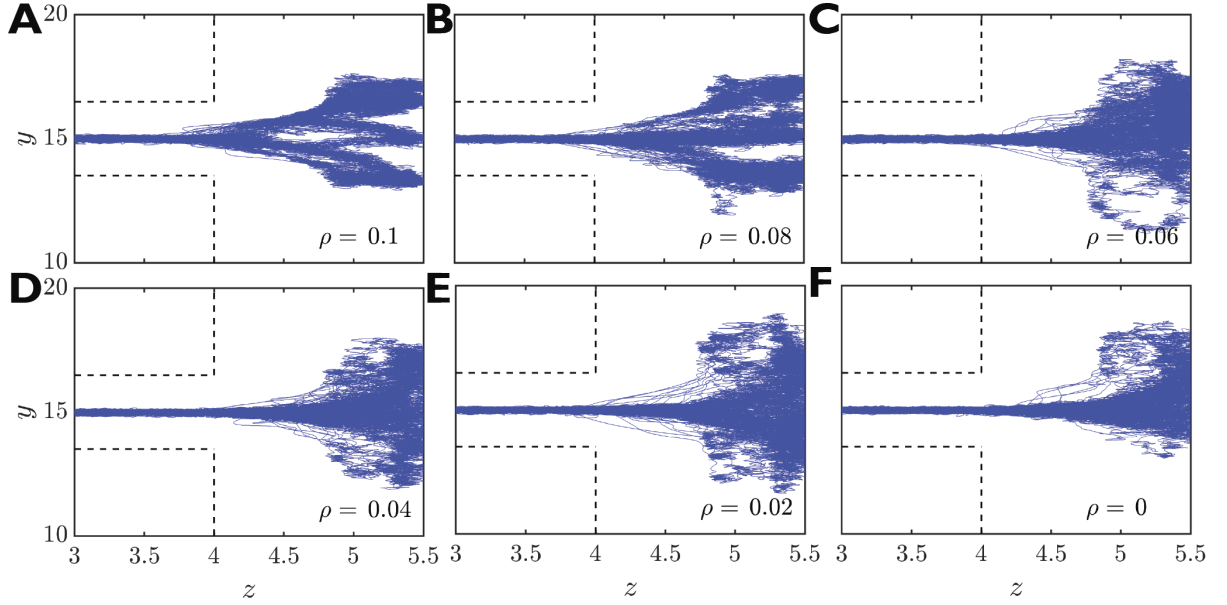


Figure 43: The side view of 100 independent trajectories of the tracer nanoparticle in the yz -plane during the SMD simulations. The dashed line indicates the substrate and nanocavity surface. The nanoparticle density decreases from 0.1 to 0, from A to F, respectively.

into a nanocavity. In this work, we exclude such cases. Figure 43 depicts the side view of all trajectories of the tracer nanoparticle during the SMD simulations, where liquid particles and nanoparticles are not shown for clarity. The pulling process starts where the tracer is approximately at $z = 5.5$, and stops where the tracer reaches $z = 3$, while the bottom of the nanocavity is at $z = 2$. Limiting the z -coordinate for the starting point is to ensure that all trajectories start approximately within the nanoparticle layer, as shown in Figure 42B, where the nanoparticle density is large. Dashed lines in Figure 43 represent the substrate and nanocavity

surface. We vary the nanoparticle density from 0.1 to 0, with an interval of 0.02, as shown in Figure 43A to F, respectively.

The results in Figure 43 suggest that all trajectories are bundled about the axis of symmetry of the nanocavity. This is mainly due to the balancing forces from the surface of the nanocavity in every direction within the xy -plane. We also observe that at high nanoparticle density, the trajectories are localized at the starting point ($z = 5.5$), which is indicative of a lattice formation, as shown in Figure 43A and B. A top view of the lattice ensure that the lattice has hexagonal configuration, as illustrated in Figure 42A for nanoparticle density of $\rho = 0.08$. However, as the nanoparticle density decreases, the trajectories are delocalized at the starting point, which suggests a disordered configuration of nanoparticles in the thin liquid film. At low densities, it is likely that the tracer starts from any point within the square box of initial positions, whereas at high densities, the tracer is bound to start from a point on the hexagonal lattice of nanoparticles; hence has less freedom of random motion.

The top view of the initial positions of all trajectories are color coded from red to blue, respective to nanoparticle density of $\rho = 0.1$ to 0, as shown in Figure 44A. In Figure 44A, the pink circle illustrates the position of the nanocavity, and the black square represents the area, where the initial position of the trajectories are located. For each of these trajectories, we calculate the work of the spring done on the tracer (W) using Equation Equation 6.5. Figure 44B shows the variation of the work against the z -coordinate of the tracer as it is pulled towards the bottom of the nanocavity averaged over 100 trajectories showed in Figure 43. The

averaged work values are color coded from red to blue, corresponding to the nanoparticle density of $\rho = 0.1$ to 0, as shown in Figure 44B.

The results in Figure 44B suggest that the work is directly correlated with the nanoparticle density such that the work needed to move the tracer from $z = 5.5$ to any given z -coordinate increases with the nanoparticle density. This trend can be explained by considering that at large nanoparticle density, the tracer is bound by several other nanoparticles. The attraction between two nanoparticles is more favorable than that between a nanoparticle and a liquid particles. As the nanoparticle density increases, the energetic barrier to move the tracer from a position surrounded by other nanoparticles to the liquid phase increases as the tracer should break some favorable interactions with other nanoparticles, and make less favorable interactions with liquid phase surrounding it. Consequently, the overall work to overcome this energetic barrier increases.

The results in Figure 44B also indicates that the work generally increases as the tracer is pulled towards the bottom of the nanocavity, i.e. as the z -position of the tracer is lowered from 5.5 to 3. Although above observation seems right at low nanoparticle density as shown in Figure 44B, we observe monotonicity of the averaged work with the tracer z -position at large nanoparticle density ($\rho \geq 0.08$). The monotonic increase of the averaged work with the tracer z -position is mainly due to the increased repulsion with the nanoparticle density. Once the tracer goes over the energetic barrier at $z = 4.2$ and $\rho = 0.01$ for example, the steric repulsion of other nanoparticles prevents the tracer from returning back to the bulk phase at $z = 5.5$. Once the tracer comes closer to the bottom of the nanocavity, the surface repulsion increases;

hence, the averaged work rises more rapidly at $z = 3.25$, and with further lowering of the z -position of the tracer.

Using the averaged work in Figure 44B, we calculate the free energy contribution to the DSA of the tracer from Jarzynski's equality in Equation Equation 6.5. The variation of the free energy with the z -position of the tracer is illustrated in Figure 44C, from red to blue, corresponding to the nanoparticle density of $\rho = 0.1$ to 0, respectively. The results in Figure 44C suggest that the smallest free energy contribution occurs at $\rho = 0.08$. Contrary to expectation, the free energy does not decrease with the density. Indeed, a closer look at the free energy variations in Figure 44C reveals that the free energy generally decreases with nanoparticle density up to $\rho = 0.08$ after which the free energy increases. As the density of nanoparticles increases in the bulk, it is entropically more favorable for some nanoparticles to move below the liquid surface, and towards the nanocavity, where the local density of nanoparticles is 0. However, at high density, it is energetically more favorable for the tracer to stay within the ordered phase of nanoparticles as favorable attraction between nanoparticles lowers the free energy of the tracer, which leads to an increase in the free energy of DSA.

Our results in Figure 42A show that nanoparticles form a lattice with coordination number of about 6 (indicative of a hexagonal lattice) at such high density. At density of $\rho = 0.08$, the change in the free energy is around 0 while the tracer moves from $z = 5.5$ to $z = 3.5$. Below $z = 3.5$, the repulsion from the bottom surface of the nanocavity becomes the dominant force, and increases the free energy contribution. Any further movement of the tracer to positions lower than $z = 3.5$ requires positive change in the free energy, regardless of the nanoparticle

density. According to the results in Figure 44C, at the density of $\rho = 0.08$, almost $25kT$ is required to directly self-assemble a nanoparticle from $z = 5.5$ in the bulk into a circular nanocavity with radius $2R$ at $z = 3.0$, where R is nanoparticle radius. Further pulling the tracer below $z = 3.0$ (not shown in Figure 44C) will lead to free energy change larger than $25kT$.

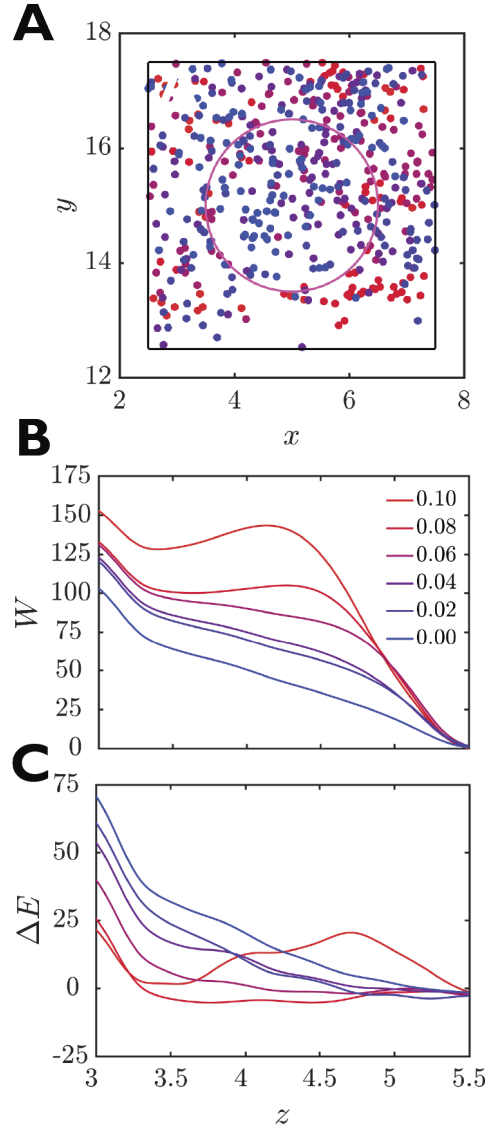


Figure 44: (A) Top view of the starting point of SMD simulations, where initial positions of the tracer nanoparticle are located in the black square in xy -plane, color coded from red to blue, corresponding to densities $\rho = 0.1$ to 0 with the interval of 0.02, respectively. The pink circle represents the top view of the circular nanocavity. (B) The external work done on the tracer to move it from $z = 5.5$ to $z = 3.0$ averaged over 100 independent trajectories with initial positions in A for the 6 different densities. Legend indicates the nanoparticle densities. (C) The change in free energy calculated from Jarzynski's equality in Equation Equation 6.5 color coded for the 6 different densities. The work and change in the free energy are nondimensionalized by kT .

Unlike the average work which is easily affected by trajectories with large work accumulation, the free energy calculation favors the paths with least accumulated work. The Jarzynski's equality considers all valid trajectories from initial position of the nanoparticle to the cavity. These trajectories include ones which start from the corners of square in Figure 44A, and may have the longest traveling distance. The tracer may strongly interact with the substrate surface multiple times along these trajectories. Such situations all contribute in excessive accumulation of work during SMD process that is not favored by exponential average in free energy calculation. In other words, the tracer nanoparticle will accumulate small amount of work from a trajectory such as the one starting right above the nanocavity. This trajectory will take more weights while the average free energy is calculated. Scanning over the nanoparticle density spectrum, Figure 44C suggests an optimum density that is able to achieve the lowest free energy during the nanoparticle self-assembly. For any density lower or higher than $\rho = 0.08$, a higher free energy is required based on Jarzynski's equality in Equation Equation 6.1. Our results suggest that the nanoparticle distribution at $\rho = 0.08$ provides more opportunities of nanoparticle to settle in the nanocavity while there is not much restraining force from the ordered hexagonal arrangement of nanoparticles in the bulk. Based on these results, it should be possible to achieve a high yield in DSA-n by preparing the system at the optimum nanoparticle density.

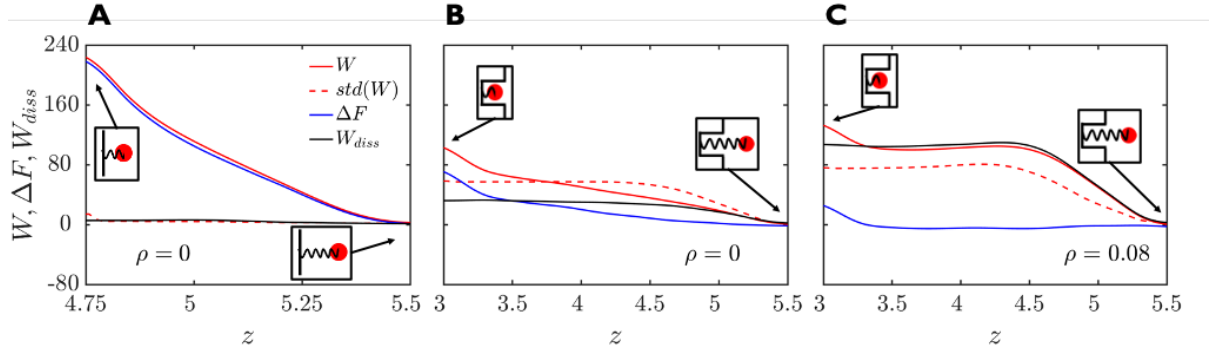


Figure 45: The average work, W , free energy change, ΔE , fluctuations in the work, $std(W)$, and energy dissipation profile, W_{diss} for the tracer nanoparticle in the absence of other nanoparticles in SMD simulation with a flat surface (A), in the presence of a nanocavity (B), and in the presence of a nanocavity and other nanoparticles with $\rho = 0.08$ (C). The results were obtained over 100 independent simulations.

We take one step further, and compare the energy profile generated by different SMD simulation setups, including deposition of a tracer nanoparticle on a flat substrate in the absence of other nanoparticles ($\rho = 0$) shown in Figure 45A, in the presence of a nanocavity with $\rho = 0$ shown in Figure 45B, and $\rho = 0.08$ depicted in Figure 45C.

We present the results of the work and its standard deviation, free energy, and energy dissipation (the difference between the work and free energy) in Figure 44, averaged over 100 independent simulations. The results for self-assembly with a flat surface in Figure 44A is

independent of the tracer's initial position; hence the work and free energy are overlapping with inconsiderable work standard deviation, and energy dissipation. Once the nanocavity is added, the initial position and trajectory in SMD process becomes important. Trajectories starting from corners of the sampling square area differ from those starting from above the cavity in accumulated work. The distinction is reflected in the relatively larger work fluctuations, as shown in Figure 45B and Figure 45C. The work fluctuation is even larger for $\rho = 0.08$ as the densely packed nanoparticles yield trajectories with accumulated work either larger or smaller than the trajectories at $\rho = 0$.

6.3.2 Receding liquid film

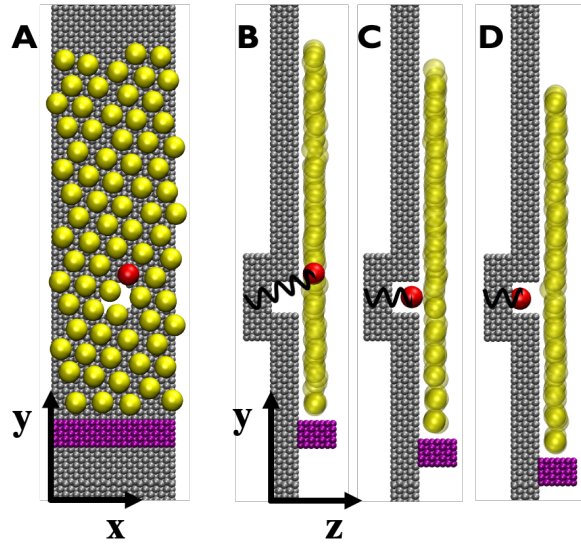


Figure 46: Panel A presents a top view of liquid film over a templated surface with a nanocavity as the initial condition of the SMD simulations. Side view of a SMD simulation at 3 stages (B to D) shows the progression of a tracer nanoparticle deposition guided by a SMD spring (black) while the liquid film is receding downward.

To account for the effect of the receding liquid film, we now look at SMD simulations where $\rho = 0.08$. The results are shown in Figure 46, where the piston (purple block) moves down, and pulls the liquid film with it over the templated surface at a constant velocity during SMD process. Figure 46A is the top view of the initial condition after equilibration in which a nanoparticle layer has formed above the nanocavity. The layer demonstrates a hexagonal nanoparticle configuration where the tracer nanoparticle is located above the upper right edge of nanocavity, as shown in Figure 46A. As the simulation proceeds, the spring steadily pulls the tracer nanoparticle in negative z -direction while the liquid film continuously slides over the substrate as shown in Figure 46C and D. The motion of liquid film helps displace the tracer nanoparticle above the nanocavity while the spring attached to the tracer nanoparticle pulls it downward. Along this trajectory, the tracer nanoparticle interacts with the surrounding including nearby particles.

To calculate the free energy using the Jarzynski's equality in Equation Equation 6.1, we sample over 100 trajectories of the tracer nanoparticle in SMD simulations as shown in Figure 47. The trajectories are shown in yz -plane for nanoparticle density varying from 0.1 to 0. The dash lines represents the surface of substrate and the wall of the nanocavity. The results suggest that the trajectories within the nanocavity are bundled, and centered due to the balancing forces from the surrounding walls. In these simulations, we elevated the initial position of the tracer in the y -direction to offset the downward motion of the liquid film at a later time. The results also indicate that the receding liquid film displaces the tracer nanoparticle further when it is

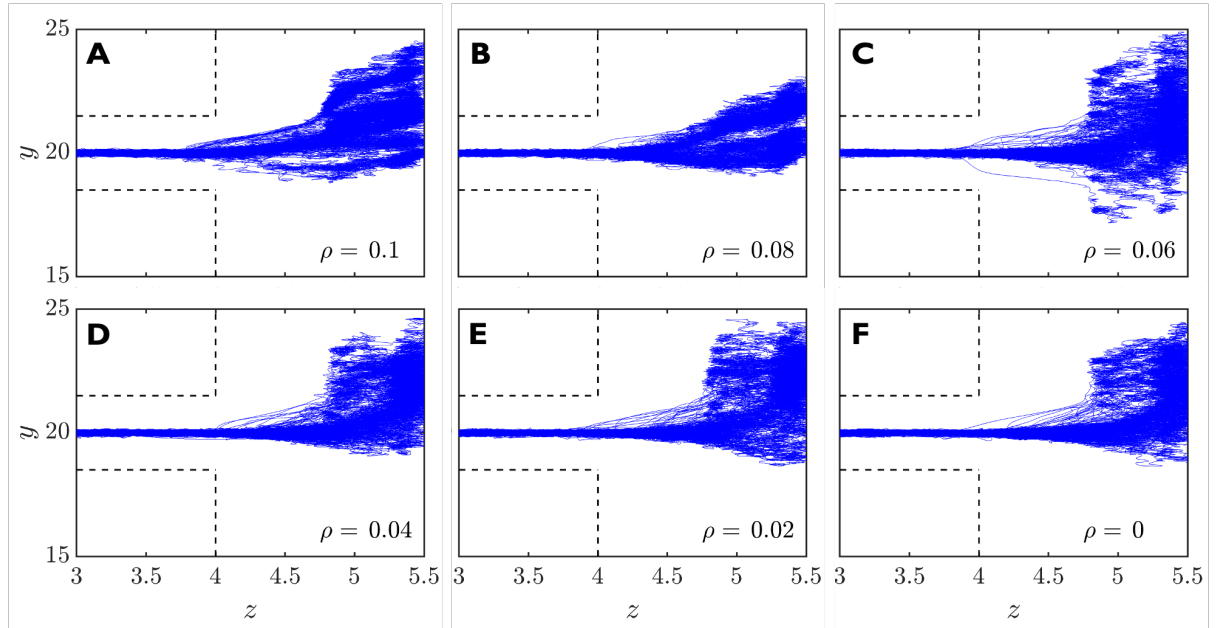


Figure 47: The trajectories of a tracer nanoparticle in the yz -plane, obtained from 100 independent SMD simulations. Nanoparticle density, ρ varies from 0.1 (A) to 0 (F).

being pulled by SMD spring. Although most trajectories of the tracer start from the region above the center of the nanocavity, they demonstrate random distribution before convergence.

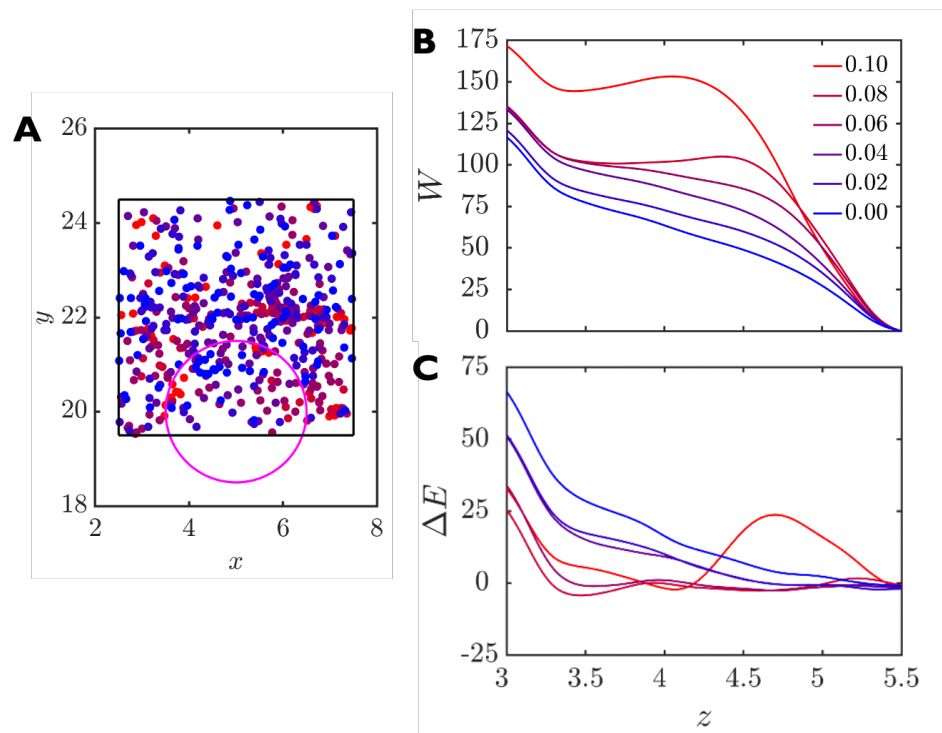


Figure 48: The initial positions of a tracer nanoparticle in xy -plane (A), average work (B), and the free energy change (C), averaged over 100 independent SMD simulations for each density. Red to blue corresponds to the density of nanoparticles ranging from 0.1 to 0.

Figure 48A presents the initial positions of the tracer nanoparticle for densities ranging from 0.1 to 0, showing a random distribution of initial conditions. The inner black square defines the boundary of initial conditions after equilibration, and the purple circle represents the top view of the nanocavity. The average work (W) and free energy change (ΔE) obtained from 100 independent simulations share findings similar to the ones with stagnant liquid film, illustrated

in in Figure 44. The increase of nanoparticle density leads to an increase of average accumulated work. The work for higher densities shows a sharp rise (Figure 48B) before the tracer leaves the cutoff distance of attraction from other nanoparticles in the bulk. Figure 48C also demonstrates the same optimum density at $\rho = 0.08$. This is the density associated with the lowest free energy change during the SMD simulation, independent of the liquid film motion. The results suggest that the receding liquid film increases the overall work by $20 - 25$ kT compared to the case where the liquid was not receding, while it does not considerably change the free energy, We hypothesize that the motion of nanoparticles within liquid film generate more collision with the tracer nanoparticle along the path, which renders higher work necessary to deposit a nanoparticle into the nanocavity. Despite the increased work in the nanoparticle deposition observed in the receding liquid film, it has the advantage of bringing more nanoparticles to the vicinity of the nanocavity, which help promote up-concentration of nanoparticles over the nanocavity. This is rather crucial in application of DSA-n.

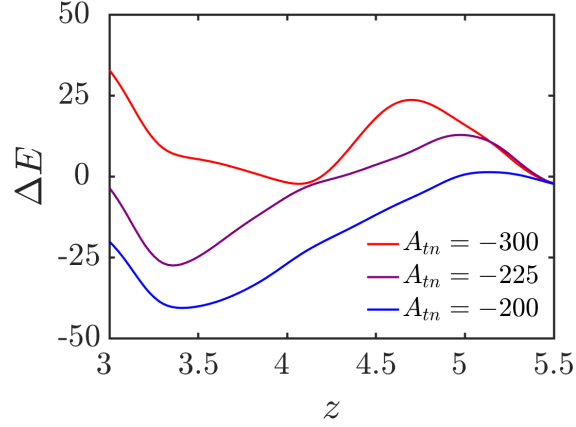


Figure 49: Comparison of the free energy change in SMD simulations for $\rho = 0.1$ and different attraction strength between the tracer and other nanoparticles.

Both the free energy comparison across densities in Figure 44C and Figure 48C demonstrate a barrier within the cutoff distance of 1 unit from the nanoparticle layer in the bulk, especially at $\rho = 0.08$. To confirm that the energetic barriers in the accumulated work at large nanoparticle densities ($\rho = 0.08$ and 0.1), and particularly in free energy at large density ($\rho = 0.1$), as shown in Figure 44B and C, is due to the attraction between the tracer and other nanoparticles, we vary this attraction. At $\rho = 0.1$, we lower the attraction between the tracer and other nanoparticles, A_{tn} , systematically from -300 , which is the same as attraction between other nanoparticles (A_{nn}), to -200 . Figure 49 illustrates the free energy comparison with decreasing attraction parameter (in absolute value, $|A_{tn}|$), averaged over 100 independent simulations. By reducing the attraction between the tracer and other nanoparticles, we observe a decrease

in the energetic barrier within the cutoff distance from other nanoparticles in the bulk. As such, it is energetically easier for the tracer particle to leave the ordered phase with hexagonal arrangement of nanoparticles in the bulk. Note that the decrease in the energetic barrier is not proportional to the that in A_{tn} , as shown in Figure 49. These results suggest that reducing the attraction (A_{tn}) between nanoparticles could be a possible way to lower the overall potential free energy barrier, and subsequently increase the yield in the directed self-assembly of nanoparticles at high densities.

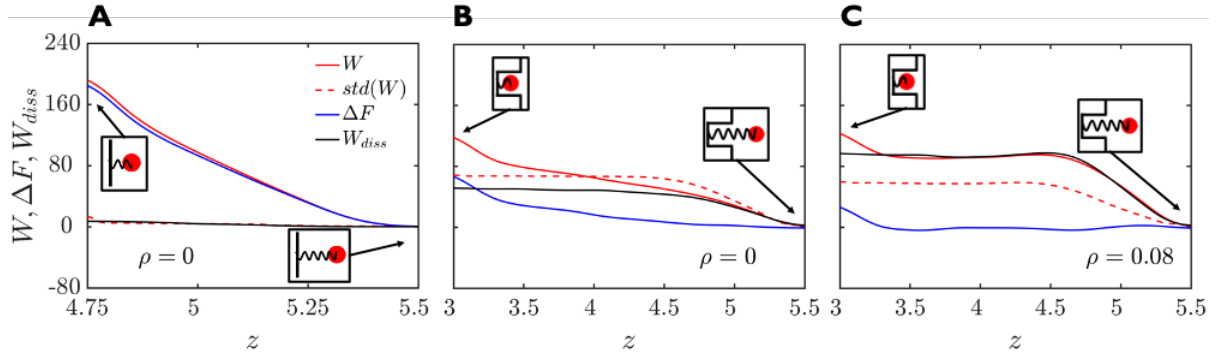


Figure 50: The work and its fluctuation, W and $std(W)$, respectively, free energy change, ΔE , and energy dissipation profile, W_{diss} for the tracer nanoparticle during deposition on a flat substrate in the absence of bulk nanoparticles (A), deposition on a templated substrate with nanocavity at $\rho = 0$ (B), and $\rho = 0.08$ (C). The results are averaged over 100 independent SMD simulations, where the liquid film is receding from top to the bottom.

We also compare the work and free energy profile from SMD simulations, shown in Figure 50, where the liquid film is receding, with those from simulations where the liquid film is stagnant, illustrated in Figure 45. We do not observe conceivable difference between the work and free energy profile from SMD simulations where a tracer nanoparticle is deposited on a flat surface in the absence of other nanoparticles ($\rho = 0$, Figure 50A), on a templated surface in the presence of a nanocavity with $\rho = 0$ (Figure 50B), and on a templated surface in the presence of other nanocavities $\rho = 0.08$ (Figure 50C). Similarity of the results shown in Figure 45 and Figure 50 suggest that receding liquid film does not impact the free energy contribution to the deposition of a nanoparticle on flat or templated substrates.

6.4 Conclusions

We have used Jarzynski's equality along with SMD simulations to measure the work, and free energy contribution to the self-assembly of a nanoparticle into a single nanocavity on an otherwise flat surface. For self-assembly of the nanoparticle on flat and templated surfaces, we took into account the effect of receding liquid film and nanoparticle density in the bulk. The SMD simulation results generally suggest that the work that is required to deposit a nanoparticle in a nanocavity increases with the nanoparticle density. The increase in the work is mainly due to the favorable interaction between the target and other nanoparticles in the bulk. Such interaction increases with nanoparticle densities, so does the work for the self-assembly of the nanoparticle. However, the free energy obtained from Jarzynski's equality does not show a monotonic increase with the nanoparticle density.

Our results indicate an optimum density of $\rho = 0.08$ in MDPD non-dimensionalized units at which the free energy contribution to the self-assembly process is minimum. We attribute the optimum free energy to the competition from the associated entropy and internal energy of the system. In particular, at low nanoparticle density, it is entropically more favorable for the nanoparticle to stay in the disordered phase of nanoparticles in the bulk. However, at high nanoparticle density, it is energetically more favorable for the nanoparticle to stay in the ordered phase of nanoparticles in the bulk. The simulation results indicate that the optimal entropy and internal energy is achieved at intermediate range of densities. We also measured the external work and free energy contribution to the self-assembly of the nanoparticle in two different settings, where the liquid film is stagnant, and in the presence of a receding liquid film. The results from SMD simulations in both cases suggests that the impact of the receding liquid film on the work and free energy contribution is minimal.

In this work, we neglected several factors, including liquid film confinement (thickness), speed of the receding contact angle, and nanocavity shape and size among others. More work is warranted to consider these effects, which will be investigated in a separate work elsewhere.

CHAPTER 7

FUTURE DIRECTIONS

The models that we have developed in this work can be readily generalized to assist with predictions and understanding of experimental observations. These predictions can also be verified by comparison with experimental measurements. We briefly review how these models can be generalized, and propose experimental settings to verify the model predictions.

The KMC model that we developed in chapter 2 is used to predict the dynamics of an advancing precursor film on a substrate. The model can be generalized for various liquids, substrates, and operational conditions. Various liquids can be considered by modifying the tunable surface tension in Equation 2.5 and liquid density in Equation 2.2. Different surface properties can be considered via van der Waals interaction of liquid particles with the substrate, which is characterized by the Hamaker constant in Equation 2.4. Various operational conditions can also be taken into account using different gravitational acceleration and temperature in Equation 2.1 and Equation 2.2, respectively. It is important to note that one can tune the gravitational acceleration experimentally using a centrifugal adhesion balance equipment developed by Tadmor *et al.* (98; 99)

The MDPD model that we developed in chapter 3 to predict the dynamics of a rising three-phase contact line along a vertical substrate can also be used for various liquids with different substrate surface properties. As far as liquid properties are concerned, one can utilize the model for various liquid density, surface tension, and viscosity. These properties can be tuned in

Equation 3.9. The substrate surface properties such as surface roughness and hydrophilicity can be adjusted by varying the surface undulation, which is nondimensionalized by the attraction cutoff distance, and attraction parameter between liquid and substrate particles in Equation 3.2, respectively. The attraction parameter should be adjusted in such a way that the contact angle agrees with the experimental measurements. We showed the variation of contact angle with the liquid-substrate attraction parameter in Figure 12. Temperature as an operational condition can also be taken into account using the Boltzmann constant in Equation 3.6.

We employed the same MDPD model we developed in chapter 3 to gain better understanding of the impact of the nanocavity geometry on the dynamics of a receding contact line pinned at the nanocavity in chapter 4. Subsequently, the liquid and surface properties, and operational conditions can be generalized in the same way as discussed above. In addition, the liquid film thickness, and receding contact line velocity can be adjusted to the need according to the experimental conditions. The liquid film thickness can be enforced by setting the distance of the ghost wall from the substrate. The speed of the receding contact line is tunable by setting a desired piston velocity.

The MDPD model that we develop to investigate the mechanisms, yield phase diagram, and energetics of DSA-n, which were discussed in chapter 5 and 6, respectively, takes the liquid (solvent), substrate, and nanoparticle properties as model parameters. These model parameters include the liquid properties, as discussed in chapter 3, operational conditions as explained in chapter 4, and particle pair-potentials. Although in the current work the mapping of dimensionalizing parameters (length, mass, and time) are set using hexane for the solvent via

Equation 3.9, the MDPD model parameters are also generalizable to match the property of any other solvent used in the experiment. (129) The particle pair-potentials can also be modified to take into account those properties of the liquid that affect the nanoparticle and substrate interactions, such as the solvent dielectric constant. In this work, we considered nanoparticles are covered by positively charge oleylamine ligands as treated in the experiments. (58; 60) The template was fabricated on silicon substrate, which is covered by Hydrogen Silsesquioxane (HSQ), (58; 60) i.e. the nanocavity walls and bottom surface are all HSQ. We adjusted the liquid, nanoparticle, and substrate interactions by changing the attraction and repulsion strength in Equation 3.2 to match the nanoparticle-nanoparticle, and nanoparticle-substrate interspacing as seen in the experiments. (58; 60) Modification of MDPD to account for electrostatic interactions has also been reported, (?) which can be used to further generalize the model application to other experimental settings.

To verify the predictions of the MDPD model, which was used to understand the dynamics of DSA-n in chapter 5 and 6, one can compare the overall yield and mechanisms of DSA-n with those from experiments. As far as the mechanisms are concerned, the likelihood of a tracer nanoparticle staying in or out of the nanocavity can be measured by the liquid-phase transmission electron microscopy, which also provides the opportunity to verify the occurrence of random hoppings ahead of the receding contact line.

The MDPD model developed for template-assisted DSA-n at sub-10 nm scale provides an opportunity to study parametric relation between the yield and underlying driving factors; hence, improve the yield, lower the self-assembly defects, and increase its scalability. Further-

more, the proposed mechanism in DSA-n can be utilized to help design the experiments when it comes to optimization of the self-assembly outcomes, and choosing the right operational parameters.

In chapter 5, we found that confinement and optimal nanoparticle concentration have a positive impact on the yield of DSA-n. Taking advantage of the phase diagram in Figure 33, one can potentially follow the suggested combination of liquid film thickness and nanoparticle density as a starting point for an experiment. Since we have neglected a few parameters, it is very likely that the predicted yield in Figure 33 obtained from our MDPD model and machine learning algorithm does not corroborate very closely with the one from the experiment. We believe that aforementioned predictions can be improved by utilizing the machine learning model and feedback loop from the experiments. Every new experimental data will be entered into the training dataset with a higher weight, which will be used to optimize the parameters while maximizing the yield. Feedback from experiments should be done iteratively to improve the learning rate; hence, the machine learning predictions. Utilizing this feedback loop, the machine learning model will predict the optimal combination of liquid film thickness and nanoparticle density to control non-equilibrium process of DSA-n. As such the underlying phase diagram in Figure 33 will be continuously updated while incorporating experimental observations until convergence is reached.

Despite above mentioned feedback loop from experiments, it is likely that the combination of the two factors considered in this work, i.e. the liquid film thickness and the nanoparticle density, would lead to a phase diagram that is far from convergence. In this case, the two

dimensional phase diagram will no longer be sufficient to optimize the DSA-n process. We hypothesize that in addition to the liquid film thickness and nanoparticle density, which were discussed in chapter 5, there are other parameters that can affect the yield of DSA-n, and need to be taken into account to improve the accuracy of the phase diagram.

One possible direction would be the design of templated substrate, where geometrical constraints are added. These constraints include nanocavity shape, radius, and lattice configuration. We discussed the impact of the nanocavity radius and center-to-center distance in chapter 5; however, a larger range of parameter sweep will be necessary. In addition, the results from the varying nanocavity radius, and center-to-center distance need to be incorporated into the phase diagram.

Another possible direction is to include other properties of the liquid film, such as speed of receding contact line, and strength of interactions between the nanoparticles, substrate, and the liquid film. In chapters 4 and 5, we discussed the local confinement, and the importance of receding contact angle, which can be tuned through liquid-solid interactions. Overall, we believe that our MDPD and machine learning model has the potential to explore all parameters mentioned above. A further sensitivity analysis and uncertainty quantification of the machine learning predictions will also shed light on the importance of each parameter to the extent that it improves the yield.

For these future directions, there are numerous possibilities for the aforementioned parameters, which cannot be investigated solely by experimental observations. In such a hyper-

dimensional parameter space, MDPD simulations will save time, and aid in narrowing the design parameters required for DSA-n.

REFERENCES

1. Denkov, N. D., Velev, O. D., Kralchevsky, P. A., Ivanov, I. B., Yoshimura, H., and Nagayama, K.: Two-dimensional crystallization. Nature, 361(6407):26–26, 1993.
2. Kralchevsky, P. A. and Nagayama, K.: Capillary forces between colloidal particles. Langmuir, 10(1):23–36, 1994.
3. Deegan, R. D., Bakajin, O., Dupont, T. F., Huber, G., Nagel, S. R., and Witten, T. A.: Capillary flow as the cause of ring stains from dried liquid drops. Nature, 389(6653):827–829, 1997.
4. Ball, P.: Fluid dynamics how coffee leaves its mark. Nature, 389(6653):788–788, 1997.
5. De Gennes, P. G.: Solvent evaporation of spin cast films: ”crust” effects. The European Physical Journal E, 7(1):31–34, 2002.
6. Witten, T. A.: Robust fadeout profile of an evaporation stain. Europhysics Letters, 86(6):64002, 2009.
7. Wink, T., vanZuilen, S. J., Bult, A., and vanBennekorn, W. P.: Self-assembled monolayers for biosensors. Analyst, 122(4):R43–R50, 1997.
8. Norris, D. J. and Vlasov, Y. A.: Chemical approaches to three-dimensional semiconductor photonic crystals. Advanced Materials, 13(6):371–376, 2001.
9. Zhou, X. Z., Zhou, Y., Ku, J. C., Zhang, C., and Mirkin, C. A.: Capillary force-driven, large-area alignment of multi-segmented nanowires. ACS Nano, 8(2):1511–1516, 2014.
10. Kraus, T., Malaquin, L., Schmid, H., Riess, W., Spencer, N. D., and Wolf, H.: Nanoparticle printing with single-particle resolution. Nature Nanotechnology, 2(9):570–576, 2007.
11. DeVries, G. A., Brunnbauer, M., Hu, Y., Jackson, A. M., Long, B., Neltner, B. T., Uzun, O., Wunsch, B. H., and Stellacci, F.: Divalent metal nanoparticles. Science, 315(5810):358–361, 2007.

12. Nie, Z., Fava, D., Kumacheva, E., Zou, S., Walker, G. C., and Rubinstein, M.: Self-assembly of metal-polymer analogues of amphiphilic triblock copolymers. Nature Materials, 6(8):609–614, 2007.
13. Kang, Y. J., Erickson, K. J., and Taton, T. A.: Plasmonic nanoparticle chains via a morphological, sphere-to-string transition. Journal of The American Chemical Society, 127(40):13800–13801, 2005.
14. Caswell, K. K., Murphy, C. J., Wilson, J. N., and Bunz, U. H. F.: Preferential end-to-end assembly of gold nanorods by biotin-streptavidin connectors. Abstracts of Papers of The American Chemical Society, 226(1):U686–U687, 2003.
15. Sharma, J., Chhabra, R., Cheng, A., Brownell, J., Liu, Y., and Yan, H.: Control of self-assembly of dna tubules through integration of gold nanoparticles. Science, 323(5910):112–116, 2009.
16. Iacovella, C. R. and Glotzer, S. C.: Complex crystal structures formed by the self-assembly of ditethered nanospheres. Nano Letters, 9(3):1206–1211, 2009.
17. Zhang, S., Pelligra, C. I., Feng, X., and Osuji, C. O.: Directed assembly of hybrid nanomaterials and nanocomposites. Advanced Materials, 30(18):1705794, 2018.
18. Nie, Z., Petukhova, A., and Kumacheva, E.: Properties and emerging applications of self-assembled structures made from inorganic nanoparticles. Nature Nanotechnology, 5(1):15–25, 2010.
19. Lin, C., Chen, S., Xiao, L., and Liu, Y.: Tuning drop motion by chemical chessboard-patterned surfaces: a many-body dissipative particle dynamics study. Langmuir, 34:2708–2715, 2018.
20. Brown, D. A., Kim, J. H., Lee, H. B., Fotouhi, G., Lee, K. H., Liu, W. K., and Chung, J. H.: Electric field guided assembly of one-dimensional nanostructures for high performance sensors. Sensors, 12(5):5725–5751, 2012.
21. Tracy, J. B. and Crawford, T. M.: Magnetic field-directed self-assembly of magnetic nanoparticles. Mrs Bulletin, 38(11):915–920, 2013.
22. Su, B., Wu, Y., and Jiang, L.: The art of aligning one-dimensional (1d) nanostructures. Chemical Society Reviews, 41(23):7832–7856, 2012.

23. Modestino, M. A., Chan, E. R., Hexemer, A., Urban, J. J., and Segalman, R. A.: Controlling nanorod self-assembly in polymer thin films. Macromolecules, 44(18):7364–7371, 2011.
24. Zhong, G., Warner, J. H., Fouquet, M., Robertson, A. W., Chen, B., and Robertson, J.: Growth of ultrahigh density single-walled carbon nanotube forests by improved catalyst design. ACS Nano, 6(4):2893–2903, 2012.
25. Shields, C. W., Zhu, S., Yang, Y., Bharti, B., Liu, J., Yellen, B. B., Velev, O. D., and Lopez, G. P.: Field-directed assembly of patchy anisotropic microparticles with defined shape. Soft Matter, 9(38):9219–9229, 2013.
26. Li, Y. C., Liu, H., Huang, X. R., and Sun, C. C.: Evaporation- and surface-induced morphology of symmetric diblock copolymer thin films: a multibody dissipative particle dynamics study. Molecular Simulation, 37:875–883, 2011.
27. Zhang, S., Li, Q., Kinloch, I. A., and Windle, A. H.: Ordering in a droplet of an aqueous suspension of single-wall carbon nanotubes on a solid substrate. Langmuir, 26(3):2107–2112, 2010.
28. Hu, L., Chen, M., Fang, X., and Wu, L.: Oil-water interfacial self-assembly: a novel strategy for nanofilm and nanodevice fabrication. Chemical Society Reviews, 41(3):1350–1362, 2012.
29. Yin, Y. D., Lu, Y., Gates, B., and Xia, Y. N.: Template-assisted self-assembly: A practical route to complex aggregates of monodispersed colloids with well-defined sizes, shapes, and structures. Journal of The American Chemical Society, 123(36):8718–8729, 2001.
30. Xia, Y., Goral, J., Huang, H., Miskovic, I., Meakin, P., and Deo, M.: Many-body dissipative particle dynamics modeling of fluid flow in fine-grained nanoporous shales. Physics Of Fluids, 29(5):056601, 2017.
31. Flauraud, V., Mastrangeli, M., Bernasconi, G. D., Butet, J., Alexander, D. T. L., Shahrabi, E., Martin, O. J. F., and Brugger, J.: Nanoscale topographical control of capillary assembly of nanoparticles. Nature Nanotechnology, 12(1):73–80, 2017.
32. Karg, M., Koenig, T. A. F., Retsch, M., Stelling, C., Reichstein, P. M., Honold, T., Thelakkat, M., and Fery, A.: Colloidal self-assembly concepts for light management in photovoltaics. Materials Today, 18(4):185–205, 2015.

33. Wang, F. and Wu, H.: Molecular origin of contact line stick-slip motion during droplet evaporation. Scientific Reports, 5(DEC 2):17521, 2015.
34. Ni, X., Wong, Z. J., Mrejen, M., Wang, Y., and Zhang, X.: An ultrathin invisibility skin cloak for visible light. Science, 349(6254):1310–1314, 2015.
35. Schurig, D., Mock, J. J., Justice, B. J., Cummer, S. A., Pendry, J. B., Starr, A. F., and Smith, D. R.: Metamaterial electromagnetic cloak at microwave frequencies. Science, 314(5801):977–980, 2006.
36. Lu, D. and Liu, Z.: Hyperlenses and metalenses for far-field super-resolution imaging. Nature Communications, 3:1205, 2012.
37. Mayer, M., Schnepf, M. J., Koenig, T. A. F., and Fery, A.: Colloidal self-assembly concepts for plasmonic metasurfaces. Advanced Optical Materials, 7(1):1800564, 2019.
38. Yan, H., Choe, H. S., Nam, S. W., Hu, Y., Das, S., Klemic, J. F., Ellenbogen, J. C., and Lieber, C. M.: Programmable nanowire circuits for nanoprocessors. Nature, 470(7333):240–244, 2011.
39. Chen, K. I., Li, B. R., and Chen, Y. T.: Silicon nanowire field-effect transistor-based biosensors for biomedical diagnosis and cellular recording investigation. Nano Today, 6(2):131–154, 2011.
40. Yang, J. X., Koplik, J., and Banavar, J. R.: Terraced spreading of simple liquids on solid-surfaces. Physical Review A, 46(12):7738–7749, 1992.
41. Collet, M., Salomon, S., Klein, N. Y., Seichepine, F., Vieu, C., Nicu, L., and Larrieu, G.: Large-scale assembly of single nanowires through capillary-assisted dielectrophoresis. Advanced Materials, 27(7):1268–1273, 2015.
42. Yu, G., Gao, J., Hummelen, J. C., Wudl, F., and Heeger, A. J.: Polymer photovoltaic cells - enhanced efficiencies via a network of internal donor-acceptor heterojunctions. Science, 270(5243):1789–1791, 1995.
43. Halls, J. J. M., Walsh, C. A., Greenham, N. C., Marseglia, E. A., Friend, R. H., Moratti, S. C., and Holmes, A. B.: Efficient photodiodes from interpenetrating polymer networks. Nature, 376(6540):498–500, 1995.

44. McGehee, M. D.: Nanostructured organic-inorganic hybrid solar cells. Mrs Bulletin, 34(2):95–100, 2009.
45. Thompson, B. C. and Frechet, J. M. J.: Organic photovoltaics polymer-fullerene composite solar cells. Angewandte Chemie-International Edition, 47(1):58–77, 2008.
46. Briseno, A. L., Holcombe, T. W., Boukai, A. I., Garnett, E. C., Shelton, S. W., Frechet, J. J. M., and Yang, P.: Oligo- and polythiophene/zno hybrid nanowire solar cells. Nano Letters, 10(1):334–340, 2010.
47. Schierhorn, M., Boettcher, S. W., Peet, J. H., Matioli, E., Bazan, G. C., Stucky, G. D., and Moskovits, M.: Cdse nanorods dominate photocurrent of hybrid cdse-p3ht photovoltaic cell. ACS Nano, 4(10):6132–6136, 2010.
48. Chuang, C. H., Lin, Y. Y., Tseng, Y. H., Chu, T. H., Lin, C. C., Su, W. F., and Chen, C. W.: Nanoscale morphology control of polymer/tio2 nanocrystal hybrids: photo-physics, charge generation, charge transport, and photovoltaic properties. Journal of Physical Chemistry C, 114(43):18717–18724, 2010.
49. Zhang, S., Pelligra, C. I., Keskar, G., Jiang, J., Majewski, P. W., Taylor, A. D., Ismail-Beigi, S., Pfefferle, L. D., and Osuji, C. O.: Directed self-assembly of hybrid oxide/polymer core/shell nanowires with transport optimized morphology for photovoltaics. Advanced Materials, 24(1):82–87, 2012.
50. Abraham, D. B., Collet, P., De Coninck, J., and Dunlop, F.: Langevin dynamics of spreading and wetting. Physical Review Letters, 65(2):195–198, 1990.
51. Greybush, N. J., Saboktakin, M., Ye, X., Della, C., Oh, S. J., Berry, N. E., Engheta, N., Murray, C. B., and Kagan, C. R.: Plasmon-enhanced upconversion luminescence in single nanophosphor-nanorod heterodimers formed through template-assisted self-assembly. ACS Nano, 8(9):9482–9491, 2014.
52. Malaquin, L., Kraus, T., Schmid, H., Delamarche, E., and Wolf, H.: Controlled particle placement through convective and capillary assembly. Langmuir, 23(23):11513–11521, 2007.
53. Ni, S., Leemann, J., Wolf, H., and Isa, L.: Insights into mechanisms of capillary assembly. Faraday Discussions, 181:225–242, 2015.

54. Henzie, J., Andrews, S. C., Ling, X. Y., Li, Z., and Yang, P.: Oriented assembly of polyhedral plasmonic nanoparticle clusters. Proceedings of the National Academy of Sciences of the United States of America, 110(17):6640–6645, 2013.
55. Zhou, Y., Zhou, X., Park, D. J., Torabi, K., Brown, K. A., Jones, M. R., Zhang, C., Schatz, G. C., and Mirkin, C. A.: Shape-selective deposition and assembly of anisotropic nanoparticles. NANO Letters, 14(4):2157–2161, 2014.
56. Wang, Z., Yen, H., Chang, C., Sheng, Y., and Tsao, H.: Trapped liquid drop at the end of capillary. Langmuir, 29(39):12154–12161, 2013.
57. Kuemin, C., Nowack, L., Bozano, L., Spencer, N. D., and Wolf, H.: Oriented assembly of gold nanorods on the single-particle level. Advanced Functional Materials, 22(4):702–708, 2012.
58. Asbahi, M., Mehraeen, S., Lim, K. T. P., Wang, F., Cao, J., Tan, M. C., and Yang, J. K. W.: Template-induced structure transition in sub-10 nm self-assembling nanoparticles. Nano Letters, 14(5):2642–2646, 2014.
59. Mehraeen, S., Asbahi, M., F., W., Yang, J. K. W., Cao, J., and Tan, M. C.: Directed self-assembly of sub-10 nm particles: Role of driving forces and template geometry in packing and ordering. Langmuir, 31(31):8548–8557, 2015.
60. Asbahi, M., Mehraeen, S., Wang, F., Yakovlev, N., Chong, K. S. L., Cao, J., Tan, M. C., and Yang, J. K. W.: Large area directed self-assembly of sub-10 nm particles with single particle positioning resolution. Nano Letters, 15(9):6066–6070, 2015.
61. De Gennes, P. G.: Wetting: statics and dynamics. Reviews of Modern Physics, 57(3):827–863, 1985.
62. Forcada, M. L. and Mate, C. M.: Molecular layering during evaporation of ultrathin liquid films. Nature, 363(6429):527–529, 1993.
63. Leger, L. and Joanny, J. F.: Liquid spreading. Reports on Progress in Physics, 55(4):431–486, 1992.
64. Cazabat, A. M.: How does a droplet spread. Contemporary Physics, 28(4):347–364, 1987.
65. Voue, M. and De Coninck, J.: Spreading and wetting at the microscopic scale: recent developments and perspectives. Acta Materialia, 48(18-19):4405–4417, 2000.

66. Tanner, L. H.: Spreading of silicone oil drops on horizontal surfaces. Journal of Physics D: Applied Physics, 12(9):1473, 1979.
67. Joanny, J. F. and De Gennes, P. G.: Upward creep of a wetting fluid: a scaling analysis. Journal De Physique, 47(1):121–127, 1986.
68. Brochard, F.: Spreading of liquid drops on thin cylinders: The manchon-droplet transition. The Journal of Chemical Physics, 84(8):4664–4672, 1986.
69. Brochard-Wyart, F., De Gennes, P. G., and Herve, H.: Wetting of stratified solids. Advances in Colloid and Interface Science, 34:561–582, 1991.
70. Ausserre, D., Picard, A. M., and Leger, L.: Existence and role of the precursor film in the spreading of polymer liquids. Physical Review Letters, 57(21):2671–2674, 1986.
71. Hardy, W. B.: The spreading of fluids on glass. The London, Edinburgh, and Dublin Philosophical Magazine and Journal of Science, 38(223):49–55, 1919.
72. Burlatsky, S. F., Oshanin, G., Cazabat, A. M., Moreau, M., and Reinhardt, W. P.: Spreading of a thin wetting film: Microscopic approach. Physical Review E, 54(4):3832–3845, 1996.
73. Heslot, F., Cazabat, A. M., Levinson, P., and Fraysse, N.: Experiments on wetting on the scale of nanometers: Influence of the surface energy. Physical Review Letters, 65(5):599–602, 1990.
74. Tiberg, F. and Cazabat, A. M.: Self-assembly and spreading of nonionic trisiloxane surfactants. Europhysics Letters, 25(3):205–210, 1994.
75. Cazabat, A. M., De Coninck, J., Hoorelbeke, S., Valignat, M. P., and Villette, S.: Influence of substrate heterogeneities on the spreading of a drop. Physical Review E, 49(5):4149–4153, 1994.
76. Heslot, F., Cazabat, A. M., and Fraysse, N.: Diffusion-controlled wetting films. Journal of Physics: Condensed Matter, 1(33):5793–5798, 1989.
77. Cazabat, A. M., Fraysse, N., and Heslot, F.: Thin wetting films. Colloids and Surfaces, 52(1):1–8, 1991.

78. Daillant, J., Benattar, J. J., and Leger, L.: Ultrathin films in wetting evidenced by x-ray reflectivity. Physical Review A, 41(4):1963–1977, 1990.
79. Albrecht, U., Otto, A., and Leiderer, P.: 2-dimensional liquid polymer diffusion: experiment and simulation. Physical Review Letters, 68(21):3192–3195, 1992.
80. Perez, E., Schaffer, E., and Steiner, U.: Spreading dynamics of polydimethylsiloxane drops: Crossover from laplace to van der waals spreading. Journal of Colloid and Interface Science, 234(1):178–193, 2001.
81. Lukkarinen, A., Kaski, K., and Abraham, D. B.: Mechanisms of fluid spreading: Ising model simulations. Physical Review E, 51(3):2199–2202, 1995.
82. Abraham, D. B., Cuerno, R., and Moro, E.: Microscopic model for thin film spreading. Physical Review Letters, 88(20):206101, 2002.
83. Oshanin, G., De Coninck, J., Cazabat, A. M., and Moreau, M.: Microscopic model for spreading of a two-dimensional monolayer. Journal of Molecular Liquids, 76(3):195–219, 1998.
84. Nieminen, J. A. and Alanissila, T.: Spreading dynamics of polymer microdroplets: A molecular-dynamics study. Physical Review E, 49(5):4228–4236, 1994.
85. Haataja, M., Nieminen, J. A., and Alanissila, T.: Dynamics of the spreading of chainlike molecules with asymmetric surface interactions. Physical Review E, 53(5):5111–5122, 1996.
86. De Coninck, J.: Spreading of chain-like liquid droplets on solids. Colloids and Surfaces A: Physicochemical and Engineering Aspects, 114(2):155–160, 1996.
87. Bekink, S., Karaborni, S., Verbist, G., and Esselink, K.: Simulating the spreading of a drop in the terraced wetting regime. Physical Review Letters, 76(20):3766–3769, 1996.
88. Heine, D. R., Grest, G. S., and Webb, E. B.: Spreading dynamics of polymer nanodroplets. Physical Review E, 68(6):061603, 2003.
89. Popescu, M. N. and Dietrich, S.: Model for spreading of liquid monolayers. Physical Review E, 69(6):061602, 2004.

90. Abraham, D. B., Heinio, J., and Kaski, K.: Computer simulation studies of fluid spreading. Journal of Physics A: Mathematical and General, 24(6):L309–L315, 1991.
91. Heinio, J., Kaski, K., and Abraham, D. B.: Dynamics of a microscopic droplet on a solid surface: Theory and simulation. Physical Review B, 45(8):4409–4416, 1992.
92. Young, T.: An essay on the cohesion of fluids. Philosophical Transactions of the Royal Society of London, 95:65–87, 1805.
93. Battaile, C. C.: The kinetic monte carlo method: Foundation, implementation, and application. Computer Methods in Applied Mechanics and Engineering, 197(41):3386–3398, 2008.
94. Newman, M. E. J. and Barkema, G. T.: Monte Carlo Methods in Statistical Physics. Oxford University Press, 1999.
95. Domb, C.: Phase transitions and critical phenomena. Academic Press, 2000.
96. Binder, K., Heermann, D., Roelofs, L., Mallinckrodt, A. J., and McKay, S.: Monte carlo simulation in statistical physics. Computers in Physics, 7(2):156–157, 1993.
97. Barabasi, A. L. and Stanley, H. E.: Fractal concepts in surface growth. Cambridge University Press, 1995.
98. Tadmor, R., Das, R., Gulec, S., Liu, J., N’guessan, H. E., Shah, M., Wasnik, P. S., and Yadav, S. B.: Solid-liquid work of adhesion. Langmuir, 33(15):3594–3600, 2017.
99. Tadmor, R., Bahadur, P., Leh, A., N’guessan, H. E., Jaini, R., and Dang, L.: Measurement of lateral adhesion forces at the interface between a liquid drop and a substrate. Physical Review Letters, 103(26):266101, 2009.
100. N’guessan, H. E., Leh, A., Cox, P., Bahadur, P., Tadmor, R., Patra, P., Vajtai, R., Ajayan, P. M., and Wasnik, P.: Water tribology on graphene. Nature Communications, 3:1242, 2012.
101. Leh, A., N’guessan, H. E., Fan, J., Bahadur, P., Tadmor, R., and Zhao, Y.: On the role of the three-phase contact line in surface deformation. Langmuir, 28(13):5795–5801, 2012.

102. Sellinger, A., Weiss, P. M., Nguyen, A., Lu, Y. F., Assink, R. A., Gong, W. L., and Brinker, C. J.: Continuous self-assembly of organic-inorganic nanocomposite coatings that mimic nacre. Nature, 394(6690):256–260, 1998.
103. Morrow, N. R. and Mason, G.: Recovery of oil by spontaneous imbibition. Current Opinion In Colloid & Interface Science, 6(4):321–337, 2001.
104. Cazabat, A. M.: Thin wetting films. Colloids and Surfaces, 52(0166-6622):1 – 8, 1991.
105. Cazabat, A. M., De Coninck, J., Hoorelbeke, S., Valignat, M. P., and Villette, S.: Influence of substrate heterogeneities on the spreading of a drop. Physical Review E, 49:4149–4153, 1994.
106. De Coninck, J., Fraysse, N., Valignat, M. P., and Cazabat, A. M.: A microscopic simulation of the spreading of layered droplets. Langmuir, 9(7):1906–1909, 1993.
107. De Coninck, J., Hoorelbeke, S., Valignat, M. P., and Cazabat, A. M.: Effective microscopic model for the dynamics of spreading. Physical Review E, 48:4549–4555, 1993.
108. Burlatsky, S. F., Oshanin, G., Cazabat, A. M., Moreau, M., and Reinhardt, W. P.: Spreading of a thin wetting film: Microscopic approach. Physical Review E, 54(4):3832–3845, 1996.
109. Burlatsky, S. F., Oshanin, G., Cazabat, A. M., and Moreau, M.: Microscopic model of upward creep of an ultrathin wetting film. Physical Review Letters, 76(1):86–89, 1996.
110. Abraham, D. B., Collet, P., De Coninck, J., and Dunlop, F.: Langevin dynamics of spreading and wetting. Physical Review Letters, 65:195–198, 1990.
111. Yang, J.-x., Koplik, J., and Banavar, J. R.: Terraced spreading of simple liquids on solid surfaces. Physical Review A, 46:7738–7749, 1992.
112. Yang, J.-x., Koplik, J., and Banavar, J. R.: Molecular dynamics of drop spreading on a solid surface. Physical Review Letters, 67:3539–3542, 1991.
113. Nieminen, J. A., Abraham, D. B., Karttunen, M., and Kaski, K.: Molecular dynamics of a microscopic droplet on solid surface. Physical Review Letters, 69:124–127, 1992.

114. De Coninck, J.: Spreading of chain-like liquid droplets on solids. Colloids and Surfaces A: Physicochemical and Engineering Aspects, 114:155–160, 1996.
115. De Coninck, J., D’Ortona, U., Koplik, J., and Banavar, J. R.: Terraced spreading of chain molecules via molecular dynamics. Physical Review Letters, 74:928–931, 1995.
116. Nieminen, J. A. and Alanissila, T.: Spreading dynamics of polymer microdroplets: A molecular-dynamics study. Physical Review E, 49(5):4228–4236, 1994.
117. Hoogerbrugge, P. J. and Koelman, J. M. V. A.: Simulating microscopic hydrodynamic phenomena with dissipative particle dynamics. Europhysics Letters, 19(3):155–160, 1992.
118. Koelman, J. M. V. A. and Hoogerbrugge, P. J.: Dynamic simulations of hard-sphere suspensions under steady shear. Europhysics Letters, 21(3):363–368, 1993.
119. Kong, B. and Yang, X. Z.: Dissipative particle dynamics simulation of contact angle hysteresis on a patterned solid/air composite surface. Langmuir, 22(5):2065–2073, 2006.
120. Liu, M., Meakin, P., and Huang, H.: Dissipative particle dynamics simulation of multi-phase fluid flow in microchannels and microchannel networks. Physics Of Fluids, 19(3):033302, 2007.
121. Pagonabarraga, I. and Frenkel, D.: Dissipative particle dynamics for interacting systems. Journal Of Chemical Physics, 115(11):5015–5026, 2001.
122. Warren, P. B.: Hydrodynamic bubble coarsening in off-critical vapor-liquid phase separation. Physical Review Letters, 87(22):225702, 2001.
123. Trofimov, S. Y., Nies, E. L. F., and Michels, M. A. J.: Constant-pressure simulations with dissipative particle dynamics. Journal Of Chemical Physics, 123(14):144102, 2005.
124. Chen, C., Zhuang, L., Li, X., Dong, J., and Lu, J.: A many-body dissipative particle dynamics study of forced water-oil displacement in capillary. Langmuir, 28(2):1330–1336, 2012.

125. Chen, C., Lu, K., Li, X., Dong, J., Lu, J., and Zhuang, L.: A many-body dissipative particle dynamics study of fluid-fluid spontaneous capillary displacement. RSC Advances, 4(13):6545–6555, 2014.
126. Chen, C., Gao, C., Zhuang, L., Li, X., Wu, P., Dong, J., and Lu, J.: A many-body dissipative particle dynamics study of spontaneous capillary imbibition and drainage. Langmuir, 26(12):9533–9538, 2010.
127. Henrich, B., Cupelli, C., Moseler, M., and Santer, M.: An adhesive dpd wall model for dynamic wetting. Europhysics Letters, 80(6):60004, 2007.
128. Louis, A. A., Bolhuis, P. G., and Hansen, J. P.: Mean-field fluid behavior of the gaussian core model. Physical Review E, 62(6, A):7961–7972, 2000.
129. Arienti, M., Pan, W., Li, X., and Karniadakis, G.: Many-body dissipative particle dynamics simulation of liquid/vapor and liquid/solid interactions. Journal Of Chemical Physics, 134(20):204114, 2011.
130. Warren, P. B.: Vapor-liquid coexistence in many-body dissipative particle dynamics. Physical Review E, 68(6,2):066702, 2003.
131. Espanol, P. and Warren, P.: Statistical-mechanics of dissipative particle dynamics. Europhysics Letters, 30(4):191–196, 1995.
132. Groot, R. D. and Warren, P. B.: Dissipative particle dynamics: Bridging the gap between atomistic and mesoscopic simulation. Journal Of Chemical Physics, 107(11):4423–4435, 1997.
133. Irving, J. H. and Kirkwood, J. G.: The statistical mechanical theory of transport processes. iv. the equations of hydrodynamics. The Journal of Chemical Physics, 18(6):817–829, 1950.
134. Jones, J. L., Lal, M., Ruddock, J. N., and Spenley, N. A.: Dynamics of a drop at a liquid/solid interface in simple shear fields: A mesoscopic simulation study. Faraday Discussions, 112:129–142, 1999.
135. Luo, Z. and Mehraeen, S.: Predictive model to probe the impact of gravity and surface tension on rising wetting thin films. Langmuir, 35(11):4189–4196, 2019.

136. Heinz, H., Paul, W., and Binder, K.: Calculation of local pressure tensors in systems with many-body interactions. Physical Review E, 72(6,2):066704, 2005.
137. Sui, Y., Ding, H., and Spelt, P. D. M.: Numerical simulations of flows with moving contact lines. Annual Review of Fluid Mechanics, 46:97–119, 2014.
138. Seemann, R., Brinkmann, M., Pfohl, T., and Herminghaus, S.: Droplet based microfluidics. Reports On Progress In Physics, 75(1):016601, 2012.
139. Khojasteh, D., Kazerooni, M., Salarian, S., and Kamali, R.: Droplet impact on superhydrophobic surfaces: A review of recent developments. Journal of Industrial and Engineering Chemistry, 42:1–14, 2016.
140. Quere, D.: Wetting and roughness. Annual review of materials research, 38:71–99, 2008.
141. Marmur, A.: Wetting on hydrophobic rough surfaces: To be heterogeneous or not to be. Langmuir, 19(20):8343–8348, 2003.
142. Metya, A. K., Khan, S., and Singh, J. K.: Wetting transition of the ethanol-water droplet on smooth and textured surfaces. Journal of Physical Chemistry C, 118(8):4113–4121, 2014.
143. Kwon, H. M., Paxson, A. T., Varanasi, K. K., and Patankar, N. A.: Rapid deceleration-driven wetting transition during pendant drop deposition on superhydrophobic surfaces. Physical Review Letters, 106(3):036102, 2011.
144. Cheng, D. F. and McCarthy, T. J.: Using the fact that wetting is contact line dependent. Langmuir, 27(7):3693–3697, 2011.
145. Bormashenko, E.: A variational approach to wetting of composite surfaces: Is wetting of composite surfaces a one-dimensional or two-dimensional phenomenon. Langmuir, 25(18):10451–10454, 2009.
146. McHale, G.: Cassie and wenzel: Were they really so wrong. Langmuir, 23(15):8200–8205, 2007.
147. Gao, L. and McCarthy, T. J.: How wenzel and cassie were wrong. Langmuir, 23(7):3762–3765, 2007.

148. Weng, Y. H., Liang, Y. E., Sheng, Y. J., and Tsao, H. K.: Evaporation- and surface-induced morphology of symmetric diblock copolymer thin films: a multibody dissipative particle dynamics study. Journal of Physical Chemistry C, 122:2231–2237, 2018.
149. Mistura, G. and Pierno, M.: Drop mobility on chemically heterogeneous and lubricant-impregnated surfaces. Advances in Physics-X, 2(3):591–607, 2017.
150. Morita, M., Koga, T., Otsuka, H., and Takahara, A.: Macroscopic-wetting anisotropy on the line-patterned surface of fluoroalkylsilane monolayers. Langmuir, 21(3):911–918, 2005.
151. Suzuki, S., Nakajima, A., Tanaka, K., Sakai, M., Hashimoto, A., Yoshida, N., Kameshima, Y., and Okada, K.: Sliding behavior of water droplets on line-patterned hydrophobic surfaces. Applied Surface Science, 254(6):1797–1805, 2008.
152. Herminghaus, S., Brinkmann, M., and Seemann, R.: Wetting and dewetting of complex surface geometries. Annual Review of Materials Research, 38:101–121, 2008.
153. Chen, X., Ma, R., Li, J., Hao, C., Guo, W., Luk, B. L., Li, S. C., Yao, S., and Wang, Z.: Evaporation of droplets on superhydrophobic surfaces: surface roughness and small droplet size effects. Physical Review Letters, 109(12):129904, 2012.
154. Kanungo, M., Mettu, S., Law, K., and Daniel, S.: Effect of roughness geometry on wetting and dewetting of rough pdms surfaces. Langmuir, 30(25):7358–7368, 2014.
155. Sbragaglia, M., Biferale, L., Amati, G., Varagnolo, S., Ferraro, D., Mistura, G., and Pierno, M.: Sliding drops across alternating hydrophobic and hydrophilic stripes. Physical Review E, 89(1):012406, 2014.
156. Song, J. H., Sakai, M., Yoshida, N., Suzuki, S., Kameshima, Y., and Nakajima, A.: Dynamic hydrophobicity of water droplets on the line-patterned hydrophobic surfaces. Surface Science, 600(13):2711–2717, 2006.
157. Jansen, H. P., Bliznyuk, O., Kooij, E. S., Poelsema, B., and Zandvliet, H. J. W.: Simulating anisotropic droplet shapes on chemically striped patterned surfaces. Langmuir, 28(1):499–505, 2012.
158. Sheng, Y., Jiang, S., and Tsao, H.: Effects of geometrical characteristics of surface roughness on droplet wetting. Journal of Chemical Physics, 127(23):234704, 2007.

159. Luo, Z. and Mehraeen, S.: Predictive model to probe the impact of gravity and surface tension on rising wetting thin films. Langmuir, 35(11):4189–4196, 2019.
160. Joanny, J. F. and Degennes, P. G.: A model for contact-angle hysteresis. Journal of Chemical Physics, 81(1):552–562, 1984.
161. Nadkarni, G. D. and Garoff, S.: An investigation of microscopic aspects of contact-angle hysteresis - pinning of the contact line on a single defect. Europhysics Letters, 20(6):523–528, 1992.
162. Espanol, P.: Hydrodynamics from dissipative particle dynamics. Phys. Rev. E, 52:1734–1742, 1995.
163. Yong, X., Qin, S., and Singler, T. J.: Nanoparticle-mediated evaporation at liquid-vapor interfaces. Extreme Mechanics Letters, 7:90–103, 2016.
164. Miller, K., Tsyrenova, A., Anthony, S. M., Qin, S., Yong, X., and Jiang, S.: Drying mediated orientation and assembly structure of amphiphilic janus particles. Soft Matter, 14:6793–6798, 2018.
165. Hastie, T., Tibshirani, R., and Friedman, J.: The elements of statistical learning. Springer, 2009.
166. Bishop, C.: Pattern recognition and machine learning. Springer, 2006.
167. Murphy, K. P.: Machine learning: A probabilistic perspective. The MIT Press, 2012.
168. Luo, Z. and Mehraeen, S.: Unraveling the mechanism of a rising three-phase contact line along a vertical surface using many-body dissipative particle dynamics. Langmuir, 36(26):7474–7482, 2020.
169. Liu, Y., Wang, J., Zhang, X., and Wang, W.: Contact line pinning and the relationship between nanobubbles and substrates. Journal of Chemical Physics, 140(5):054705, 2014.
170. Dussan V., E. B. and Davis, S. H.: On the motion of a fluid-fluid interface along a solid surface. Journal of Fluid Mechanics, 65(1):71–95, 1974.

171. Berim, G. O. and Ruckenstein, E.: Nanodrop on a nanorough hydrophilic solid surface: Contact angle dependence on the size, arrangement, and composition of the pillars. Journal Of Colloid And Interface Science, 359(1):304–310, 2011.
172. Wang, X., Qian, T., and Sheng, P.: Moving contact line on chemically patterned surfaces. Journal of Fluid Mechanics, 605:59–78, 2008.
173. Varagnolo, S., Ferraro, D., Fantinel, P., Pierno, M., Mistura, G., Amati, G., Biferale, L., and Sbragaglia, M.: Stick-slip sliding of water drops on chemically heterogeneous surfaces. Physical Review Letters, 111(6):066101, 2013.
174. Pierce, E., Carmona, F. J., and Amirfazli, A.: Understanding of sliding and contact angle results in tilted plate experiments. Colloids and Surfaces A: Physicochemical and Engineering Aspects, 323(1-3):73–82, 2008.
175. Zhao, H., Park, K., and Law, K.: Effect of surface texturing on superoleophobicity, contact angle hysteresis, and robustness. Langmuir, 28(42):14925–14934, 2012.
176. Jiang, Z. H., Lin, L., Ma, D., Yun, S., Werner, D. H., Liu, Z., and Mayer, T. S.: Broad-band and wide field-of-view plasmonic metasurface-enabled waveplates. Scientific Reports, 4:7511, 2014.
177. Xi, C., Marina, P. F., Xia, H., and Wang, D.: Directed self-assembly of gold nanoparticles into plasmonic chains. Soft Matter, 11(23):4562–4571, 2015.
178. Ryan, K. M., Mastroianni, A., Stancil, K. A., Liu, H., and Alivisatos, A. P.: Electric-field-assisted assembly of erpendicularly oriented nanorod superlattices. NANO Letters, 6(7):1479–1482, 2006.
179. Li, L. S. and Alivisatos, A. P.: Semiconductor nanorod liquid crystals and their assembly on a substrate. Advanced Materials, 15(5):408–411, 2003.
180. Winkleman, A., Gates, B. D., McCarty, L. S., and Whitesides, G. M.: Directed self-assembly of spherical particles on patterned electrodes by an applied electric field. Advanced Materials, 17(12):1507–1511, 2005.
181. Parviz, B. A., Ryan, D., and Whitesides, G. M.: Using self-assembly for the fabrication of nano-scale electronic and photonic devices. IEEE Transactions on Advanced Packaging, 26(3):233–241, 2003.

182. Grzelczak, M., Vermant, J., Furst, E. M., and Liz-Marzan, L. M.: Directed self-assembly of nanoparticles. ACS Nano, 4(7):3591–3605, 2010.
183. Dong, Z., Asbahi, M., Lin, J., Zhu, D., Wang, Y. M., Hippalgaonkar, K., Chu, H. S., Goh, W. P., Wang, F., Huang, Z., and Yang, J. K. W.: Second-harmonic generation from sub-5 nm gaps by directed self-assembly of nanoparticles onto template stripped gold substrates. NANO Letters, 15(9):5976–5981, 2015.
184. Clark, T. D., Tien, J., Duffy, D. C., Paul, K. E., and Whitesides, G. M.: Self-assembly of 10- μ m-sized objects into ordered three-dimensional arrays. Journal of the American Chemical Society, 123(31):7677–7682, 2001.
185. Eklof-Osterberg, J., Lofgren, J., Erhart, P., and Moth-Poulsen, K.: Understanding interactions driving the template-directed self-assembly of colloidal nanoparticles at surfaces. Journal of Physical Chemistry C, 124(8):4660–4667, 2020.
186. Shillingford, C., Grebe, V., McMullen, A., Brujic, J., and Weck, M.: Assembly and dynamic analysis of square colloidal crystals via templated capillary assembly. Langmuir, 35(37):12205–12214, 2019.
187. Liddle, J. A., Cui, Y., and Alivisatos, A. P.: Lithographically directed self-assembly of nanostructures. Journal of Vacuum Science & Technology B, 22(6):3409–3414, 2004.
188. Chang, J. B., Choi, H. K., Hannon, A. F., Alexander-Katz, A., Ross, C. A., and Berggren, K. K.: Design rules for self-assembled block copolymer patterns using tiled templates. Nature Communications, 5:3305, 2014.
189. Duan, H. and Berggren, K. K.: Directed self-assembly at the 10 nm scale by using capillary force-induced nanocoherence. NANO Letters, 10(9):3710–3716, 2010.
190. Lu, Y., Yin, Y. D., and Xia, Y. N.: A self-assembly approach to the fabrication of patterned, two-dimensional arrays of microlenses of organic polymers. Advanced Materials, 13(1):34–37, 2001.
191. Yin, Y. D., Lu, Y., and Xia, Y. N.: A self-assembly approach to the formation of asymmetric dimers from monodispersed spherical colloids. Journal of the American Chemical Society, 123(4):771–772, 2001.

192. Yin, Y. D., Lu, Y., and Xia, Y. N.: Assembly of monodispersed spherical colloids into one-dimensional aggregates characterized by well-controlled structures and lengths. Journal of Materials Chemistry, 11(4):987–989, 2001.
193. Yin, Y. D. and Xia, Y. N.: Self-assembly of monodispersed spherical colloids into complex aggregates with well-defined sizes, shapes, and structures. Advanced Materials, 13(4):267–271, 2001.
194. Hughes, R. A., Menumenov, E., and Neretina, S.: When lithography meets self-assembly: a review of recent advances in the directed assembly of complex metal nanostructures on planar and textured surfaces. Nanotechnology, 28(28):282002, 2017.
195. Kuemin, C., Stutz, R., Spencer, N. D., and Wolf, H.: Precise placement of gold nanorods by capillary assembly. Langmuir, 27(10):6305–6310, 2011.
196. Li, B., Valverde, L. R., Zhang, F., Zhou, Y., Li, S., Diao, Y., Wilson, W. L., and Schroeder, C. M.: Macroscopic alignment and assembly of pi-conjugated oligopeptides using colloidal microchannels. ACS Applied Materials & Interfaces, 9(47):41586–41593, 2017.
197. Asbahi, M., Wang, F., Dong, Z., Yang, J. K. W., and Chong, K. S. L.: Directed self-assembly of sub-10nm particle clusters using topographical templates. Nanotechnology, 27(42):424001, 2016.
198. Luo, M. and Dai, L. L.: Molecular dynamics simulations of surfactant and nanoparticle self-assembly at liquid-liquid interfaces. Journal of Physics-Condensed Matter, 19(37):375109, 2007.
199. Zhang, Z. L., Horsch, M. A., Lamm, M. H., and Glotzer, S. C.: Tethered nano building blocks: Toward a conceptual framework for nanoparticle self-assembly. NANO Letters, 3(10):1341–1346, 2003.
200. Spaeth, J. R., Kevrekidis, I. G., and Panagiotopoulos, A. Z.: Dissipative particle dynamics simulations of polymer-protected nanoparticle self-assembly. Journal of Chemical Physics, 135(18):184903, 2011.
201. Knorowski, C., Burleigh, S., and Travesset, A.: Dynamics and statics of dna-programmable nanoparticle self-assembly and crystallization. Physical Review Letters, 106(21):215501, 2011.

202. Miller, K., Tsyrenova, A., Anthony, S. M., Qin, S., Yong, X., and Jiang, S.: Drying mediated orientation and assembly structure of amphiphilic janus particles. Soft Matter, 14(33):6793–6798, 2018.
203. Steinhardt, P. J., Nelson, D. R., and Ronchetti, M.: Bond-orientational order in liquids and glasses. Physics Review B, 28:784–805, 1983.
204. Aurenhammer, F., Klein, R., , and Lee, D. T.: Voronoi diagrams and Delaunay triangulations. World Scientific Publishing Company, 2013.
205. Ni, S., Leemann, J., Buttinoni, I., Isa, L., and Wolf, H.: Programmable colloidal molecules from sequential capillarity-assisted particle assembly. Science Advances, 2(4):e1501779, 2016.
206. Xia, Y. N., Yin, Y. D., Lu, Y., and McLellan, J.: Template-assisted self-assembly of spherical colloids into complex and controllable structures. Advanced Functional Materials, 13(12):907–918, 2003.
207. Mezei, M. and Beveridge, D. L.: Free energy simulations. Annals of the New York Academy of Sciences, 482(1):1–23, 1986.
208. Raut, V. P., Agashe, M. A., Stuart, S. J., and Latour, R. A.: Molecular dynamics simulations of peptide-surface interactions. Langmuir, 21(4):1629–1639, 2006.
209. Schneider, J. and Ciacchi, L. C.: A classical potential to model the adsorption of biological molecules on oxidized titanium surfaces. Journal of Chemical Theory and Computation, 7(2):473–484, 2011.
210. Kirkwood, J. G.: Statistical mechanics of fluid mixtures. The Journal of chemical physics, 3(5):300–313, 1935.
211. Notman, R. and Walsh, T. R.: Molecular dynamics studies of the interactions of water and amino acid analogues with quartz surfaces. Langmuir, 25(3):1638–1644, 2009.
212. Hoeffling, M., Iori, F., Corni, S., and Gottschalk, K. E.: Interaction of amino acids with the au (111) surface: adsorption free energies from molecular dynamics simulations. Langmuir, 26(11):8347–8351, 2010.
213. Jarzynski, C.: Nonequilibrium equality for free energy differences. Physical Review Letters, 78(14):2690–2693, 1997.

214. Isralewitz, B., Gao, M., and Schulten, K.: Steered molecular dynamics and mechanical functions of proteins. Current opinion in structural biology, 11(2):224–230, 2001.
215. Jarzynski, C.: Equilibrium free-energy differences from nonequilibrium measurements: A master-equation approach. Physical Review E, 56(5):5018–5035, 1997.
216. Krammer, A., Lu, H., Isralewitz, B., Schulten, K., and Vogel, V.: Forced unfolding of the fibronectin type iii module reveals a tensile molecular recognition switch. Proceedings of the National Academy of Sciences, 96(4):1351–1356, 1999.
217. Gao, M., Wilmanns, M., and Schulten, K.: Steered molecular dynamics studies of titin i1 domain unfolding. Biophysical Journal, 83(6):3435–3445, 2002.
218. Park, S., Khalili-Araghi, F., Tajkhorshid, E., and Schulten, K.: Free energy calculation from steered molecular dynamics simulations using jarzynski’s equality. The Journal of Chemical Physics, 119(6):3559–3566, 2003.
219. Cuendet, M. A. and Michielin, O.: Protein-protein interaction investigated by steered molecular dynamics: the tcr-pmhc complex. Biophysical Journal, 95(8):3575–3590, 2008.
220. Bayas, M. V., Schulten, K., and Leckband, D.: Forced detachment of the cd2-cd58 complex. Biophysical Journal, 84(4):2223–2233, 2003.
221. Pan, H., Tao, J., Xu, X., and Tang, R.: Adsorption processes of gly and glu amino acids on hydroxyapatite surfaces at the atomic level. Langmuir, 23(17):8972–8981, 2007.
222. Chu, X., Jiang, W., Zhang, Z., Yan, Y., Pan, H., Xu, X., and Tang, R.: Unique roles of acidic amino acids in phase transformation of calcium phosphates. The Journal of Physical Chemistry B, 115(5):1151–1157, 2011.
223. Balsera, M., Stepaniants, S., Izrailev, S., Oono, Y., and Schulten, K.: Reconstructing potential energy functions from simulated force-induced unbinding processes. Biophysical journal, 73(3):1281–1287, 1997.
224. Jensen, M., Park, S., Tajkhorshid, E., and Schulten, K.: Energetics of glycerol conduction through aquaglyceroporin glpf. Proceedings of the National Academy of Sciences, 99(10):6731–6736, 2002.

225. Luo, Z. and Mehraeen, S.: Unraveling the mechanism of a rising three-phase contact line along a vertical surface using many-body dissipative particle dynamics. Langmuir, 36(26):7474–7482, 2020.

VITA

NAME	Zhen Luo
EDUCATION	M.S., Chemical Engineering, Beijing University of Chemical Technology (BUCT), Beijing, China, 2013
EDUCATION	B.S., Chemical Engineering, Beijing University of Chemical Technology (BUCT), Beijing, China, 2010
TEACHING	Modern 3D Printing (Summer 2017)
PUBLICATIONS	<p>Luo, Z. and Mehraeen, S.: Unraveling the mechanism of a rising three-phase contact line along a vertical surface using many-body dissipative particle dynamics. <u>Langmuir</u>, 36(26):7471-7482, 2020.</p> <p>Luo, Z. and Mehraeen, S.: Predictive model to probe the impact of gravity and surface tension on rising wetting thin films. <u>Langmuir</u>, 35(11):4189-4196, 2019.</p> <p>Zhang, R. D., Liu, N., Luo, Z., Yang, W., Liang, X., Xu, R. N., Chen, B. H., Duprez, D. and Royer, S.: A remarkable catalyst combination to widen the operating temperature window of the selective catalytic reduction of NO by NH₃. <u>ChemCatChem</u>, 6(8):2263-2269, 2014.</p> <p>Luo, Z. and Mehraeen, S. "Impact of confinement on directed self-assembly of sub 10 nm particles into textured substrates." In Proceedings of the American Institute of Chemical Engineers (AIChE, 2020).</p> <p>Luo, Z. and Mehraeen, S. "Kinetics of directed self-assembly of sub 10 nm particles into textured substrates." In Proceedings of the American Institute of Chemical Engineers (AIChE, 2018).</p> <p>Luo, Z. and Mehraeen, S. "Revealing governing mechanism in directed self-assembly of sub-10 nm particles with single particle resolution." In Proceedings of the American Institute of Chemical Engineers (AIChE, 2017).</p>



Predictive Model to Probe the Impact of Gravity and Surface Tension on Rising Wetting Thin Films

Author: Zhen Luo, Shafigh Mehraeen

Publication: Langmuir

Publisher: American Chemical Society

Date: Mar 1, 2019

Copyright © 2019, American Chemical Society

PERMISSION/LICENSE IS GRANTED FOR YOUR ORDER AT NO CHARGE

This type of permission/license, instead of the standard Terms & Conditions, is sent to you because no fee is being charged for your order. Please note the following:

- Permission is granted for your request in both print and electronic formats, and translations.
- If figures and/or tables were requested, they may be adapted or used in part.
- Please print this page for your records and send a copy of it to your publisher/graduate school.
- Appropriate credit for the requested material should be given as follows: "Reprinted (adapted) with permission from (COMPLETE REFERENCE CITATION). Copyright (YEAR) American Chemical Society." Insert appropriate information in place of the capitalized words.
- One-time permission is granted only for the use specified in your request. No additional uses are granted (such as derivative works or other editions). For any other uses, please submit a new request.

[BACK](#)[CLOSE WINDOW](#)

Unraveling the Mechanism of a Rising Three-Phase Contact Line along a Vertical Surface Using Many-Body Dissipative Particle Dynamics



Author: Zhen Luo, Shafigh Mehraeen

Publication: Langmuir

Publisher: American Chemical Society

Date: Jul 1, 2020

Copyright © 2020, American Chemical Society

PERMISSION/LICENSE IS GRANTED FOR YOUR ORDER AT NO CHARGE

This type of permission/license, instead of the standard Terms & Conditions, is sent to you because no fee is being charged for your order. Please note the following:

- Permission is granted for your request in both print and electronic formats, and translations.
- If figures and/or tables were requested, they may be adapted or used in part.
- Please print this page for your records and send a copy of it to your publisher/graduate school.
- Appropriate credit for the requested material should be given as follows: "Reprinted (adapted) with permission from (COMPLETE REFERENCE CITATION). Copyright (YEAR) American Chemical Society." Insert appropriate information in place of the capitalized words.
- One-time permission is granted only for the use specified in your request. No additional uses are granted (such as derivative works or other editions). For any other uses, please submit a new request.

[BACK](#)[CLOSE WINDOW](#)